Nuclear structure studies with (n,d) reactions

Ravenderan Yagambaram Naidoo

December 1988

Submitted in partial fulfillment of the requirements for the Degree of Master of Science in the Department of Physics at the University of Durban-Westville

Supervisor : Professor K. Bharuth-Ram
Co-Supervisor : Dr W.R. McMurray

Abstract

The $^{27}Al(n,d)^{26}Mg$ and $^{56}Fe(n,d)^{55}Mn$ reactions have been studied at 22 MeV incident energy. The 6 MV Van de Graaff facility at the National Accelerator Centre, Faure was used for the experimental aspects. An (n, charged particle) spectrometer was used to detect the energy and angle of the outgoing deuterons. The spectrometer allows for accumulation of particle discriminated data over an angular range of 80^0. The intrinsic geometry of the spectrometer limits its' angular resolution to $\sim 5^0$ (FWHM). The spectrometer has an energy resolution of $\sim$ 0.7 MeV(FWHM). A detailed study of the experimental system has been conducted and the proportional counters in particular were extensively investigated.

A review of the relevant nuclear models for the target and residual nuclei is presented, together with a theoretical outline of the reaction mechanism for the (n,d) reaction. The distorted waves method approach is used in the analysis of the reaction cross sections. Optical potentials are used to simulate the incoming and outgoing distorted waves and thus generate the theoretical cross sections for the (n,d) reactions. The shapes of the angular distributions of the reaction cross sections for different orbital angular momentum transfers are compared to obtain a fit. Comparison of experimental and theoretical cross sections produce the spectroscopic factors which reveal the occupancy or vacany of level states and hence the single particle nature of these states. It was concluded from the study that the shell model of the nuclei under investigation gives a very good description of the results obtained for the (n,d) reactions.

Acknowledgements

I would like to thank the following:

my supervisor, Professor K. Bharuth-Ram and my co-supervisor, Dr. W.R. McMurray, for their guidance, assistance and expertise throughout the supervision of my work

Mr A.C. Bawa for introducing me to this investigation, Mr J.V. Pilcher for assistance with the computing and Piet Groenewald for assistance with some of the diagrams

my colleagues in the Physics Department

those who provided me with accommodation during my visit to the Cape, especially Ravi Naidoo and Niresh Bhagwandeen

the University of Durban-Westville and the CSIR for their financial support

my friends, who helped me keep my studies in perspective

Finally, I save my special thanks for my parents and my wife Pam, for sticking with me through difficult times and for the moral support that made this all possible.

Contents

List of Figures

List of Tables

Chapter 1

Introduction

The study of the interaction of neutrons with atomic nuclei is a subject of unflagging interest in the development of nuclear physics. This is attributable to the specific properties of the neutron, which unlike charged particles, can easily penetrate the nucleus and induce nuclear reactions at relatively low energies. Nuclear reactions have provided excellent tools for the study of nuclei. For this reason the neutron induced reactions under investigation are highly informative for the study of nuclear reaction cross sections and the associated properties of excited states of nuclei. The (n,d) reactions considered in this study can thus be thought of as nuclear structure probes in which the level structure of the incident and residual nuclei and their model configurations are investigated.

In the theoretical analysis of the cross section for reactions such as the (n,d), it is common practice to divide the reaction mechanism into fast direct processes with the excitation of a comparatively small number of degrees of freedom in the nucleus, and slower statistical or compound processes associated with the excitation of complex "long-lived" states of the compound nucleus. Since the direct reaction occurs in a time comparable to the transit time of the projectile through the nucleus, it is expected that

the final nuclear state will retain some knowledge of the initial state and is somewhat similair to the initial state, so that perturbation techniques may be used. Although it is assumed that at sufficiently high energies the direct reaction is the dominant mechanism, it is to be expected that both mechanisms contribute to the observed cross sections.

The (n,d) reaction can be considered, in terms of a direct reaction, as a single step pick-up reaction on the target nucleus. Pick-up reactions and their inverse, the stripping reactions, are of paramount importance in nuclear spectroscopy as they have been instrumental in confirming the shell model of nuclei. These transfer reactions are highly selective due to parity and angular momentum selection rules and this makes them very sensitive to the relationship between the initial and final nuclear states. In particular, the (n,d) reactions are useful as nuclear structure probes because they investigate the single particle character of nuclear states and reveal the occupancy or vacancy of the nuclear levels in terms of spectroscopic factors. These spectroscopic factors measure the extent to which the nuclear levels display a single particle - shell model character and are thus vital in validating the nuclear shell model.

In the reactions invetigated in the present work, incident neutrons of 21.6 MeV impinge on the enriched target foils and the resultant deuterons are detected in the McMurray/Bharuth-Ram spectrometer[1] specially designed for the study of (n,charged particle) reactions. Energy and angle determination of the deuterons provides information on the cross section for the (n,d) reaction. The experimental cross sections are compared with the theoretical cross sections, obtained via a Distorted Waves Born Approximation analysis. The theoretical and experimental cross sections are related in an uncomplicated manner via the spectroscopic factor. The theoretical cross sections are generated by the distorted waves calculation by considering the transition amplitude from initial to final states. Since the pick-up reaction

must satisfy angular momentum selection rules only one or at most two or three l -values will contribute to the cross section of a specific energy level. Optical potentials for elastic scattering in the initial and final systems are used to generate the distorted waves and the theoretical cross sections are then determined within the framework of an Optical model. The DWBA cross sections were determined with the computer program DWUCK4[2].

Working within the broad framework of the shell model, the (n,d) reactions will be considered as single particle transfer reactions to first order. A general overview of single particle transfer reactions will be discussed in section 1.1, to be supplemented in section 1.2 by a critical comparison of proton pick-up reaction studies that are relevant to this study (i.e. (n,d), (d,^{3}He), and (e,e'p)) and followed in section 1.3 by an outline of the relevant nuclear models.

1.1 Single particle transfer reactions

Single particle transfer is realised experimentally in stripping and pick-up reactions. Stripping reactions involve the transfer of one nucleon from the incoming projectile when it passes the nucleus while in pick-up reactions one nucleon is transferred to the projectile as it passes the nucleus. Both reactions can be represented as

$$a + A \rightarrow B + b \tag{1.1}$$

where A denotes the target nuclei, a the incident projectile, B the residual nucleus and b the outgoing particle. For single particle transfers the mass numbers of A and B (and of a and b) differ by one unit. Many reactions proceed by single particle transfer; some common forms of (a,b) are denoted in Table 1.1.

If the single particle transfer takes place with a minimum of rearrangement

proton	transfer	neutron	transfer
stripping	pick-up	stripping	pick-up
(d,n)	(n,d)	(d,p)	(p,d)
(^{3}He,d)	(d,^{3}He)	(t,d)	(d,t)
(α,t)	(t,α)	(α,^{3}He)	(^{3}He,α)

Table 1.1: Examples of single particle transfer reactions

of nucleons in the nucleus involved, then it can be considered a Direct Reaction[3],[4]. For high incident energies the probability of a direct reaction is much greater than that for a compound process in which a fairly long lived intermediate nuclear state is formed. One can generally distinguish between compound processes and direct reactions because direct reactions have the distinguishing features that the intensity of the outgoing particles are peaked in the forward directions and the cross section is not very sensitive to the energy of the incoming particle. Compound nucleus formation is often characterised, at least at low projectile energies, by sharp resonances indicative of preferential formation of long lived compound (intermediate) states prior to breakup.

The cross section $\sigma^{lj}(\theta)$ of a direct reaction for the transfer of a particle of orbital angular momentum l can be written as a product of two parts. Ignoring a few numerical factors the expression for the cross section is

$$\sigma_{exp}(\theta) = N\sigma^{lj}_{DW}(\theta)\langle C\rangle^2 S \tag{1.2}$$

The theoretical cross section $\sigma^{lj}(\theta)$ depends only on the reaction part of the process ie. on energies, scattering angles, angular momentum transfers. It is not influenced by the structure of the initial and final nucleus. This is contained in the spectroscopic factor $\langle C\rangle^2$S. The isospin Clebsch- Gordan factor $\langle C\rangle^2$ takes into account that the transferred particle is either a proton or neutron. N is a normalization factor. The theoretical cross section is usually calculated with a Distorted Waves Born Approximation (DWBA) in the optical model[3,4,5]. The spectroscopic factor C^2S is determined ex-

perimentally from the ratio of theoretical and measured values of $\sigma^{lj}(\theta)$. The experimental spectroscopic factor is then compared with a theoretical C^2S value obtained from the overlap probability of initial and final states, described in terms of a nuclear model.

An interesting feature of single particle transfer reactions is that all reactions that start from a given initial state and lead to the same final state are associated with the same spectroscopic factor C^2S, independent of the projectile used. Thus spectroscopic factors for the reactions (n,d), (d,^{3}He) and (t,α) should be identical and any observed differences in the cross sections should be completely contained in $\sigma^{lj}(\theta)$.

The angular momentum of the transferred nucleon determines the shape of the angular distribution of the outgoing particles. For the pick-up reaction this involves the l -value of the nucleon removed from the target. One can usually extract the l -value from the measured angular distribution as the l -distributions have unique shapes and are sometimes known as l -signatures.

1.1.1 Spin and Parity considerations

If the spin (the angular momentum) of the initial state is J_i and that of the final state is J_f then from conservation of angular moment we must have

$$\vec{J_i} = \vec{J_f} + \vec{j} \tag{1.3}$$

where $\vec{j} = \vec{l} + \vec{s}$ is the vector sum or the orbital angular momentum and the intrinsic spin of the transferred nucleon. Experimentally the determination of $\vec{j}$ for the transferred nucleon is obscure since it can be either $l + 1/2$ or $l - 1/2$ and the angular distributions are generally only sensitive to l . Often the j -dependence leads to two different cross sections with identical geometric shape but differing magnitude.

The parity of the initial state π_i and of the final state π_f must satisfy:

$$\pi_i \pi_l = \pi_f \tag{1.4}$$

The parity of the wavefunction of the transferred particle is given by

$$\pi_l = (-1)^l \tag{1.5}$$

Hence the orbital angular momentum of the transferred particle is restricted by

$$\pi_i \pi_f = (-1)^l \tag{1.6}$$

1.1.2 Spectroscopic factors for pick-up reactions

For a pick-up reaction the cross section is given as

$$\sigma_{exp}(\theta) = N \sigma_{DW}^{lj}(\theta) \langle C \rangle^2 S \tag{1.7}$$

$$\langle C \rangle = \left\langle T_f T_{fz} \frac{1}{2} t_z \mid T_i T_{iz} \right\rangle \tag{1.8}$$

N is a normalization factor depending on the interaction between the transferred nucleus and the outgoing particle. In the isospin formalism the spectroscopic factor must be able to distinguish between neutron and proton pick-up, this is taken into account in the isospin Clebsch-Gordan coefficient $\langle C \rangle^2$. The value $t_z = +\frac{1}{2}$ holds for neutron transfer and $t_z = -\frac{1}{2}$ for proton transfer. The values for $\langle C \rangle$ can be derived from Table 1.2.

The spectroscopic coefficient S, for a pick-up reaction can be expressed by an overlap integral I

$$S = n [I(\rho)]^2 \tag{1.9}$$

Where n denotes the number of active particles in the initial state and is included since the transferred particle may be any one of those in the

	stripping		pick-up	
	proton	neutron	proton	neutron
$T_f = T_i - \frac{1}{2}$	$\frac{T_i+T_{iz}}{2T_i+1}$	$\frac{T_i-T_{iz}}{2T_i+1}$	$\frac{T_f-T_{fz}+1}{2T_f+1}$	$\frac{T_f+T_{fz}+1}{2T_f+1}$
$T_f = T_i + \frac{1}{2}$	$\frac{T_i-T_{iz}+1}{2T_i+1}$	$\frac{T_i+T_{iz}+1}{2T_i+1}$	$\frac{T_f+T_{fz}}{2T_f+1}$	$\frac{T_f-T_{fz}}{2T_f+1}$

Table 1.2: Isospin Clebsch-Gordan coefficients[4]

antisymmetric initial state. Here ρ specifies all quantum numbers of the transferred nucleon.

The overlap integral is defined from the wave functions Φ by:

$$I(\rho) = \left\langle \left[\Phi^{as}_{r_f}(1,....,n-1)\, X\rho(n)\right]_{r_i} \mid \Phi^{as}_{r_i}(1,....,n)\right\rangle \tag{1.10}$$

where X denotes vector coupling.

Thus the value of I(ρ) depends on the overlap between the initial state $\Phi^{as}_{r_i}(1,....,n)$ which is completely antisymmetric in the n active particles, and the state formed by coupling the final state $\Phi^{as}_{r_f}(1,....,n-1)$ (antisymmetric in n-1 particles) with the transferred particle to a coupled state Γ_f. Maximum overlap yields:

$$\mid I(\rho) \mid = 1 \tag{1.11}$$

1.2 Advantages and limitations of proton pick-up reactions

As the initial and final state configurations for direct reactions are independent of the type of projectile used, the spectroscopic factors obtained via (n,d), (d,^{3}He) and (e,e'p) reactions should be similar. This makes it interesting to compare the values obtained via the different reactions. Also, the spectroscopic factors are largely independent of the incident energy and it is possible to compare previous (n,d) and (d,^{3}He) studies with the present work.

The chief motivation for experiments in which a single nucleon is removed from a shell is to investigate to what extent the single- particle shell model extends to states at and below the Fermi surface. In this both the (n,d) and (d,^{3}He) reactions are intrinsically flawed; these pick-up reactions are mainly sensitive to the asymptotic tail of the wave-function of the proton hole state i.e. these are essentially surface reactions and do not probe deep hole states, and as a result, the entire proton hole state wave function is not explored as in the (e,e'p) reaction. The investigation of deep hole states in the ^{27}Al(e,e'p)^{26}Mg[6] reaction leads to an interesting comparison of proton occupation numbers from the shell model, pick-up reactions and the (e,e'p) reaction.

In recent studies of the ^{90}Zr(e,e'p)^{90}Y and ^{51}V(e,e'p)^{50}Ti reactions den Herder et al.[7][8] obtain spectroscopic factors for the transitions to states in the product nuclei that are in disagreement with theoretical shell model values and values obtained from (d,^{3}He) reactions[9,10,11,12]. The (e,e'p) measurements are incompatible with spin-dependent sum rules(SDSR)[13] and a theoretical understanding of single particle strengths in nuclei, and suggest that a major fraction of the transition strengths are unobserved in

the nucleon induced pick-up reactions. It is thus worthwhile to investigate the proton pick-up strengths via the (n,d) reactions as a further test of relevant nuclear models.

A comparison between proton pick-up via (n,d) and (d,^{3}He) reactions is of interest as a comparison of the advantages and limitations of the two reactions. As a result of the complex incoming and outgoing projectiles, the energy required for good energy resolution in the (d,^{3}He) reaction is generally higher than for the corresponding (n,d) reaction. Projectile breakup and multi-step processes are also more likely to be prevalent and the charged nature of the incoming projectile makes for additional competing reactions.

Optical potentials for the (d,^{3}He) reactions are not as well documented and generally less well understood than for the (n,d) reactions. This is highlighted by the variation in the normalisation factor, N, for calculation of cross sections via the distorted waves method. Fulmer[14] has calculated the constant to be 2.95 for (d,^{3}He), while Chant[15] has suggested a value of 2.0 and Ioannides[16] has calculated the value as being 2.363.

The (n,d) reaction is by no means without problems. Until recently inefficient detection systems and low neutron fluxes have resulted in excessive run-times. High background rates and competing reactions that result in charged particles complicate matters. The techniques used for the study of (n,d) reactions generally gave relatively poor energy resolution which severely limited the range of nuclei that could be investigated. Recent technical developments at TRIUMF, Canada[17] have made it possible to use the high resolution capabilities of their magnetic spectrometer for the outgoing charged particles, an advantage always enjoyed by investigators using the (d,^{3}He) and (t,α) reactions.

The relatively low incident energies that have been used previously to study

the (n,d) reaction meant that only the ground state or the lowest lying excited states were analysed and the poor energy and angular resolution resulted in inadequate determination of cross sections. The contradictory interpretation of previous (n,d) results throws doubts as to the quality of these results. For the ^{27}Al(n,d)^{26}Mg reaction especially, a low energy investigation[18] of proton pick-up has been interpreted in terms of the rotational model, while a higher energy study[19] has found the low-lying states to be of a shell model nature while the higher excited states are rotational in nature.

1.2.1 The ^{27}Al(n,d)^{26}Mg reaction

The ^{27}Al(n,d)^{26}Mg reaction studied is of particular interest as previous (n,d) reactions and (d,^{3}He) reactions have been explained by varying theoretical models for the target and residual nuclei. The ^{27}Al and ^{26}Mg nuclei lie in the transition region from prolate to oblate deformation and a true picture of these nuclei can only be obtained when there is good correlation between the theoretical models and the experimental results. The nature of the levels and the structure of ^{26}Mg have been extensively studied by proton pick-up reactions including: ^{27}Al(n,d)^{26}Mg at 14.8MeV[18] and 56.3MeV[19] and ^{27}Al(d,^{3}He)^{26}Mg at 12.8MeV[20], 15MeV[21], 34MeV[22] and 52MeV[23]. At energies below 20 MeV only the lowest three levels have been examined; whilst the optical potentials for (n,d) reactions are generally better understood than for more complex particles. This emphasises the usefulness of the (n,d) reaction as a tool in investigating the nature of the excited states in ^{26}Mg. A comparison of (n,d) and (d,^{3}He) data is of interest as the spectroscopic factors from (d,^{3}He) reactions exhibit a marked energy dependence as compared to those from the (n,d) reaction[23].

The structure of ^{26}Mg has been based on very differing experimental and

theoretical results. The explanations of the structure of ^{26}Mg are as varied as the different results, these range from the shell model explanations of Wildenthal[24] to a weak coupling model and to a strong coupling or rotational model. Varying degrees of success have been achieved with these models and with modifications to these models, in particular the shell model with Adjusted Surface-Delta Interaction(ASDI) and the rotation/vibration models[24] have had some success in explaining the structure of ^{26}Mg; but by far the most comprehensive model structure is found in the combination of simple shell and rotational features in the Deformed Shell Model(DSM) advanced by Craig[26]. The varied approaches to the structure of ^{26}Mg emphasises the need for more experimental data to complete the theoretical picture.

1.2.2 The ^{56}Fe(n,d)^{55}Mn reaction

The ^{56}Fe(n,d)^{55}Mn study has only been done at relatively low energy[27](14MeV) in which only the ground state was adequately excited. Recent ^{56}Fe(d,^{3}He)^{55}Mn work[28] at 80MeV has revealed spectroscopic factors that are in good agreement with shell model values. The ^{56}Fe and ^{55}Mn nuclei lie close to the supposed doubly magic ^{56}Ni nucleus and in recent years considerable attention has been paid to to the energy levels of nuclei close to ^{56}Ni[29]. Quasi-particle core coupling model and cluster vibration models[28] have been employed to explain the the positive parity states of ^{55}Mn due to problems with handling the large model space in shell model calculations.

1.3 Outline of relevant nuclear models

In order to adequately analyse the experimental data it is important to consider the theoretical models and model spaces for the incident and residual nuclei. The experimental data will then be correlated with the theoretical predictions to provide an understanding of the nuclear interaction within the framework of a model.

1.3.1 ^{27}Al(n,d)^{26}Mg

(i) The target nucleus ^{27}Al.

An interpretation of the structure of ^{27}Al is complicated as it lies in the transition region between prolate(^{25}Mg, ^{25}Al) and oblate(^{28}Si, ^{29}Si) deformation, hence it's properties are not easily described by a single model. Previous studies investigating the structure of ^{27}Al have been done with varying approaches, including elastic scattering, lifetime measurements, stripping and pick-up reactions [30],[31],[32],[33].

In the shell model description of the ^{27}Al nucleus the configuration space used is the $1d_{5/2}{}^{n}2s_{1/2}{}^{l}1d_{3/2}{}^{m}$ space in which ^{16}O is treated as an inert core. The valence protons are distributed such that n+l+m=11. This configuration space is well suited for studying low-lying levels of nuclei in the middle of the s-d shell. The dominant configuration in this space is then expected to be $1d_{5/2}$ and the ^{27}Al ground state is described as a $d_{5/2}$ proton coupled to the ground state of ^{26}Mg. Several calculations with shell model prescriptions and modified shell model descriptions[30],[34] have been applied to explain the spectroscopic factors obtained with proton pick-up from ^{27}Al. These refined interaction calculations for the s-d shell show good agreement with detailed experimental results.

Assuming a physical interpretation of the ^{27}Al nucleus as a single proton coupled to the ground state of ^{26}Mg, then the extent to which ^{27}Al can be described either as rotational, vibrational or spherical depends on (i) the extent to which the ^{26}Mg basis space is either rotational, vibrational or spherical or (ii) the extent to which the additional proton that makes up ^{27}Al induces such effects. Therefore an interpretation of the state of the 'core' nucleus ^{26}Mg is very important as is the understanding of the residual nucleon-nucleon interaction.

A microscopic description of ^{27}Al by a shell model calculation has proven valuable in reproducing the energy levels and spin sequence for the low excitation region of the ^{27}Al level scheme as well as the characteristics revealed by single nucleon transfer and electromagnetic transition rates. Alternately, additional insight into the band structure of ^{27}Al can be gained from various macroscopic models [33],[35].

The simplest macroscopic model which has been successfully applied to explain the structure of ^{27}Al is the excited core model [35],[36],[37]. In this model the ground state of an odd mass nucleus (^{27}Al) is described as a particle (or hole) in the lowest allowed orbital of the average potential due to the even-even core (^{28}Si). If the energy required to raise this odd hole to the next single "particle" state is comparable to or larger than the excitation energy of the core, then low-lying excited states of the odd nucleus can be described predominantly as collective excitations of the core. Pauli blocking effects and core polarization effects are ignored under the assumption that the valence nucleons do not appreciably perturb the core. The ground state of ^{27}Al is then described as the coupling of a $d_{5/2}$ proton hole to the ^{28}Si core (Fig 1.1).

The excited core model is also known as the weak coupling model and although it is successful in describing elastic scattering of light particle on

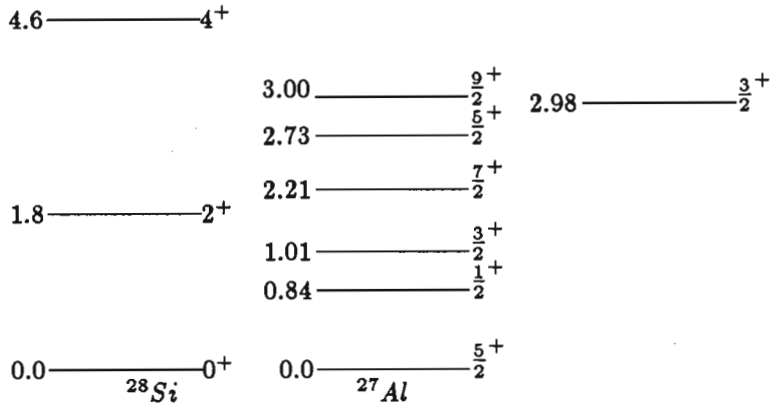

Figure 1.1: The weak coupling model of ^{27}Al formed by coupling a $d_{5/2}$ proton hole to ^{28}Si[31]

^{27}Al[31] and reproducing many of the electromagnetic transition probabilities, it fails in predicting the correct spectroscopic factors for one nucleon transfer into or out of ^{27}Al[38].

The strong coupling model, also known as the rotational model, partially resolves these problems. The strong coupling model assumes a static prolate deformation of the nucleus. Following the extreme rotational model of Nilsson, the ^{27}Al ground state (Fig. 1.2) is described by filled Nilsson orbits no. 6, $\Omega=\frac{1}{2}$ and no. 7, $\Omega=\frac{3}{2}$. There is just a single proton in orbit no. 5, $\Omega=\frac{5}{2}$ resulting in a proton hole in that orbit.

Using equation (16) from Satchler[39] and the Nilsson coefficients obtained by Chi[40], spectroscopic factors for the ^{27}Al(n,d)^{26}Mg reaction have been extracted in the rotational model. The spectroscopic factors for proton pick-up from the Nilsson orbits Ω leading to final states in ^{26}Mg denoted by J^{π} and $K=\mid \frac{5}{2}+\Omega \mid$ are quoted in the results under the strong coupling model.

The rotational model has been successful in reproducing the low lying lev-

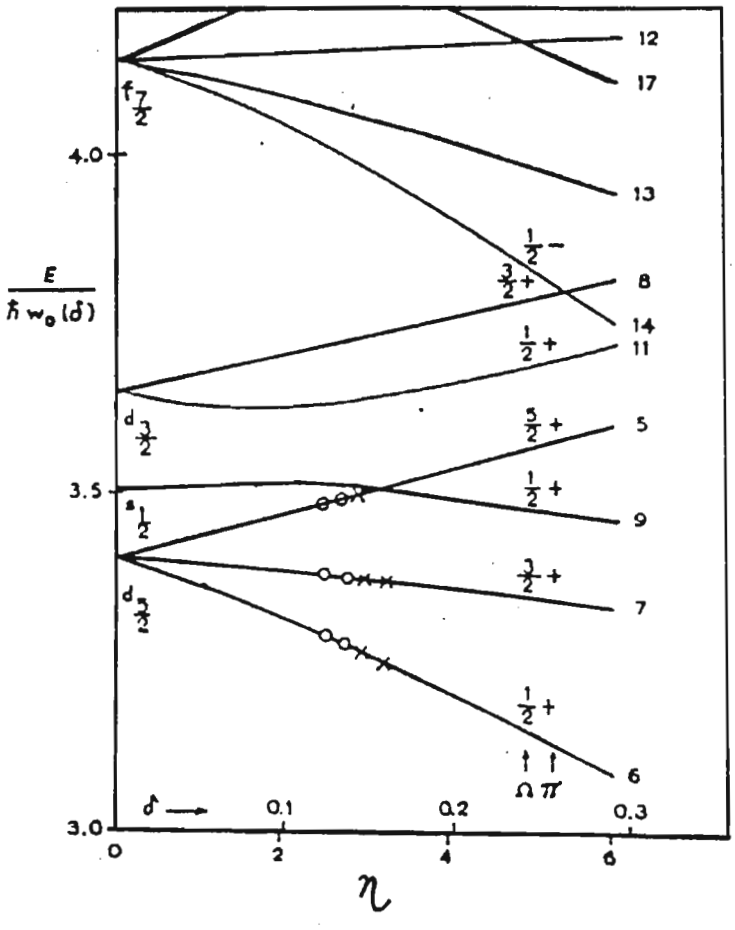

Figure 1.2: Nilsson diagram for the ground state of ^{27}Al, deformation parameter $\eta \simeq 3$. Neutrons are denoted by circles and protons by crosses[18]

els and many of the electromagnetic transition rates of ^{27}Al. Using the rotational model with an oblate instead of prolate deformation, and including Coriolis mixing, it has been shown[33] that the strong coupling model can account for enhanced E2 transitions between ^{27}Al states and for spectroscopic factors for single nucleon pick-up from ^{28}Si. However, inelastic scattering data and the band structure of ^{27}Al are incompatible with the strong coupling model.

A novel combination of the complementary aspects of these two models in a rotational-vibrational coupling scheme[41] accounts well for much of the experimental data on ^{27}Al: inelastic scattering for up to 3 MeV states

are well described as are E2 transition rates and level spacings, but some difficulty still exists in the determination of spectroscopic factors.

In light of these varying approaches into the interpretation of the structure of ^{27}Al, additional experimental data is required to rigorously test the different macroscopic models. The present study takes into account the fact that although ^{27}Al is deformed, a spherical optical model can still be applied to understand the ^{27}Al(n,d)^{26}Mg reaction as long as suitable adjustments in the optical potentials are made.

(ii) The residual nucleus ^{26}Mg.

The structure of ^{26}Mg has been studied through elastic scattering[42][43][44], stripping reactions[45], Doppler shifted lifetime measurements[46] and pick-up reactions[18],[19],[20],[22],[23]. The structure of ^{26}Mg is of special interest as a result of its unique position among the nuclei; it lies in the middle of the s-d shell where the the nuclear shape changes from prolate to oblate. An exact description of the nuclear structure of ^{26}Mg is elusive; its properties have been described both by a single particle shell-model and by a collective rotational model, with varying degrees of success.

The various approaches into interpreting the structure of ^{26}Mg is compounded by conflicting experimental evidence for both models. Electromagnetic transition rates are known to be considerably enhanced above the Weisskopf single particle values, a feature which is commonly attributable to collective motion of the nucleus. This is supplemented by the fact that many of the low-lying energy levels can be arranged into overlapping rotational bands. The rotational nature of ^{26}Mg has found basis in a large amount of experimental evidence that supports such a model[20],[21],[23],[43],[46]

The independent particle shell model has also had success in explaining the

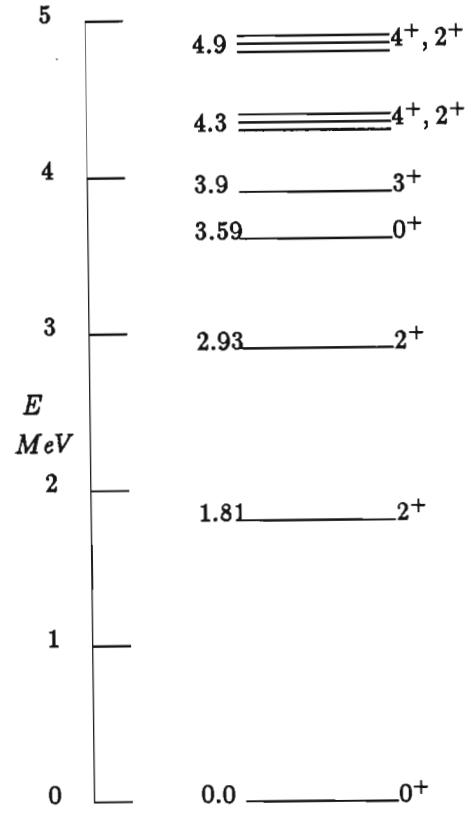

Figure 1.3: Energy levels in ^{26}Mg[47]

structure of ^{26}Mg. Theoretical calculations using the Kuo and Preedom-Wildenthal interactions in the full s-d basis with ^{16}O as an inert core have been used to predict the energy spectra of ^{26}Mg[48]. Spectroscopic factors have been well accounted for with the shell model description, in particular shell model calculations using an Adjusted Surface Delta Interaction (ASDI)[34] has been particularly well suited towards yielding correct spectroscopic factors for stripping and pick-up to ^{26}Mg. This apparent ambiguity in interpretation of the structure of ^{26}Mg is further complicated by the fact that recent proton pick-up reactions leading to ^{26}Mg reveal spectroscopic factors that are consistent with a shell model description rather than a rotational model description[19],[23]. The simple shell model, how-

ever, is inadequate in accounting for the electromagnetic transition rates between excited states and cannot predict the experimentally observed band structure[43].

Cujec[21] considered the ^{26}Mg nucleus to be built up from the ^{24}Mg nucleus by the addition of two neutrons. On the basis of the similarities of the the low-lying states of the magnesium isotopes, a rotation-vibration model was proposed. However, the level spectrum of ^{26}Mg differs grossly from the simpler rotational band structure of ^{24}Mg. Despite the absence of obvious rotational bands in ^{26}Mg, Robinson et al.[46] attempted to fit the rotation-vibration model to the structure of ^{26}Mg and found that the rotor-vibrator model was only able to reproduce the positions of the first three levels but not the higher states. From the point of view of the shell model the T=0 ^{24}Mg nucleus and the T=1 ^{26}Mg are vastly different. Other T=1 nuclei in the s-d shell such as ^{30}Si exhibit a level structure more like that of ^{26}Mg than does ^{24}Mg.

Since ^{26}Mg lies near the centre of the s-d shell where nuclear deformation changes from prolate to oblate shape and from strong to weak coupling, it might be expected that ^{26}Mg has only a small deformation and exhibits a vibrational spectrum. Indeed, elastic electron scattering[42] has shown that ^{26}Mg has a lower quadrupole moment than either ^{24}Mg or ^{25}Mg and that it's mean square charge radius is smaller than for the other two magnesium isotopes. This is at odds with the empirical $A^{1/3}$ rule which ascribes a larger mean square charge radius for ^{26}Mg. Mackintosh[25] has also determined that ^{26}Mg is a poor rotational nucleus using Skyrme-type interactions. Skyrme interactions are effective interactions used to calculate the transition rates for multipole operators acting between states projected from Hartree -Fock deformed intrinsic states and give a good description of light deformed nuclei.

The last two neutrons have a strong sphericising tendency on ^{26}Mg, resulting in the smaller deformation. The proton and neutron orbits vary in the shape they assume; the protons tend towards deformation as in the ^{24}Mg nucleus whereas the addition of two neutrons to ^{24}Mg favours a spherical solution for the neutron orbits. Hence the resulting nucleus must be a compromise for which the collectivity ratios are lower than in ^{24}Mg. Talmi and Unna[49] have shown that the light deformed nuclei in the s-d shell, due to strong configuration mixing, can be traced to the the strong isoscalar residual interaction between neutrons and protons. This is especially so when they occupy the partner orbits $d_{5/2}$ and $d_{3/2}$. Thus we might speculate that the relationship of the N-N interaction is of importance for such a nucleus. The importance of the n-p interaction in the s-d region in producing deformation can be noted by a comparison of the energy spectra of ^{20}Ne and ^{20}O. The ^{20}O nucleus can be understood in terms of simple shell model configurations while the ^{20}Ne nucleus exhibits a ground state rotational band (Fig 1.4).

Mackintosh[25] also contends that as a result of the competition between proton and neutron densities which have different deformations, the equilibrium deformation may be different from either of the nucleon deformations and the collectivity properties are not necessarily defined for the nucleus as a whole, but are independent properties of the proton and neutron densities. This leads to the conjecture that "how rotational" the nucleus is may depend on the projectile that is interacting with it. This may have some significance in interpreting the structure of ^{26}Mg as it is generally the elastic scattering experiments that indicate the rotational nature of the nucleus whereas proton pick-up results indicate a shell model.

The deformed shell model (DSM) advanced by Craig[26] presents the most comprehensive description of the level structure of ^{26}Mg. The DSM describes ^{26}Mg as a symmetric prolate rotor core of ^{24}Mg combined with an

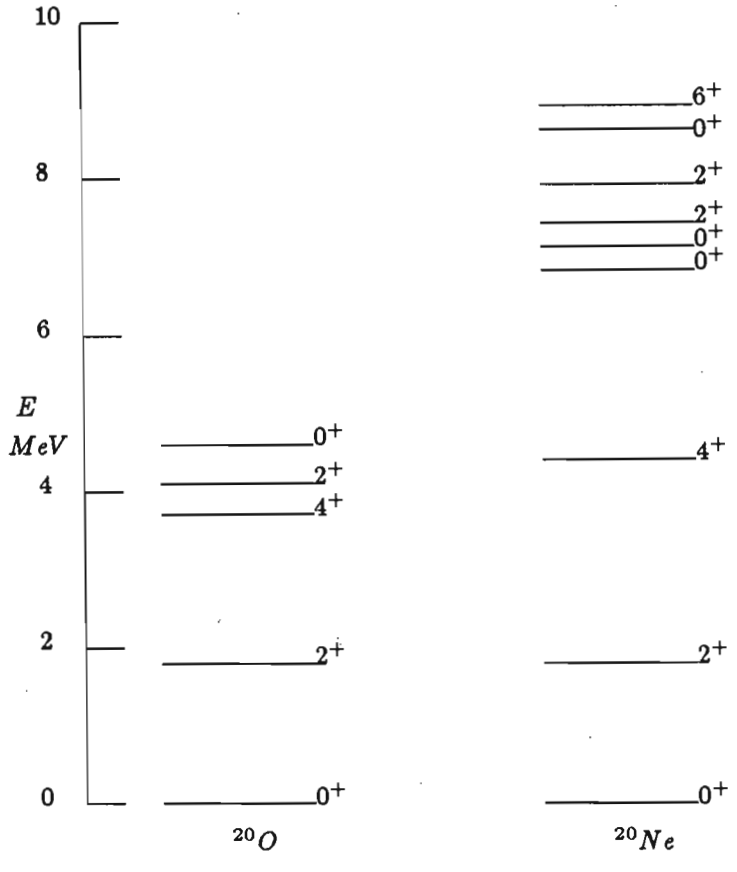

Figure 1.4: The effect of the N-N interaction on isotones[50]

intrinsic two-particle state. The Hamiltonian for the valence nucleons coupled to the core is given by:

$$H = A \times R^2 + H_{sp} + V \tag{1.12}$$

$$A \simeq 0.25 MeV \, for \, {}^{24}Mg$$

where A is the reciprocal moment of inertia and R the angular momentum of the core nucleus ^{24}Mg, H_{sp} is the single particle Hamiltonian for the valence nucleons and V the residual interaction between the valence nucleons. The

collective and single particle degrees of freedom are coupled by the mean field generated by the core nucleons. The core is also chosen so that the single particle spectrum should split naturally into inert core orbitals and active valence orbitals. The parameters of the DSM are then associated with the collective and single particle aspects of the deformed field.

The DSM is based on the combination of the spherical shell model and the collective rotational model, while incorporating some of the phenomenology of microscopic theory. The Hartree-Fock (HF) model also predicts an axially symmetric prolate shape for ^{24}Mg. However, the use of Hartree-Fock valence orbitals to describe the additional neutrons in ^{26}Mg is problematic as the HF solutions demand that the single particle wavefunctions remain unchanged. This may not be the situation if the rotor core is polarized by the addition of valence particles, resulting in a change in deformation of the average potential. Hence in the DSM the Hartree-Fock single particle energies are renormalised according to the empirical single particle values obtained from the next odd nucleus ^{25}Mg as is done in the spherical shell model.

1.3.2 ^{56}Fe(n,d)^{55}Mn

(i) The target nucleus ^{56}Fe

^{56}Fe, with N=30, Z=26 is described in the simple shell model as having a shell closure core of ^{48}Ca, two extra core neutrons and six valence protons. Configuration mixing of the two extra core neutrons is allowed and the active neutron orbits are the $p_{3/2}p_{1/2}f_{5/2}$ shells while the active proton orbit is the $f_{7/2}$ shell.

A shell model description of ^{56}Fe that includes the positive parity levels requires very large scale shell model calculations. Valuable insight into the high spin states of ^{56}Fe has been derived both by a conventional truncated shell model calculation[51] and by a microscopic description of the levels in ^{56}Fe[52].

The proximity of ^{56}Fe to the doubly closed shell at ^{56}Ni leads to an interpretation of the structure of ^{56}Fe in a rather simple form, described in terms of a few valence particles with rather pure shell model configurations. The ^{56}Fe nucleus is light enough to be treated microscopically and probably also heavy enough to exhibit some collective properties. ^{56}Fe has been the subject of various experimental[53],[54] and theoretical investigations [55],[56].

In recent shell model calculations[28], two different residual interactions have been employed: (i) a modified interaction based on the Kuo-Brown(KB) matrix elements and (ii) the schematic surface delta interaction(SDI). Large scale shell-model calculations have revealed a good correlation between experiment and theory for the low-lying levels in ^{56}Fe[56]. Spectroscopic factors for single particle transfer as well as electromagnetic transition rates and moments are well reproduced by the shell model description.

However, there is also evidence that ^{56}Fe displays collective behaviour in the low-lying states[57]. In recent shell model approaches to rotational nuclei[56], rotational spectra are expected to appear in nuclei having active neutrons and protons moving in different shell orbits, a condition for which ^{56}Fe qualifies.

It has been suggested that because ^{56}Fe lies close to the spherical nickel nuclei, it may qualify for shape co-existence, known to occur in some soft or transitional nuclei. This is substantiated by the existence of a prolate ground state quasi-rotational band and recent evidence for oblate deformation of the high spin states[58].

The apparent contradictions in spherical-prolate-oblate deformation may be resolved if one considers the calculations of Tanaka and Sheline[59] in which calculations for ^{56}Fe were performed in an aligned coupling scheme, used to construct wavefunctions from spherical bases in order to explain possible quasi-band structure. The emergence of prolate-and oblate-like deformations from spherical bases and the correct prediction of transition rates and quadrupole moments gives the aligned coupling scheme strong support in explaining the structure of ^{56}Fe.

(ii) The residual nucleus ^{55}Mn

Shell model calculations for ^{55}Mn are similar to those for ^{56}Fe in that they are based on the closed ^{48}Ca core with two neutrons in the $p_{3/2}p_{1/2}f_{5/2}$ shell and five active protons in the $f_{7/2}$ shell. Shell model calculations for ^{55}Mn have also been performed with the Kuo-Brown interaction and the surface delta interaction and reveal excitation energies, magnetic moments, quadrupole moments, lifetimes and relative branching ratios for the excited states that are in fair agreement with experimental values [56].

The ground state spin of ^{55}Mn is $J^{\pi}=\frac{5}{2}^{-}$ which differs from the prediction of the simple shell model and can only be explained by the presence of strong proton-neutron interactions. Although the negative parity levels in ^{55}Mn are well described by use of the KB and SDI shell model codes, a shell model description for the positive parity levels has not been accurately given due to difficulties in handling the very large model space required. Even though these positive parity levels are not adequately excited in the present study it is nevertheless worthwhile to see whether models prescribed for investigating the positive parity levels reveal correct spectroscopic factors for the low-lying negative parity levels.

Two models[28] that include a description of the positive parity levels in ^{55}Mn are (i) the quasi-particle core coupling model(QPCC) and (ii) the cluster vibration model(CVM).

Quasi-particle core coupling has been used to describe the ^{55}Mn nucleus structure, especially those configurations for which there is a particle excited out of the s-d shell orbitals. Core excitations are dealt with by simplifying them into harmonic quadrupole and octupole vibrations. QPCC calculations are unable to reproduce all the detailed properties of the negative parity levels but do describe the low-lying positive parity states if the

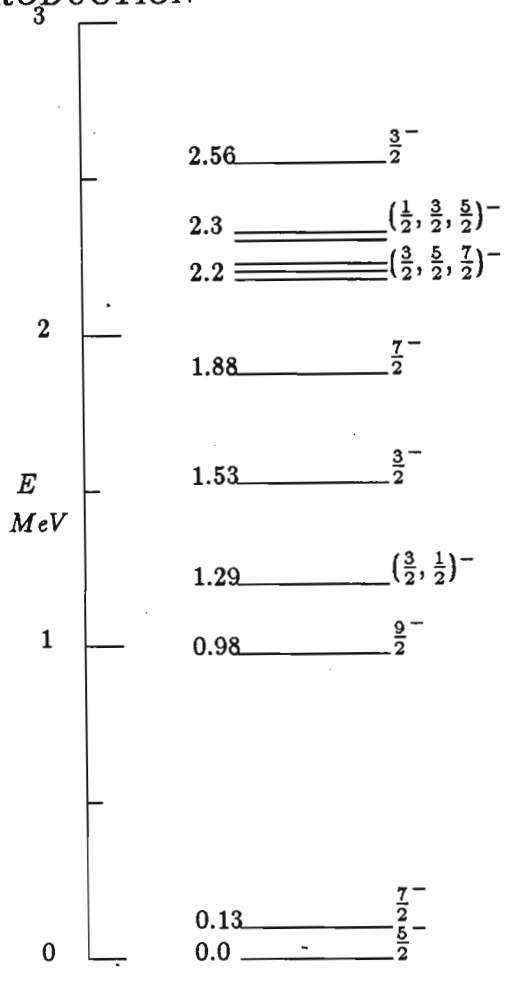

Figure 1.5: The low-lying levels in ^{55}Mn[47].

s-d single hole excitations are incorporated with the $f_{7/2}$, three hole state.

The negative parity levels in the QPCC model have substantial pick-up strengths only for the $1f_{7/2}$ orbital and this is largely concentrated in the ground state, while shell model calculations predict a more pronounced spread in the pick-up strength over the excited states. In the calculations for the positive parity levels the pick-up strengths are almost half the expected values, an indication of important mixing with nearby levels.

In the cluster vibration model(CVM), the odd ^{55}Mn nucleus is described by coupling 3 proton holes, below the the Z=28 shell, to the quanta of

quadrupole vibration of the core. The three hole $f_{7/2}$ configuration in the Z=20-28 shell plays the dominant role in this model. In the calculations by Puttaswamy et al.[28], use of the CVM is advantageous as the spectroscopic factors in the CVM have been calculated with none of the parameters of the CVM adjusted to fit experiment.

The CVM is flawed in that if there is sizable coupling between the hole cluster and the vibrational core the perturbation criterion of the shell model does not hold anymore and the wavefunction will not have any distinctive leading component. This would imply an insensitivity of the the spectroscopic factor to changes in the wave function.

References

1.) W.R. McMurray and K. Bharuth-Ram, S.Afr. J. Phys. 8 (1985) 22.
2.) P.D. Kunz, University of Colorado, 1978, unpublished.
3.) G.R. Satchler, Nucl. Phys. A55 (1964) 1.
4.) N. Austern, Direct Nuclear Reaction Theories (Wiley Interscience, New York, 1970).
5.) P.E. Hodgeson, Rep. Prog. Phys. 47 (1984) 613.
6.) K. Nakamura et al., Nucl. Phys. A271 (1976) 221.
7.) J.W.A. den Herder et al., Phys. Lett. 161B (1985) 65.
8.) J.W.A. den Herder et al., Phys. Rev. Lett. 57 (1986) 1843.
9.) C.K. Kovalski et al., Phys. Rev. 161 (1967) 1107.
10.) B.M. Preedom, E. Newman and J.C. Halbert, Phys. Rev. 166 (1968) 1156.
11.) A. Stuirbank et al., Z. Phys. A297 (1980) 307.
12.) J.N. Craig, N.S. Wall and R.H. Bassel, Phys. Rev. Lett. 36 (1976) 565.
13.) S.M. Perez, Phys. Rev. Lett. 60 (1988) 1342.
14.) C.B. Fulmer and J.B. Ball, Phys. Rev. 140B (1965) 330.
15.) N.S. Chant et al., Phys. Rev. C15 (1977) 53.
16.) A.A. Ioannides, M.A. Nagarajan and R. Shyam, Nucl. Phys. A363 (1981) 150.
17.) W.P. Alford, (n,p) Reaction Studies (2nd Conference on Intersections between Particles and Nuclear Physics, Lake Louise, May 1986).
18.) R.N. Glover and E. Wiegold, Nucl. Phys. A24 (1961) 630.
19.) F.P. Brady et al., Nucl. Phys. A288 (1977) 269.
20.) F. Pelligrini and S. Wiktor, Nucl. Phys. 40 (1963) 412.
21.) B. Cujec, Phys. Rev. 128 (1962) 203.
22.) B.H. Wildenthal and E. Newman, Phys. Rev. 175 (1968) 1431.
23.) G.J. Wagner et al., Nucl. Phys. A125 (1969) 80.
24.) B.H. Wildenthal et al., Phys. Lett. 26B (1968) 692.
25.) R.S. Mackintosh, J. Phys. G.: Nucl. Phys. V4 (1978) 547.
26.) G. Craig, Nucl. Phys. A225 (1974) 493.
27.) L. Colli et al., Nucl. Phys. 46 (1963) 73.
28.) N.G. Puttaswamy et al., Nucl. Phys. A401 (1983) 269.
29.) P.W.M. Glaudemans and R. Vennik, Phys. Lett. 95B (1980) 171.
30.) B.H. Wildenthal and J.B. McGory, Phys. Rev. C7 (1973) 714.
31.) G.M. Crawley and G.T. Garvey, Phys. Rev. 167 (1968) 1070.
32.) W. Bohne et al., Nucl. Phys. A131 (1969) 273.
33.) D. Dehnard, Phys. Lett. 38B (1972) 389.
34.) F. Meurders, P.W.M. Glaudemans, J.F.A. Van Hienan and G.A.

Turimer, Z. Physik A276 (1976) 113.
35.) V.K. Thankappan, Phys. Rev. 141 (1966) 957.
36.) C.S. Whisnant, J.H. Dave and G.R. Gould, Phys. Rev. C30 (1984) 1435.
37.) G.C. Bonazolla, E. Chiawassa and T. Bressani, Phys. Rev. B140 (1965) 835.
38.) F.B. Malik and W.Scholz, Nuclear Structure (North Holland, Amsterdam, 1967).
39.) G.R. Satchler, Ann. of Phys. 3 (1958) 275.
40.) B. Chi, Nucl. Phys. 83 (1966) 97.
41.) H. Ropke, V. Glattes and G. Hammel, Nucl. Phys. A156 (1970) 477.
42.) E.W. Lees et al., J. Phys. G.: Nucl. Phys. 2 (1976) 105.
43.) P. Wagner, M.A. Alli, J.P. Coffin and A. Gallman, Phys. Rev. C11 (1975) 1622.
44.) A. Nagel et al., J. Phys. G.: Nucl. Phys. 1 (1975) 324.
45.) B. Cujec, Phys. Rev. B136 (1964) 1305.
46.) S.W. Robinson and R.D. Bent, Phys. Rev. 168 (1968) 1266.
47.) C.M. Lederer et al., Table of Isotopes, 7ed. (Wiley Interscience, New York, 1976).
48.) B.J. Cole, A. Watt and R.R. Whitehead, J. Phys. G.:
Nucl. Phys. 2 (1976) 501.
49.) I. Talmi, Rev. Mod. Phy. 34 (1962) 704, I. Unna,
Phys. Rev. 132 (1963) 2225.
50.) P. Federman and S. Pittel, Phys. Rev. C20 (1979) 820.
51.) J.B. McGrory, Phys. Rev. 160 (1967) 915.
52.) P.W.M. Glaudemans and R. Vennik, Phys. Lett. 95B (1980) 171.
53.) S.M. El Kadi, Nucl. Phys. A390 (1982) 509.
54.) D.G. Sarantities et al., Phys. Rev. C14 (1976) 1412.
55.) J.B. McGrory and S. Raman, Phys. Rev. C20 (1979) 830.
56.) H. Horie et al., Nucl. Phys. A216 (1973) 407.
57.) J.P. Delaroche et al., Nucl. Phys. A390 (1982) 509.
58.) N. Bendjaballah, Phys. Rev. Lett. 36 (1976) 1536.
59.) Y. Tanaka and R.K. Shaline, Phys. Lett. 56B (1975) 309.

Chapter 2

Theory

The interaction between a nucleon and a nucleus is of basic importance in the study of nuclear reactions. It is essentially rather complicated, as it is the sum of all the interactions between the incident(outgoing) nucleon and all the nucleons comprising the target(residual) nucleus, modulated by the interactions among these nucleons. There are two basic reaction types that are of importance: direct reactions and compound reactions. Direct reactions, which we are concerned with, can be classified as involving only a few internal degrees of freedom for the colliding systems, whether these are best described by single particle or collective modes. Compound theory, on the other hand, involves statistical distributions and is associated with long-lived, complex intermediate states that are formed in the interaction of nucleus and nucleon. Compound reactions are generally characterized by sharp resonances, indicative of these intermediate states.

Current theories for direct reactions[1],[2],[3] assume a weak coupling for the interaction in that elastic scattering is the major process involved and

inelastic or re-arrangement reactions are treated as perturbations. This gives rise to the Distorted Waves Born Approximation expression for the transition amplitude[4],[5] in which the interaction responsible for the reaction occurs just once; that is, it describes a simple one-step process. The relative motion of the pair of nuclei before and after the event is then described by distorted waves, which are calculated using an Optical Model approximation.

Previous theories using plane wave approximations[6],[7] were found to over estimate the cross section (see Fig 2.1), often by an order of magnitude or more. The importance of the distorted waves method has been firmly established over the years as a means of determining cross sections .

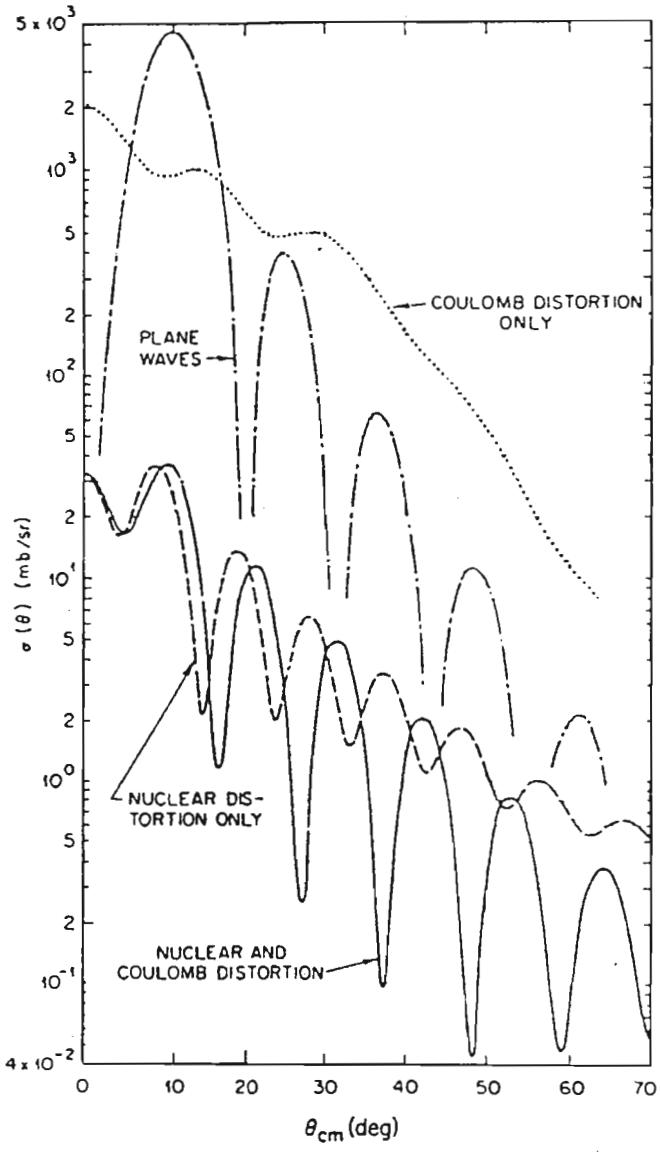

Figure 2.1: The effects of distortion caused by the Coulomb and nuclear potentials on elastic scattering of alpha particles[8]

2.1 The Distorted Waves Method

Consider the following reaction:

$$a + A \rightarrow b + B \tag{2.1}$$

where the entrance channel (a,A) is denoted by α and the exit channel (b,B) is denoted by β. The DWBA theory for this reaction is based on the transition amplitude of the form:

$$T_{\beta\alpha} = J_{\beta\alpha} \int d\vec{r}_\alpha \int d\vec{r}_\beta \chi_\beta^{(-)*}(k_\beta, r_\beta) \langle \beta \mid W \mid \alpha \rangle \chi_\alpha^{(+)}(k_\alpha, r_\alpha) \tag{2.2}$$

where W is the residual interaction and the relative co-ordinates r_α , r_β are given by the displacement of a from A and of b from B respectively. J is the Jacobian of the transformation for these relative co-ordinates. The functions χ_α and χ_β are the distorted waves and are an approximation of the true wave functions. The distorted waves are calculated from an optical potential that fits the energy averaged elastic scattering in the entrance and exit channels. They describe the relative motion of the pair a,A (asymptotically with relative momentum k_α) before the collision, or of the pair b,B (with k_β) after the collision. Asymptotically, the χ have the form of plane- plus scattered wave, and in the absence of a Coulomb field can be represented:

$$\chi^{(+)}\left(\vec{k}, \vec{r}\right) \rightarrow exp\left(i\vec{k}.\vec{r}\right) + f(\theta)\, exp\frac{(ikr)}{r} \tag{2.3}$$

The superscripts (+) and (-) indicate the usual outgoing or ingoing boundary conditions respectively.

In the optical model approximation, the distorted waves are generated from a Schrodinger equation:

$$\{\nabla^2 + k^2 - \left(\frac{2\mu}{\hbar^2}\right)[U(r) + U_c(r)]\}\chi(k, r) = 0 \tag{2.4}$$

where U(r) is the optical model potential, U_c the Coulomb potential and μ is the reduced mass of the interacting pair. When the particles a and b have spin, a spin-orbit coupling term is included in U(r) and the functions χ become matrices in spin space $\chi_{m'm}$, where m is the z component of spin.

2.1.1 The interaction kernel

The remaining factor in the amplitude (2.1) is the matrix element of the interaction causing the perturbation, taken between the internal states of the colliding pairs. Written as an interaction kernel it becomes:

$$I_{\beta\alpha} = \langle \beta \mid W \mid \alpha \rangle = \langle \Phi_B \Phi_b \mid V - U \mid \Phi_A \Phi_a \rangle \tag{2.5}$$

V is the complicated effective interaction between nucleons in the nuclei and U is the distorting potential. The integration, in terms of the bra-ket notation is over all co-ordinates independent of r_α and r_β. This nuclear matrix element is a function of r_α and r_β and plays the role of an effective (generally non-local) interaction for the transition between the distorted waves $\chi_\alpha^{(+)}$ and $\chi_\beta^{(-)}$. The matrix element contains all the data on nuclear structure, angular momentum selection rules and even the type of reaction being considered. The "physics" of any reaction then appears in the magnitude and radial shape of the nuclear matrix element.

If we consider the entrance channel α as that in which the incident nucleon interacts with the target nucleus, and the exit channel β as that in which the residual nucleus interacts with the outgoing nucleon(s) then the transition amplitude (2.1) lends itself to a prior and post interaction representation[2]. In both the post and prior forms of the interaction the auxiliary potentials U are not arbitrary but describe elastic scattering in the α and β channels to the approximation that the coupling effects between the α and β channels can be ignored. This approximation can be represented in the prior form

as:

$$U_\alpha = (\alpha \mid V_\alpha \mid \alpha) \tag{2.6}$$

where $(\alpha \mid V_\alpha \mid \alpha)$ is a potential that describes elastic scattering in the α channel.

With V_α and V_β as the prior and post effective interactions, an additional approximation is introduced by replacing their diagonal matrix elements by simple optical model potentials whose parameters are adjusted to fit observed elastic scattering at the appropriate energies. If these fits are good the corresponding optical model wave functions will be the same as the true wave functions outside the region of interaction, and should not differ much in the surface or peripheral region where the direct reaction occurs predominantly. There is no guarantee, however, that the optical model wave functions and the true wave functions will be similar in the interior or strong interaction region. Hence an optical model assumption may introduce errors insofar as the interior region may make important contributions to the transition amplitude.

Even with the calculation of the interaction kernel $I_{\beta\alpha}$, the amplitude (2.1) remains a 6-dimensional integral over r_α and r_β. The computation of the amplitude is simplified to a 3-dimensional integral by taking r_β parallel to r_α or $r_\beta = \lambda r_\alpha$, so that the interaction kernel assumes the zero range form[9],[10]

$$I^{ZR}_{\beta\alpha} = F_{\beta\alpha}(r_\alpha)\delta(r_\beta - \lambda r_\alpha) \tag{2.7}$$

2.1.2 Spin representation

A multipole expansion of $I_{\beta\alpha}$, equivalent to breaking down the matrix elements into terms corresponding to angular momentum transfers between the various parts of the system that occur during the collision. Hence we

must take into account the transferred angular momentum:

$$\begin{aligned} J_B - J_A &= J_{BA} \\ J_b - J_a &= J_{ba} \\ J_{BA} + J_{ba} &= j \end{aligned} \tag{2.8}$$

If we define the nuclear spins and their z components as:

$$J_i m_i = j(i),\ i = A, B, a, b \tag{2.9}$$

then the interaction kernel can be written explicitly in terms of nuclear spins and their z components as:

$$I_{\beta j(B),j(b),\alpha j(A),j(a)}(r_\beta, r_\alpha) = J_{\beta\alpha} \int d\zeta_\beta \Phi_{j(B)}(x_B)^* \Phi_{j(b)}(x_b)^* W \Phi_{j(A)}(x_A) \Phi_{j(a)}(x_a) \tag{2.10}$$

where the the internal co-ordinates x are to be transformed to (ζ_β, r_β) with the Jacobian $J_{\beta\alpha}$.

The components of the integrand in (2.10) can be vector coupled according to Satchler[11], noting that the interaction W and the Jacobian $J_{\beta\alpha}$ are scalar quantities. Under rotation of the co-ordinates the wave function Φ_{JM} behaves like $(-1)^{J-M}\Phi^*_{(J-M)}$ and similarly for $\Phi^*_{(JM)}$. Hence the product $\Phi^*_{j(B)}\Phi^*_{j(A)}$ may be expressed as a sum of terms, each of which is vector-coupled to a resultant that behaves like the conjugate of a function with angular momentum $J_{\beta\alpha}$ and the entire kernel $I_{\beta\alpha}$ can be expanded as:

$$\begin{aligned} I_{\beta j(B),j(b),\alpha j(A),j(a)}(r_\beta, r_\alpha) = \Sigma_{J_{BA} J_{ba} l} \quad & \langle J_b J_a m_b - m_a \mid J_{ba} m_{ba} \rangle \\ \times\ & \langle J_B J_A m_B - m_a \mid J_{BA} m_{BA} \rangle \\ \times\ & \langle J_{ba} J_{BA} m_{ba} M_{BA} \mid l m \rangle \\ \times\ & (-1)^{J_A - m_A + J_a - m_a} G^m_{l J_{ba} J_{BA}}(r_\beta, r_\alpha) \end{aligned} \tag{2.11}$$

The multipole components $G^m_{lJ_{ba}J_{BA}}$ are defined by inverting the expansion (2.11) using the orthonormality properties of the coefficients. It can be shown[11],[12] that these multipole functions, under rotation, behave like the conjugates of spherical harmonics $Y^{m^*}_l$ and in the zero range form are proportional to $Y^{m^*}_l$. In this case the quantum number l determines the parity change for the transition.

$$\pi_{\beta\alpha} = \pi_B \pi_b \pi_A \pi_a = (-)^l \tag{2.12}$$

Taking into account the isospin representation, the kernel $I_{\beta\alpha}$ would then have additional Clebsch-Gordan coefficients [13],[14] and an additional summation over the the isospin transfer t.

2.1.3 Spectroscopic coefficient

It is often helpful to write the factor G in (2.9) as a product

$$G^m_{lJ_{ba}J_{BA}}(r_\beta, r_\alpha) = A^m_{lJ_{ba}J_{BA}} f^m_{lJ_{ba}J_{BA}}(r_\beta, r_\alpha) \tag{2.13}$$

This separation into a spectroscopic coefficient A and a form factor f is one of convenience so that standard form factors with simple normalizations may be used in the computation. A is usually chosen to include such quantities as fractional parentage coefficients[15] for the initial and final nuclear states and the interaction strengths.

2.1.4 The differential cross section

We are now in a position to write the differential cross section in terms of the the transition amplitudes $T_{\beta\alpha}$. Ignoring the isospin representation and taking an average over the initial spin orientation the differential cross

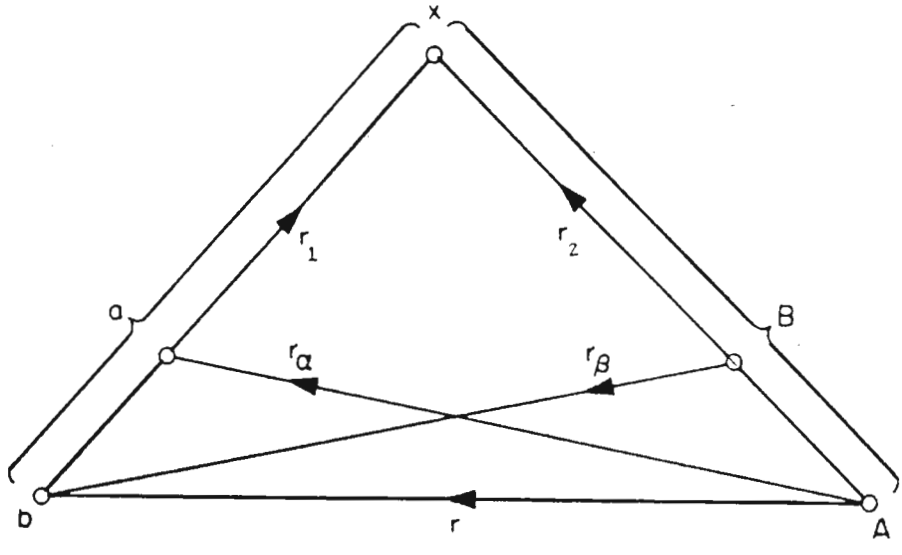

Figure 2.2: Coordinates for a three body model of a transfer reaction[9]

section is given by:

$$\frac{d\sigma_{\beta\alpha}}{d\Omega} = \frac{\mu_\beta \mu_\alpha k_\beta}{(2\pi\hbar)^2 k_\alpha (2J_A+1)(2J_a+1)} \sigma_{\beta\alpha}(\theta) \tag{2.14}$$

where the reduced cross section is

$$\sigma_{\beta\alpha}(\theta) = \Sigma_{\beta\alpha} \mid T_{\beta\alpha} \mid^2 \tag{2.15}$$

It has been pointed out that if the co-ordinates of the interaction kernel satisfy the condition that r_α and r_β are approximately parallel, then $I_{\beta\alpha}$ assumes the so- called zero-range approximation form. Evaluation of the transition amplitude without approximation generally involves finding corrections to the zero-range limit due to recoil or finite range effects. The most successful approach has been to use a type of Taylor expansion. We will not go into the details of these corrections except to mention that some of the most comprehensive discussion on the matter is presented by Santos[9] and involves the use of a three-body formalism for transfer reactions (see Fig 2.2).

The characteristics of cross section angular distributions(2.14) tend to be determined primarily by the transferred l- value. However, j- dependency in the cross section is sometimes possible and can affect the correlation between experimental and theoretical cross sections. As a spectroscopic tool, j- dependency in cross sections is largely empirical (Fig 2.3) and although the distorted waves method generally leads to an understanding of the effect, it is not to be relied on for the fine detail. There are three sources of j-dependence in the cross section angular distribution for one step transfers:

(i) The bound state wave function for the transferred particle has a radial component that will depend on j because of spin-orbit coupling in the binding potential. This effect is not expected to be significant.

(ii) Spin -dependency of the distorted waves due to spin-orbit coupling in the distorting potential.

(iii) The internal states of the particles may contain non-S state components, such as the D state of the deuteron[16].

It is well known[17] that for a given l value the j- dependency manifests itself as a cross section with the same geometrical profile for $j = l + \frac{1}{2}$ as for $j = l - \frac{1}{2}$ but with a possible difference in magnitude of up to 50%. Thus for instance, in l= 2 transfers with dominant j= $\frac{5}{2}$ transfer, an underestimate in the spectroscopic factor can result if there is significant j= $\frac{3}{2}$ transfer.

To summarize, we have shown that the nuclear matrix element contains all the "physics" necessary to analyze direct reactions and contains the overlap between initial and final states. The measure of overlap between the states is given by the spectroscopic factors, which can be derived from the interaction kernel $I_{\beta\alpha}$. For light ion reactions such as the (n,d) reaction the transition can be approximated using a zero-range potential.

To achieve agreement between theory and experiment the cross section is

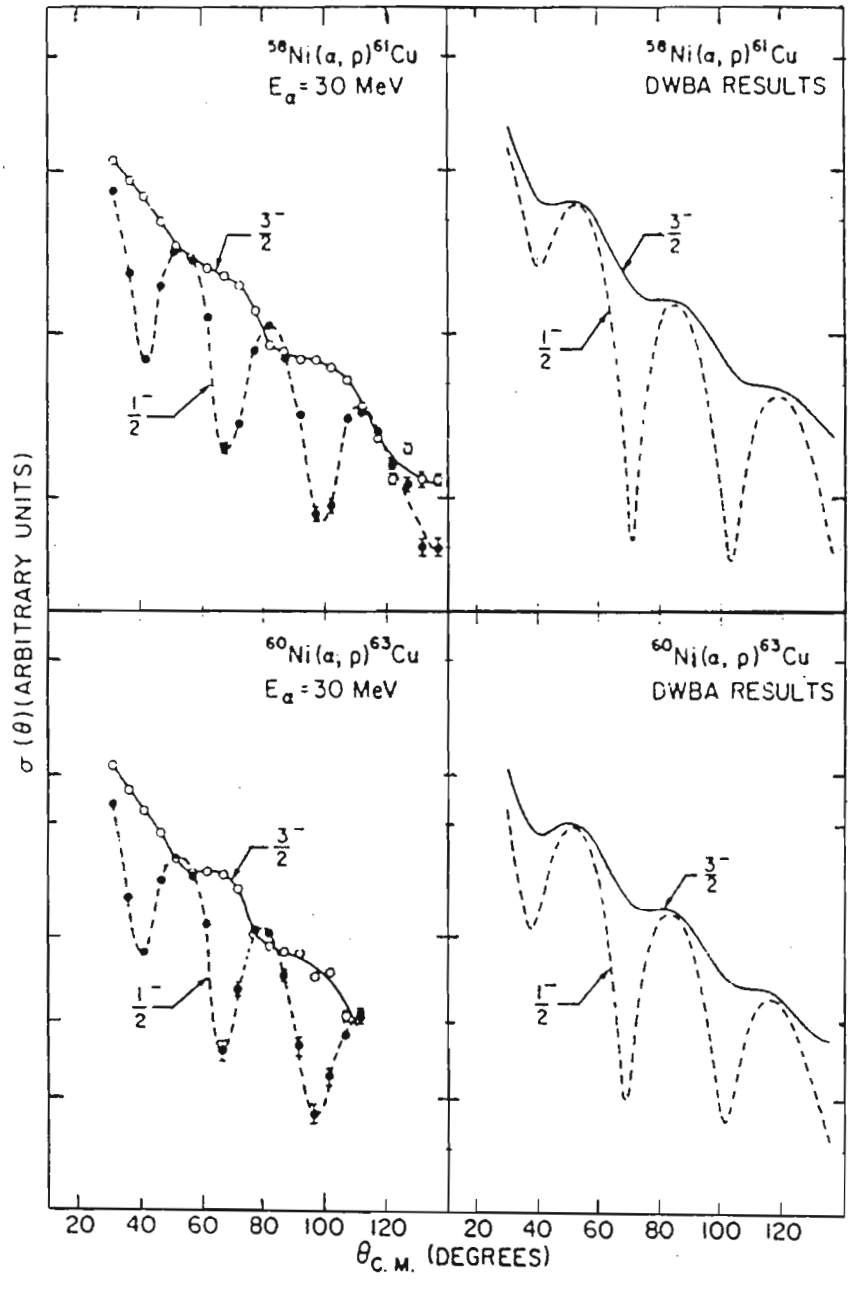

Figure 2.3: Angular distributions for l=1 transfers showing strong j-dependence[18]

calculated in a model space generated by optical potentials with various l-values until the shape of the cross section is found to agree. The spectroscopic factor is then revealed as the ratio of experimental to theoretical cross sections. The agreement of the zero-range theory with the experimental angular distributions is generally quite convincing (Fig.2.4). Thus one can assume that the determination of the spins and parities l, j and $(-)^l$ are fairly sound. However, the normalization by which the spectroscopic factors are determined must be carefully chosen. A comparison of the zero-range theory with the full finite-range calculation for light ions is usually reassuring[19].

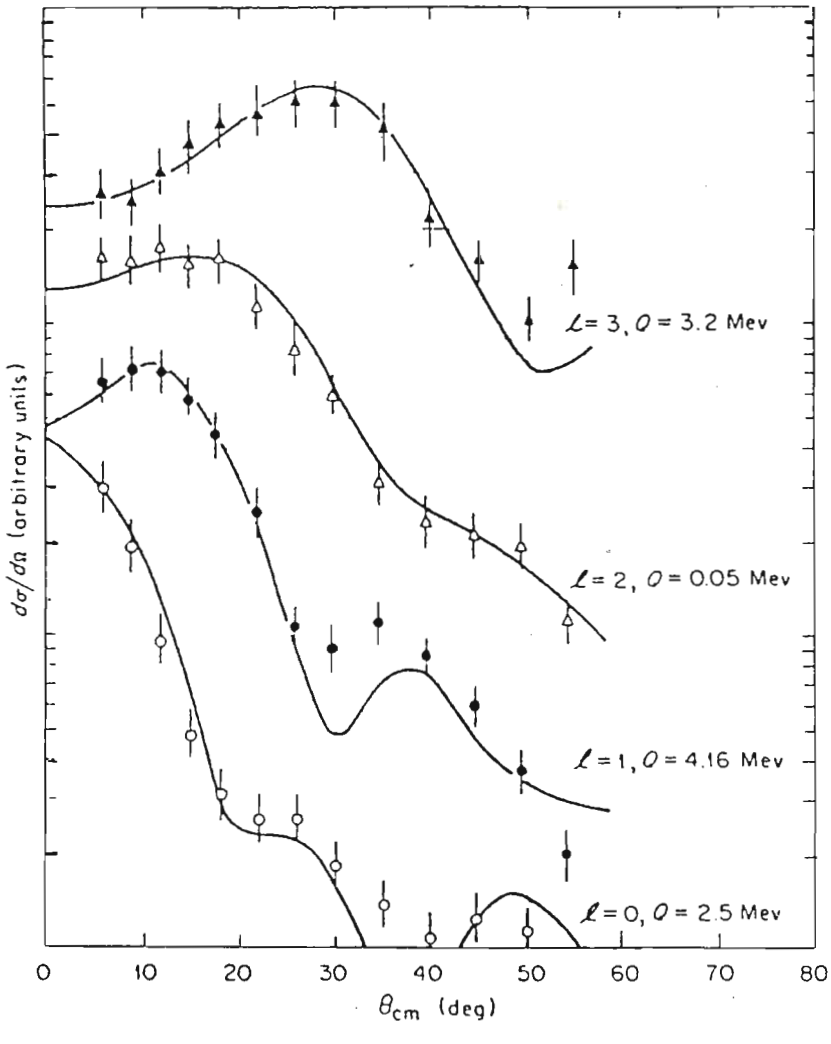

Figure 2.4: The identification of the transferred angular momentum from the shape of the angular distribution for deuteron stripping[20]

2.2 The Optical Model

An optical model is a model of the effective interaction between two nuclei; it attempts to replace the complex many-body problem of the interaction of two nuclei by the simpler picture of two bodies interacting through a potential.

The history of the optical model is long and varied and goes back as far as Bethe's calculations[21] for the scattering of nucleons by a real potential. Le Levier and Saxon [22] introduced damping by allowing the potential to be complex and Feshbach et al.[23] examined the total and reaction cross sections for the interaction of neutrons with nuclei for a large range of energies and nuclei. The optical model derives it's name from the use of a complex potential; just as the interaction of light with a medium which is both refractive and absorbtive can be treated by allowing the refractive index to become complex, so the scattering and absorption of nucleons by nuclei can be represented by a complex potential.

The optical potentials can be determined either by phenomenological analysis of experimental data or by a more fundamental calculation starting from the nucleon-nucleon interaction. The former uses relatively simple physical arguments to establish the form of the potentials and the approximate values of its parameters, then relying on comparison with experimental data to fix these parameters precisely. The fundamental or microscopic calculation is much more complex and has only recently been developed to the stage where it can give reliable quantitative results[24],[25]. While there is good agreement between the phenomenological analysis and the microscopic description, the fundamental calculation has thrown new light on apparently anomalous results in the phenomenological analysis[26],[27],[28], thus unifying both into a coherent whole. There is evidence that the optical model is not

merely a phenomenological model but has important basis in microscopic theory[24],[25].

2.2.1 Radial variation of the optical potentials

At sufficiently high energies the effective nucleon-nucleon (N-N) interaction reduces approximately to the free N-N scattering amplitude. Hence the optical potential can be realistically based on the N-N interaction, which is short range and falls exponentially with distance. If we assume a local approximation for the N-N interaction then in the entrance channel α the elastic scattering is given approximately by an optical potential that is just the N-N interaction averaged over the distribution of nucleons in the colliding nuclei $a + A$

$$U(r_\alpha) = \int\int \rho_a(r_i)\rho_A(r_j)t(r_{ij})dr_i dr_j \tag{2.16}$$

where $r_{ij} = r+r_i-r_j$, $t(r_{ij})$ is the local N-N interaction and ρ_a or ρ_A is the density distribution in the ground state of a or A. If the projectile a is single nucleon (eg.neutron) then ρ_a disappears and the expression for U reduces to a single integral.

Thus, to first approximation, we expect the optical potential to have a radial variation that follows the nuclear density quite closely, with a somewhat larger radius reflecting the finite range of the N-N interaction. This can be conveniently represented by an analytic expression of the Woods-Saxon form[29]

$$\begin{aligned} f(x) &= \frac{1}{1 + exp\left[\frac{(r-R)}{a}\right]} \\ x &= \frac{(r-R)}{a} \end{aligned} \tag{2.17}$$

where R is the radius and a the surface diffuseness parameter. Since nuclear radii are generally proportional to $A^{\frac{1}{3}}$ where A is the mass number, the radius is

$$R = r_o A^{\frac{1}{3}} \tag{2.18}$$

where r_o is independent of A. Then the real part of the optical potential is given by

$$\begin{aligned} ReU(r) &= -V f(x_v) \\ x_v &= \frac{r - R_v}{a_v} \end{aligned} \tag{2.19}$$

where V is the potential well depth. The subscript v indicates a volume optical potential. The potential goes to -V as $x \rightarrow -\infty$ and to zero as $x \rightarrow +\infty$. Additionally, the form of the potential (Fig. 2.5) shows that $f(0) = \frac{1}{2}$ and $f(x)$ falls from 0.9 to 0.1 as x goes from -2.2 to +2.2.

The imaginary absorbtive potential takes into account all the non-elastic processes that remove flux from the incident channel and is assumed to have a volume or surface form or both. The volume term is defined as in 2.17 and 2.18

$$\begin{aligned} ImU(r) &= -W f(x_w) \\ x_w &= \frac{r - R_w}{a_w} \end{aligned} \tag{2.20}$$

where R_w and a_w need not have the same values as for the real potential. The imaginary volume potential is supplemented by a surface peaked potential of the radial derivative form

$$ImU(r) = 4W_D \frac{df(x_D)}{dx_D}$$

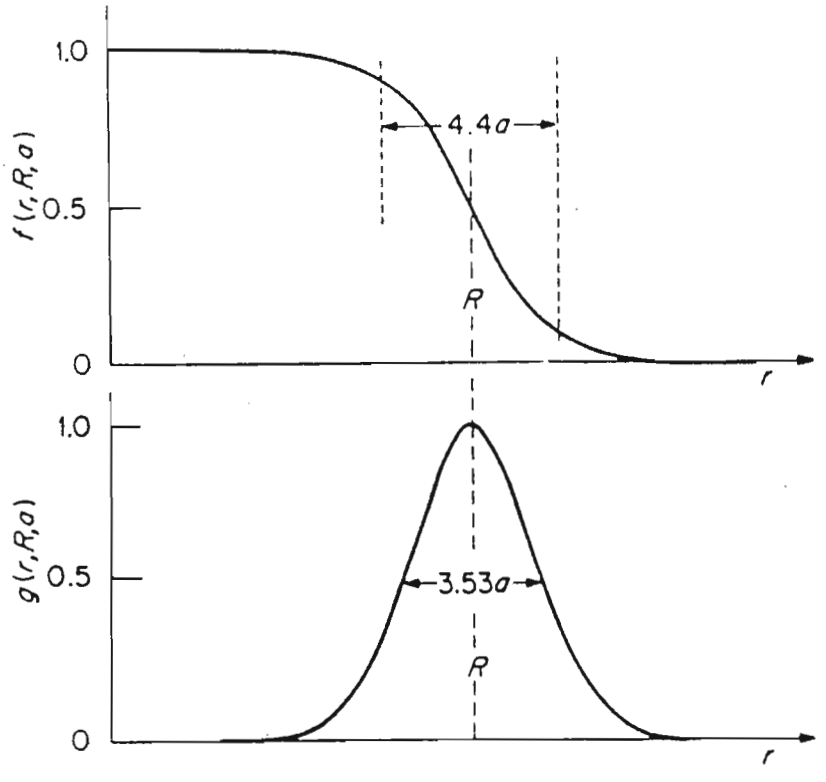

Figure 2.5: The form of the optical Woods-Saxon $f(x)$ and Woods-Saxon derivative potential $g(x)$ for $R/a \sim 9$(from Ref[1]).

$$= -4W_D \frac{exp(x_D)}{(exp(x_D)+1)^2} \tag{2.21}$$

The factor 4 is included so that Im U(r) has a peak value of W_D at r=R_D. When both the surface and imaginary terms are used one usually assumes $R_W = R_D$ and $a_W = a_D$.

2.2.2 The spin-orbit term

As a result of the finite dimensions of the nuclei in both the entrance and exit channels, the spin orientation of the interacting nuclei with respect to the incoming or outgoing particles is of significance. The simple vector spin-orbit coupling must assume a form $\vec{L}.\vec{s}$ where $\vec{s}$ is the spin of the nuclei. In analogy with the corresponding term for atoms, the spin-orbit potential is given by

$$\begin{aligned} U_{so}(r) &= (\frac{\hbar}{m_\pi c})^2 (V_{so}) \frac{1}{r} \frac{df(x_{so})}{dr} \vec{L}.\vec{s} \\ x_{so} &= \frac{r - R_{so}}{a_{so}} \end{aligned} \tag{2.22}$$

The Woods-Saxon function $f(x_{so})$ is defined as in 2.17. Usually $R_{so} \neq R_v$ and $a_{so} \neq a_v$. The factor $(\frac{\hbar}{m_\pi c})^2 = 2.00$ fm^2 is included so that V_{so} may be expressed in MeV. For high energies($\geq$ 100MeV) V_{so} is sometimes allowed to become complex. This term is expected to be strongest near the surface of the target or residual nuclei as it is only near the surface that the interaction between projectiles and nuclei is likely to depend on the direction of their relative momentum. Tensor couplings are possible for $s \geq 1$ and is found to appear in deuteron related scattering.

2.2.3 The Coulomb potential

If we consider the interaction of charged particles and nuclei, it is important to take into account the Coulomb potential due to the charges. The potential due to an incident nucleon of point charge $Z_a e$ interacting with a target nucleus of charge $Z_A e$, uniformly distributed over a sphere of radius

R_{ch} is given by

$$\begin{aligned} U_c(r) &= \frac{Z_a Z_A e^2}{r}, r > R_{ch} \\ &= \frac{Z_a Z_A e^2}{2R_{ch}}(3 - \frac{r^2}{R_{ch}^2}), r < R_{ch} \end{aligned} \tag{2.23}$$

The above expression is simplistic in assuming spherical symmetry for the nuclei and does not take into account the diffuse nuclear surface. A more accurate expression uses the charge density distribution for the incident projectile and target nucleus and is represented in the double folded model (Fig. 2.6) as

$$U_c(r_\alpha) = \int\int \rho_{chA}(r_1)\rho_{cha}(r_2)\frac{1}{r_{12}}dr_1 dr_2 \tag{2.24}$$

$$r_{12} = \mid r_\alpha + r_2 - r_1 \mid \tag{2.25}$$

This reduces to the simpler single folded expression with $\rho_{ch(a)} = e$ if the incident particle is a single nucleon.

2.2.4 Energy variation of the optical potentials

The parameters of the optical potentials usually vary monotonically with energy, and are similar for neighbouring nuclei. It is generally the real and imaginary potentials that have an energy dependence; that of the real part of the potential is essentially linear and decreases with energy (Fig. 2.7). The decrease | V| with energy can be attributed in part to the N-N interaction. At low energies the long range attraction contributes primarily to the optical potential. As the energy increases the repulsion at short distance in the fundamental N-N collisions partially overcomes the attractive contribution.

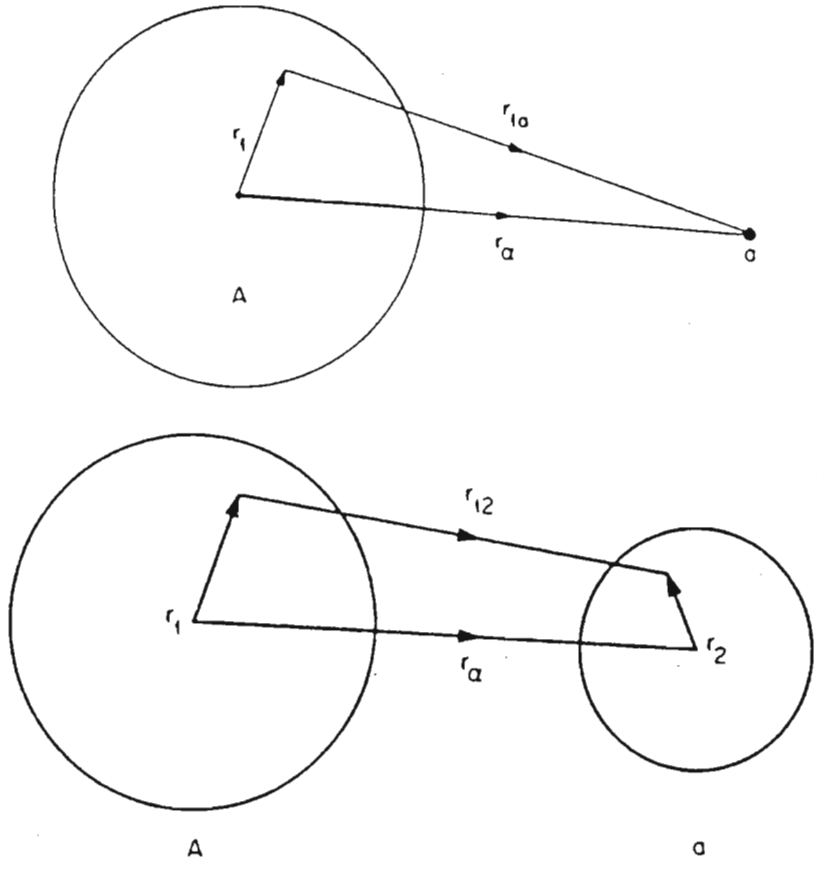

Figure 2.6: Coordinates used for single and double folding models[1]

The imaginary part of the potential increases in magnitude with the energy to take into account the increasing cross sections of the various non-elastic reactions. The increase in | W| corresponds to the opening of more channels that drain flux from the elastic channel. The energy variation of the potential is usually attributable to the variation of the Hartree-Fock field and is associated with the non-locality of the potential.

2.2.5 Nonlocality of the optical potential

In addition to the energy dependence, the structure of the optical potential exhibits an explicit non-local character. This non-locality stems from the intrinsic non-local character of the effective interactions as well as from

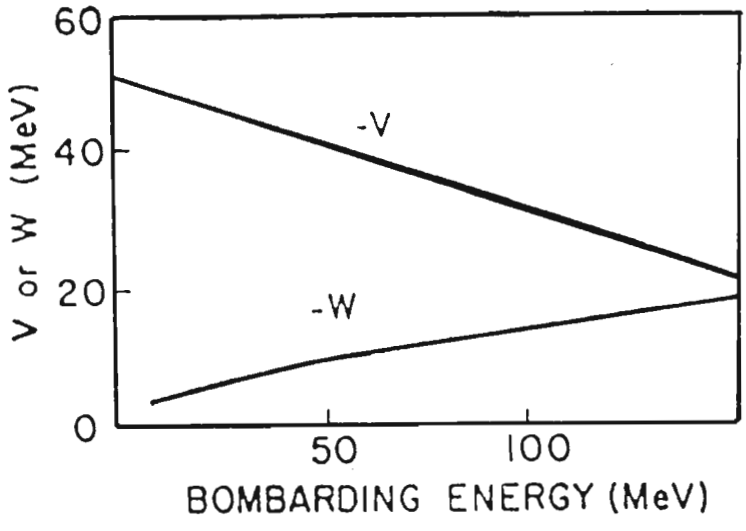

Figure 2.7: Schematic behaviour of real and imaginary parts of optical potential as a function of energy

Ω

the anti-symmetrization between projectile and target nucleons. When the model potentials are taken to be local an element of error is induced in calculating the transition amplitude. This is corrected for with an adjustment to the form factor by a multiplicative correction factor. This correction is represented as

$$W_{NL}(r) = exp\left[\frac{2\beta_i^2 m_i V_i(r)}{8h^2}\right] \tag{2.26}$$

for each particle. The V_i are the local potentials while β_i are the nonlocal parameters, taken from Kunz[30] as being 0.85 for nucleons and 0.54 for deuterons.

2.2.6 Finite range corrections

A full finite range calculation for the (n,d) reaction will involve a six-dimensional integration for the transition amplitude. The calculation is vastly simplified if one reduces the six- dimensional integral to a two-dimensional one by assuming a zero-range form for the overlap of incident and picked-up nucleon. In the full finite range calculation for the (n,d) reaction the overlap of incident neutron and picked-up proton can be written as

$$D(r_{pn}) = (\Phi_n \mid V_{pn}\Phi_p) \tag{2.27}$$

where V_{pn} is the sum of all proton-neutron interactions and generally includes spin factors. The function D has a short range for light ions and in the zero-range approximation is replaced by a delta function

$$D(r_{pn}) = D_o\delta(r_{pn}) \tag{2.28}$$

The delta function does, however, introduce very strong correlations between the different functions that are varying rapidly in the interior region, resulting in an overestimation of the contributions from the nuclear interior. The effect of the zero-range approximation is to introduce an additional locality in the potential which must be offset by introducing an additional energy dependence i.e. the finite range effects are replaced by a zero-range approximation in which the potential is a local, energy dependent one, sometimes referred to as the local energy approximation (LEA)[31],[32].

References

1.) G.R. Satchler, Direct Nuclear Reactions (Oxford Science Publications, Oxford, 1983).

2.) N. Austern, Direct Nuclear Reaction Theories (Wiley Interscience, New York, 1970).

3.) N.K. Glendenning, Direct nuclear reactions (Academic Press, London, 1983).

4.) J.B. Marion and J.L. Fowler, Fast neutron Physics (Interscience, New York, 1963).

5.) W. Tobocman, Theory of direct nuclear reactions (Oxford Univ. Press, New York, 1961).

6.) S.T. Butler, Phys. Rev. 106 (1957) 272.

7.) S.T. Butler, N. Austern and C. Pearson, Phys. Rev. 112 (1958) 1227.

8.) E. Rost, Phys. Rev. 128 (1962) 2708.

9.) F.D. Santos, Nucl. Phys. A212 (1973) 341.

10.) M.A. Nagarajan, Nucl. Phys. A209 (1973) 485.

11.) G.R. Satchler, Nucl. Phys. 55 (1964) 1.

12.) G.R. Satchler, Nucl. Phys. A91 (1967) 75.

13.) A.M. Lane, Nucl. Phys. 35 (1962) 676.

14.) S. Contach and D. Robson, Nucl. Phys. A209 (1973) 301.

15.) P.J. Brussard and P.W.M. Glaudemans, Shell model applications in Nuclear Spectroscopy, (North Holland, Amsterdam, 1972).

16.) L.L. Lee and J.P. Schiffer, Phys. Rev. B136 (1964) 405.

17.) F. Meurders, P.W.M. Glaudemans, J.F.A. Van Hienan and G.A. Turimer, Z. Physik A276 (1976) 113.

18.) L.S. August, P. Shapiro and L.R. Cooper, Phy. Rev. Lett. 23 (1969) 537.

19.) R.M. Drisko and G.R. Satchler, Phys. Lett. 9 (1964) 342.

20.) B.L. Cohen, R.H. Fulmer and A.L. McCarthy, Phys. Rev. 126 (1962)

698.

21.) H.A. Bethe, Phys. Rev. 47 (1935) 94.

22.) R.E. Le Levier and D.S. Saxon, Phys. Rev. 87 (1952) 40.

23.) H. Feshbach, C.E. Porter and V.F. Weisskopf, Phys. Rev. 96 (1954) 448.

24.) J.P. Jeukene, A. LeJeune and C. Mahaux, Phys. Rep. 25C (1976) 83.

25.) J.P. Jeukene, A. LeJeune and C. Mahaux, Phys. Rev. C16 (1977) 80.

26.) G.E. Brown, J.H. Gunn and P. Gould, Nucl. Phys. 46 (1963) 598.

27.) M. Bauer et al., J. Phys. G.: Nucl. Phys. 8 (1982) 525.

28.) H. Ngo, Nucl. Phys. A390 (1982) 198.

29.) R.D. Woods and D.S. Saxon, Phys. Rev. 95 (1954) 577.

30.) P.D. Kunz, University of Colorado, 1978, unpublished.

31.) F.G. Perey and D.S. Saxon, Phys. Lett. 10 (1964) 107 .

32.) J.K. Dickens et al., Phys. Lett. 15 (1965) 337.

Chapter 3

Experimental details

The $^{27}Al(n,d)^{26}Mg$ and $^{56}Fe(n,d)^{55}Mn$ reactions have been studied using a 6 MV Van de Graaff accelerator (at the National Accelerator Centre, Faure, Cape Province). Incident neutrons at 21.6 MeV were produced by the $^{3}H(d,n)^{4}He$ reaction in a tritium gas cell at low pressure. The Van de Graaff accelerator produces a 5.0 MeV deuteron beam which is directed onto the tritium gas cell. The high Q value of the (d,t) reaction (17.5 MeV) results in neutrons of $\sim$ 22 MeV which are incident on the target foil.

The charged particle reaction products emanating from the target foil were detected in the McMurray - BharuthRam spectrometer[1], specifically designed for the study of neutron - induced charged particle reactions. The measurements presented in this study are part of an on - going study of (n,d) reactions on different nuclei. Some of the experimental methods employed have been described previously[1][2].

In this chapter a discussion of some of the experimental details will be recounted but we will concentrate more on investigating the behaviour of the proportional counters. The general characteristics of multi-wire proportional counters will not be presented here except as relates specifically

to our system.

Angular distribution measurements for low yield nuclear reactions induced by fast neutrons have been difficult to make for several reasons: A low incident neutron flux resulting in a low yield nuclear reaction produces extremely long run times if conventional silicon surface barrier ΔE-E telescopes are used. Competing reactions, high background rates and neutron damage to detectors were also responsible for further complications in angular measurements. In the present setup, the spectrometer used partially resolves these problems.

The spectrometer and it's components are described in section (3.1), the setting up of the spectrometer in section (3.2), data acquisition in section (3.3) and data reduction in section (3.4). Although the detection system was designed for the study of the (n,p) reaction[3], it is well suited for a study of (n,d) reactions.

A comparison of the experimentally determined cross-section with the theoretically determined cross-sections from the Distorted Waves Born Approximation (DWBA) gives information on the nuclear structure of the target nuclei and the level structure of the residual nuclei. Experimental cross-sections were determined from the angular distributions of the outgoing deuterons.

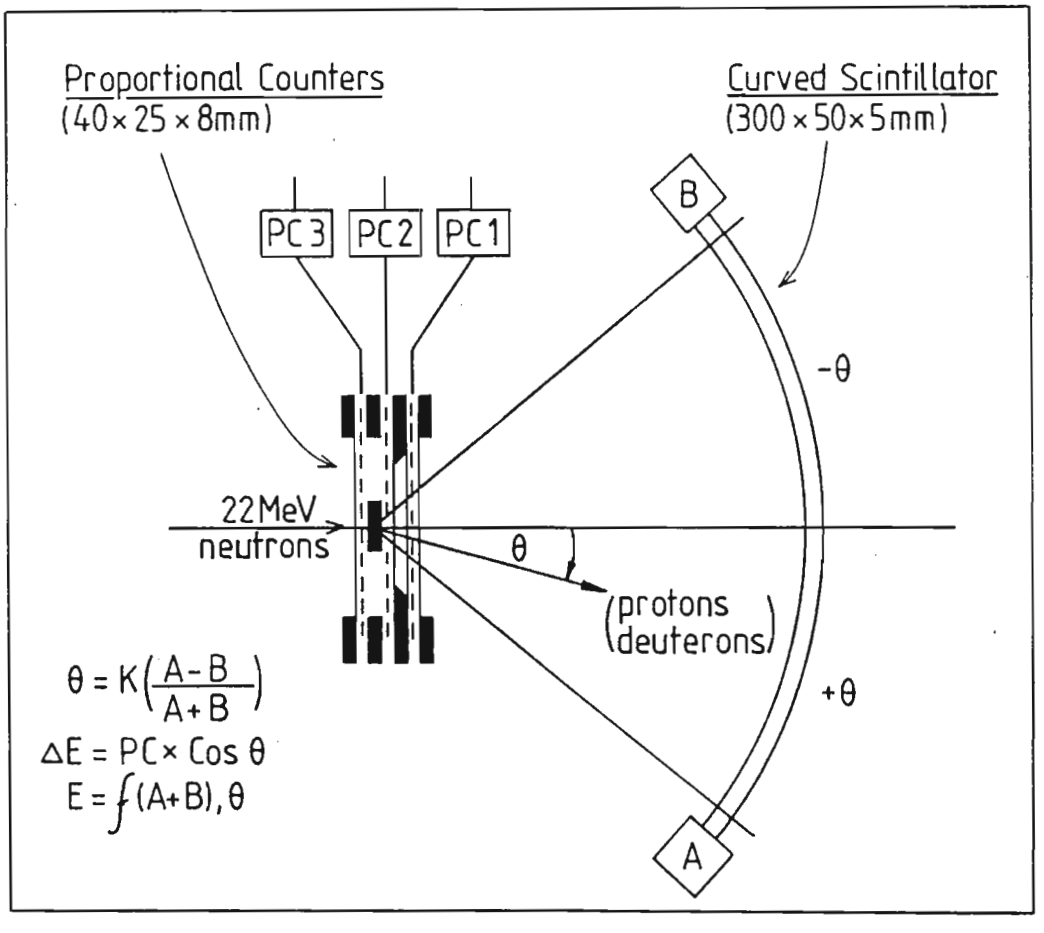

Figure 3.1: Schematic diagram of the spectrometer[1]

3.1 The particle spectrometer

A schematic diagram of the spectrometer is shown in Fig. 3.1. The spectrometer consists of three multi-wire proportional counters (PC3, PC2 and PC1) followed by a plastic scintillator. The target foil is sandwiched between proportional counters PC3 and PC2. PC3 is operated in anti-coincidence, PC1 and PC2 in coincidence with the scintillator to select only events originating in the target sample. A collimator in between PC1 and PC2 limits the effective height of the target sample to 12mm. The target is 10mm wide.

Proportional counters PC1 and PC2 act as two ΔE detectors and the scintillator as an energy, E, detector, thus providing ΔE-E particle identification. The spectrometer allows for the simultaneous accumulation of particle discriminated spectra over an angular range of 80^0 with an angle resolution of $\sim 5^0$ (FWHM). The energy resolution for deuterons is $\sim$ 0.7 MeV (FWHM).

The spectrometer is positioned on a level surface and the plane of the spectrometer is checked with a spirit level. The spectrometer has been used in a 0^0, -15^0 and a -25^0 position. This means that the midpoint of the scintillator is either at 0^0, -15^0 or -25^0 with respect to the incoming beam. This implies that for the symmetrical positioning the spectrometer scans an angular range of -40^0 to $+40^0$, whereas in the -15^0 and -25^0 position the range is -25^0 to $+55^0$ and -15^0 to $+65^0$ respectively. The angular positioning is determined precisely with the aid of a theodolite. The target is centred on the neutron beam by lining up the theodolite with the centre of the tritium cell and using this as reference to align the target on the zero degree neutron beam direction and to set the angular positioning of the whole spectrometer with respect to this direction.

3.1.1 The proportional counters

An expanded illustration of the proportional counter assembly is shown in Fig. 3.2. Constant flow multi-wire proportional counters(MWPC) were used in the present experimental setup. These have the advantage of providing more than one anode wire for pulse height determination. The number of wires in the proportional counter units have been varied from 3 to 15, each with a thickness of between 0.025mm and 0.05mm. The large number of wires increases the probability of background.

The proportional counters are 8mm thick with an active area $\sim$ 1000mm^2

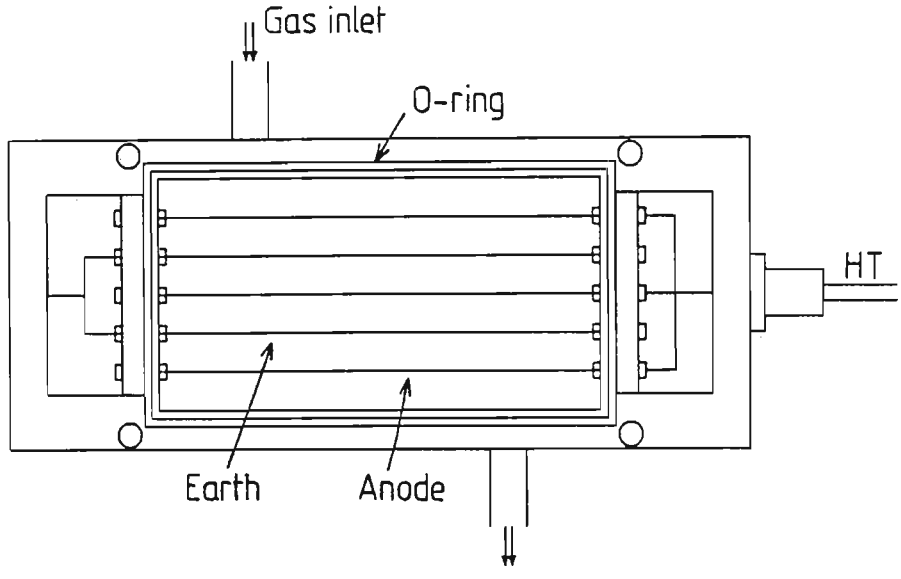

Figure 3.2: Schematic representation of a proportional counter

and are operated in continuous flow mode with a methane-argon mixture or carbon dioxide-argon mixture at atmospheric pressure. Gas inlet/outlet ports are situated diagonally across each other on the upper and lower walls of each PC to ensure adequate flushing of residual air and uniformity in the gas flow pattern. It is well known that the addition of small amounts of a polyatomic gas such as methane to a common fill gas such as argon suppresses photon induced effects by preferentially absorbing the photons in a mode which does not lead to further ionisation[4]. The timing resolution of the system is improved with a higher methane content, but this has the adverse effect of increasing the proton recoil yield which adds to the proton background underlying the deuteron spectra. A mixture of CO_2 - Ar was used in place of the methane mixture in PC2 and PC3, giving much lower proton background without affecting the counter energy response. However, analysis of the background reveals a peak that is assigned to the $^{40}Ar(n,d)^{39}K(gnd)$ and $^{16}O(n,d)^{15}N(gnd)$ reactions which may occur in the CO_2-Ar gas in PC2 and therefore be detected as an event in the spectrometer. The external frame of PC3 is covered by a 0.025μm Al foil

while PC3 and PC2 are separated by the sample and flanking thin wires. PC2 and PC1 are separated by two 0.0125μm Al cathodes that cover the two sides of a 2mm brass collimator as well as the rear face of PC1. The thin foils are adequate to maintain gas purity and field homogeneity while minimizing energy degradation and background production by the beam striking the windows. The gas purity in the chambers were maintained by securing the windows with O-ring seals that prevent contamination from outside water vapour, O_2 and other gases. The thin wires flanking the sample strip (10mm$\times$ 25mm) extend the cathode wall between PC3 and PC2 counters. The EHT of the proportional counters was about 1150V to provide suitable gas gain for the detection of particle energy loss. The behaviour of the counters was checked by observation of the 17.5 keV X-ray peak using an Am-Mo source. The spectral shape of the energy calibration peaks is shown in Fig. 3.3. A straight line calibration with these X-rays indicates linear behaviour in the low energy region. It must be pointed out however, that the X-ray sources effectively probe small elements of the proportional counter volume and that local variations will be averaged out when observing the counter response to penetrating protons or deuterons.

In a study of the pulse height response of the proportional counters using a ^{55}Fe X - ray source it was found that the pulse height and resolution spread is sensitive to the geometry of the proportional counters.

Starting with a total of 11 wires a distance of 2mm apart, the following features have been investigated for these PC's:
i) all wires at High Tension (HT) and the walls of the PC as earth,
ii) alternate HT and earth wires,
iii) increasing the distance between the side HT wires and the side walls, thereby decreasing the field strength in these regions,
iv) increasing the length of the chamber along the wires and decreasing the relative importance of end effects (near the insulators).

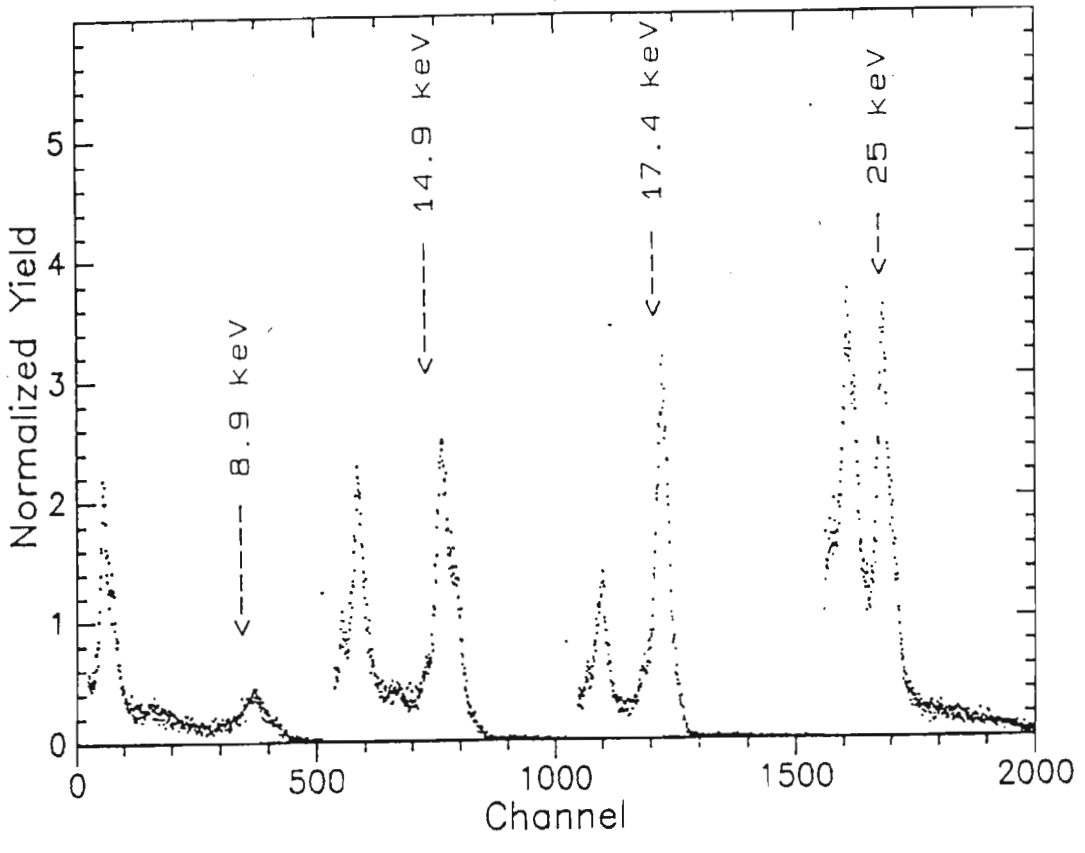

Figure 3.3: Energy calibration spectra for the proportional counters

v) Varying the number and spacing of the wires.

It was found that the number of wires, the distance between wires and the distance of side wires to the wall were of importance for a uniform response over the detectors active area. It was noted that uniform response and good spectral shape was achieved by removing every alternate wire and then alternating HT and earth wires i.e. half the wires were removed. This behaviour can be understood if one considers the mode of detection of the PC. After an event occurs at some place s at time t_0 the electrons drift toward, and avalanche at the anode wire. The electrical signal multiplies in the high field region near the wire. The major factor in particle energy measurement must be a uniform multiplication at all points along the anode wire. A uniform multiplication factor implies a high field region

which is independent of position or orientation along the anode wires. The most symmetrical arrangement is therefore likely to give the best position insensitivity to the energy resolution. The detector design as finally used separates the flat detector into approximately square cross-section regions around each anode wire.

With a large active area and few HT wires the difference in pulse height along the wires and across the full active area is minimal i.e. the PC has uniform response over its entire active area. The detector end geometry was also modified to further reduce the effect of the end insulators.

The position and flow sensitivity of the MWPC was investigated by placing a copper sheet over the face of a sample PC. A ^{55}Fe X-ray source provides adequately collimated X-rays so that holes in the copper sheet define nine positions along the PC as shown in Fig. 3.4. The following were investigated:

i.) position sensitivity using a 10% CH_4 -90% Ar mixture,

ii.) reversing the direction of gas flow from that in (i),

iii.) replacing 10% CH_4 -90% Ar with a 5% CO_2 -95% Ar mixture.

A plot of channel against position number is shown in Fig. 3.5. From the plot we observe that the pulse height (channel) varies with position; this is generally true for all three cases. The deviation is within reasonable limits and does not differ by more than 5% from the adjacent readings. A possible explanation stems from differences in the distance between anode and earth wires and anode and chamber wall and corresponding changes in central field strengths

Although the gas flow pattern and flow rate may be of importance it was found that for both flow directions the highest pulse was recorded along the lower chamber wall so that this effect is not attributable to a gas flow

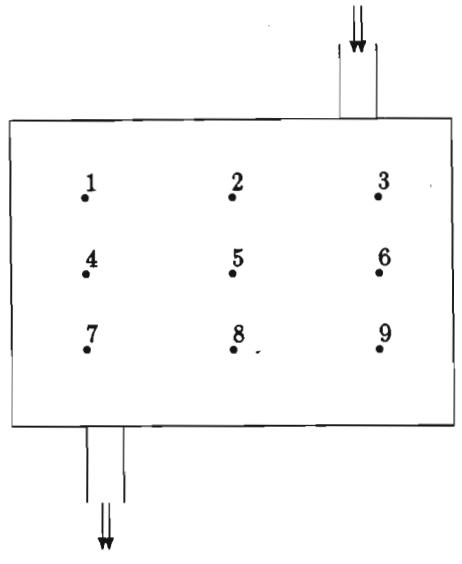

Figure 3.4: Position sensitivity of proportional counters

direction . Significant operating parameters which can affect energy resolution are the gas purity, gas pressure and stability of the high voltage applied to the chambers. Trace quantities of electronegative gases can also significantly reduce the gas multiplication[4] and introduce fluctuations in the pulse amplitude as well as create numerous low energy spurious pulses. Changes in gas pressure(ambient pressure) of a few percent can also be of significance. Variations in the applied voltage can drastically affect the pulse amplitude and thus voltage supplies must be well regulated to preserve the long term energy resolution of the proportional counter.

The degradation of proportional counters filled with argon-methane has been investigated by Smith et.al.[5]. A drop in gain accompanied by the formation of a double peak in the pulse height spectrum is an indication of the formation of polymerised methane on the wire that reduces the usefulness of the PC. However, this is known to occur at very high count rates and is not expected to be significant in our situation.

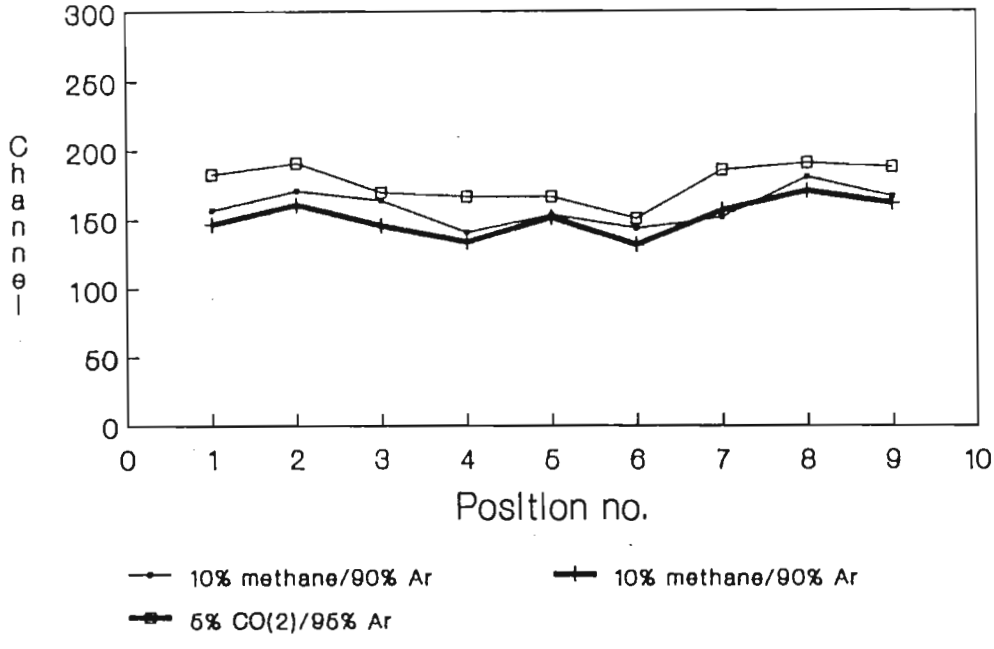

Figure 3.5: The position sensitivity of the proportional counters for low energy X-rays

3.1.2 The scintillator

The plastic scintillator is 5mm thick, 50 mm high, 300mm long and has a radius of curvature of 200mm. It therefore subtends an angle of more than 80^0 at the target. The energy signal, E, is obtained by summing the output from the two photomultipliers at the ends of the scintillator (see Fig. 3.1).

The energy determination of a detected particle depends on the stopping power of the particle in the scintillator. The scintillator was designed to stop 25 MeV protons. Reducing the scintillator thickness for the deuteron energy range of interest(8-18 MeV) would decrease the background count rate but could cause a deterioration in the energy resolution of the system. The response function of the scintillator to deuterons in air and in vacuum is shown in Figure 3.6.

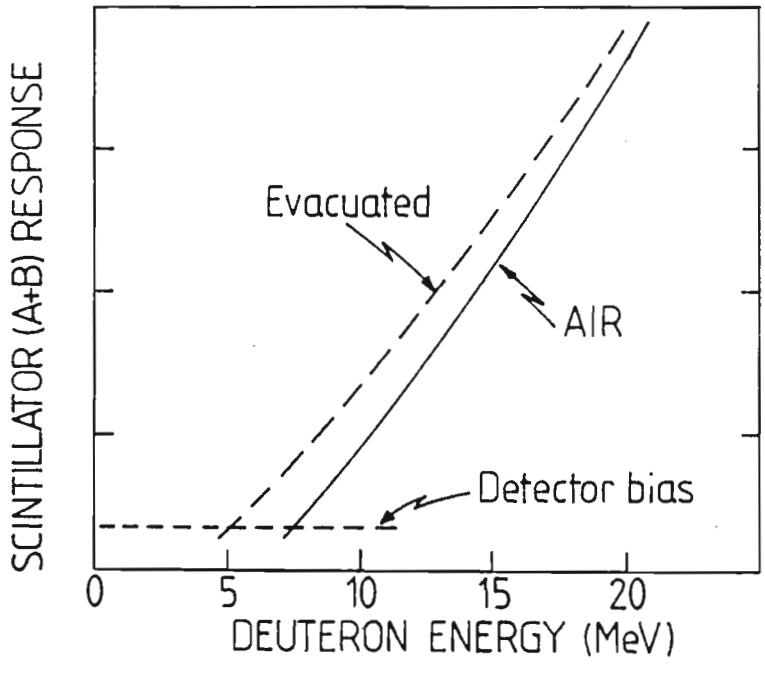

Figure 3.6: Response function of scintillator to deuterons in air and in vacuum[1]

The scintillator is optically coupled to the photomultipliers with a clear silicone grease and good optical contact is maintained with the use of transparent O-rings that retain the contact. Overflow reservoirs for topping up the silicone grease are situated on top of the perspex light guides that hold the scintillator to the phototubes (Fig 3.7). The scintillator was viewed at its' end with a Hamamatsu R329 twelve stage phototube was used in conjunction with a E934 Hamamatsu base. The system was found to be very stable and showed gain drifts of less than 2% over a 2 week period. As small fluctuations in the high voltage supply can produce large gain fluctuations it is very important that the EHT supplies are regulated.

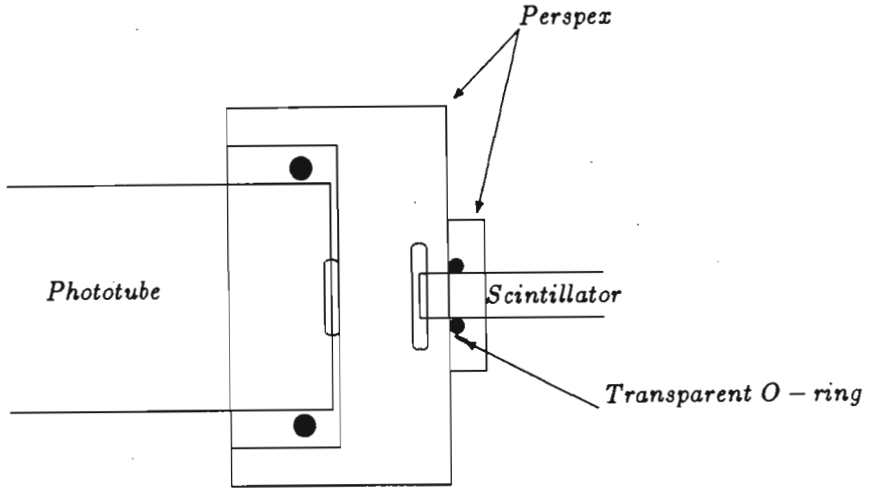

Figure 3.7: Schematic representation of scintillator contact at the phototubes

3.1.3 Electronics

A diagram of the electronic system, based on standard fast-slow timing systems, is shown in Fig. 3.8.

The proportional counters PC1 and PC2 and the scintillator have both slow and fast outputs. For PC1 and PC2 a pulse fed from the preamplifiers into the spectroscopic amplifiers is divided into a bipolar (timing) and unipolar (energy) output. The bipolar pulses are passed through timing single channel analysers (TSCA's) which use the bipolar cross-over for timing. The fast outputs from the TSCA's become the start pulses for the two time to amplitude converters (TAC's).

The anode pulses from the photomultipliers at A and B at the ends of the scintillator are amplified and processed similarly to those from the PC's. The amplifier bipolar outputs are added together. The combined (A+B)

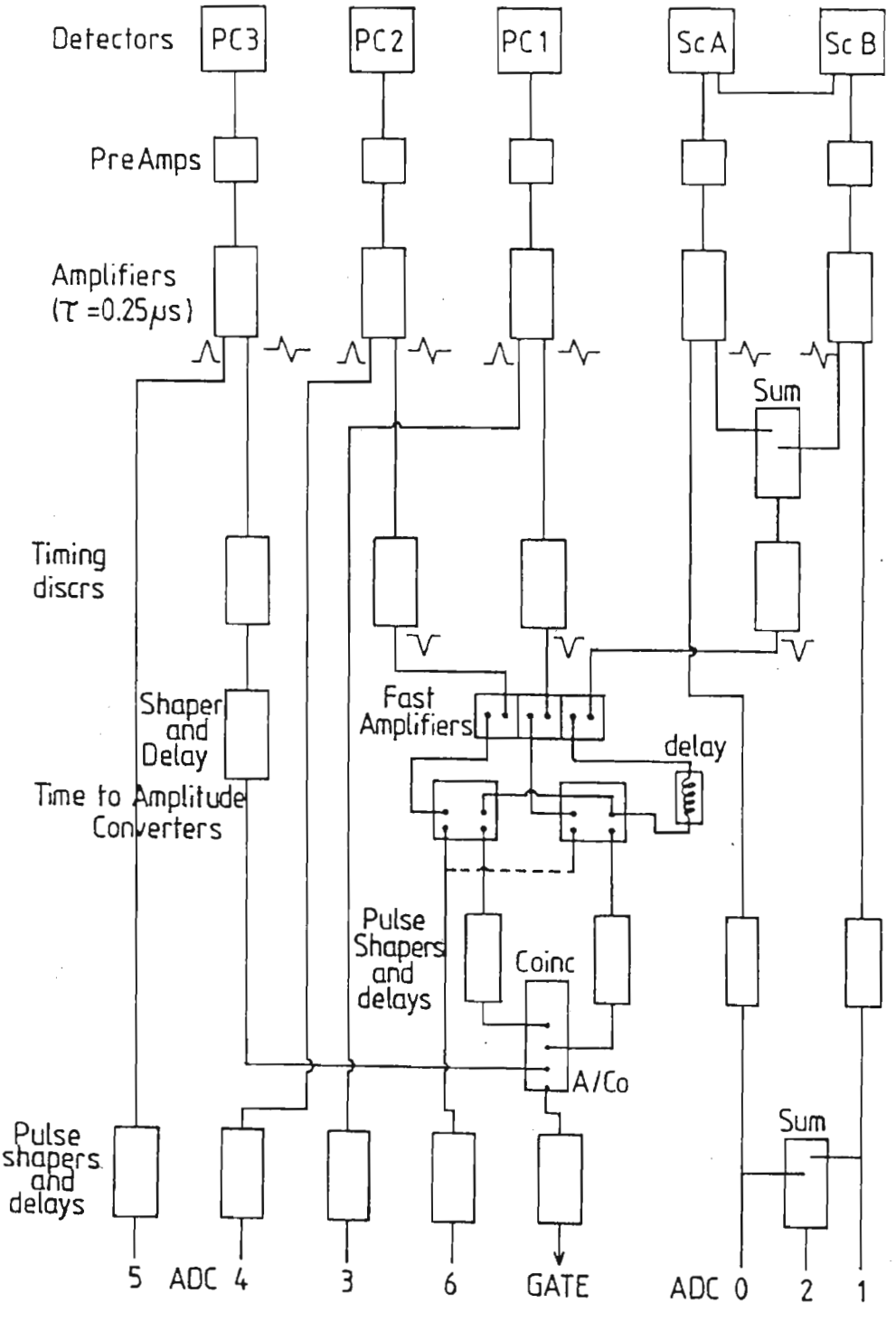

Figure 3.8: Electronic details

bipolar pulse is fed to a TSCA which provides the stop signal for each TAC. Linear gating of the coincidence peaks in the TAC outputs provides two of the coincidence gates, which indicate a particle event in the spectrometer. The requirement that timing pulses from PC3 must be in anticoincidence with the PC1/(A+B) and PC2/(A+B) coincidence gates serves to eliminate the background of particles which originate behind the sample (or those that move backward through the spectrometer, if any such particles are generated). The output of the coincidence unit, after being delayed and shaped, is used to gate all the analogue to digital converters (ADC's) which are interfaced to a computer based data acquisition system[6].

Unipolar pulses from the proportional counters PC1, PC2 and PC3 provide the energy loss (ΔE) pulses and the unipolar pulses from the scintillator, A and B, are also combined to form a (A+B) or residual energy pulse. After being delayed and biased the PC and scintillator pulses from the spectroscopic amplifiers are transmitted through gates that are opened by the output pulse of the fast coincidence unit. Two dimensional displays of PC vs (A+B) for the proportional counters are used to monitor the data accumulation. A two dimensional display of A vs B monitors the angular spread of the observed events.

3.2 Setting up the spectrometer

3.2.1 The proportional counters

The proportional counters were set using the 17.5keV X-rays from a Am-Mo source placed behind the proportional counter sandwich on the side of PC3. It was found that adjusting the X-ray peak pulse to $\sim$ 1.0 Volt set the amplifier pulse height range suitably for detection of the proton and deuteron ΔE pulses.

3.2.2 The scintillator-photomultipliers

The scintillator-photomultipliers were set up using a ^{207}Bi source which emits internal conversion electrons of $\sim$ 1 MeV energy. The source could be inserted close to the centre position (0^0) of the scintillator behind a light-tight thin foil. Two other monitor positions are provided at $+35^0$ and -35^0 along the scintillator length. The ^{207}Bi source was used to balance the photomultiplier outputs A and B and provide a precise monitor (as required) of the A and B gains and the scintillator angular response.

3.2.3 Using a 5.5 MeV proton beam

On-line setting of the fast timing requirements (i.e. discriminator levels and delays) was achieved with a 5.5 MeV proton beam from the accelerator. For this calibration the tritium gas cell is replaced by a snout with a thin Havar window. The protons pass through the proportional counters and get into the scintillator. All delays are adjusted so that the TSCA unipolar fast outputs are approximately in coincidence. The time relations between the proportional counters and the scintillator was measured and adjusted

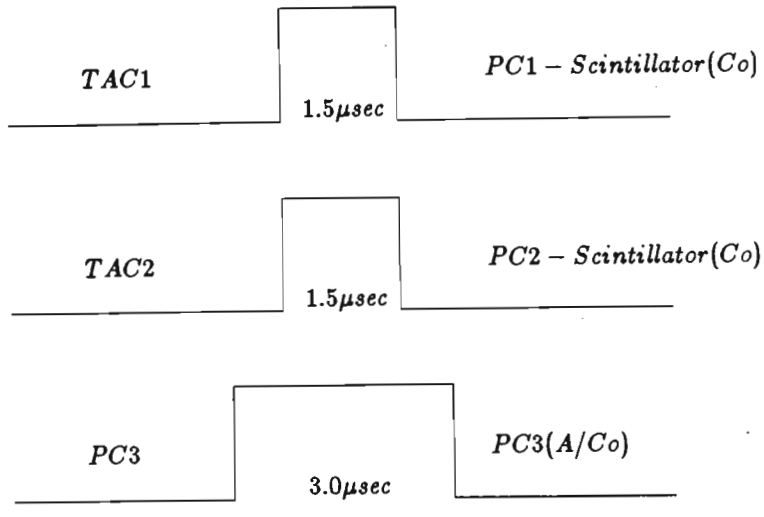

Figure 3.9: Coincidence timing conditions

to ensure that the stop pulse to the TAC's arrives after the start pulses. The anti-coincidence/coincidence conditions are then met by delaying the outputs of the TAC's to satisfy the conditions shown in Fig. 3.9.

To ensure that the ADC slow inputs arrive after the gate pulse rising edge by $\sim 0.5\mu$sec an additional timing adjustment was made to the PC1, PC2 and scintillator slow pulses. This condition is shown in Fig. 3.10.

3.2.4 Position determination in the scintillator

The position determination in the scintillator is set with a ^{207}Bi source in a 0^0 position (scintillator midpoint). The gains for the photomultipliers A and B are set so that the ^{207}Bi source produces equal peaks for A and B at the midpoint of the scintillator.

Position determination in the scintillator is based on light attentuation along the scintillator which cause the outputs of the photomultipliers at the ends of the scintillator at A and B to be position sensitive. The vari-

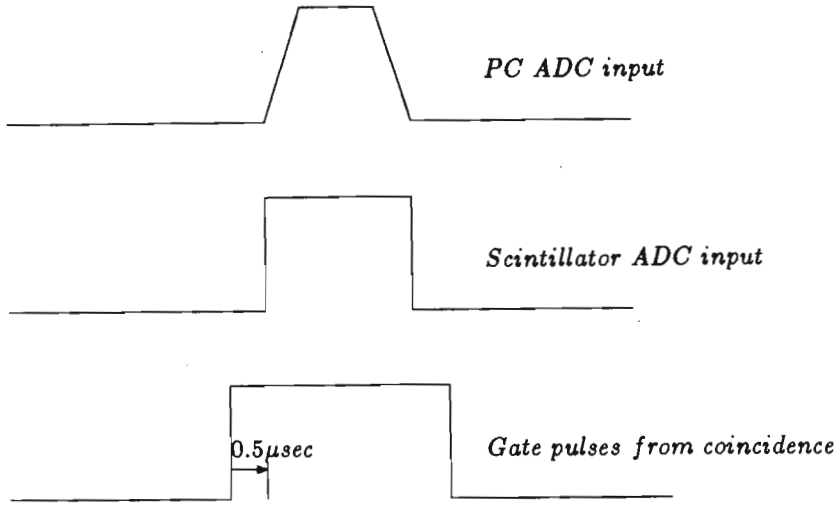

Figure 3.10: The gate timing conditions

ation of each output A or B with position is not strictly linear nor purely exponential and the summed output (A+B) is also to a smaller degree position dependent. It was found empirically that the function $\frac{A-B}{A+B}$ was nearly linear with position along the scintillator at least from $+35^0$ to -35^0. The value of $\frac{A-B}{A+B}$ for the outputs A and B following the detection of an event in the scintillator then defines the position of that event. Figure 3.11 was obtained from measurements using the ^{207}Bi source.

The position measurement is finely adjusted by observing recoil protons from a perspex sample bombarded by 21.6 MeV neutrons. These protons are more reliable than the ^{207}Bi electrons as a position check as they cover the particle energy range for which the scintillator is being used. In fact good agreement is obtained between these two methods. The slow outputs from the ADC's are displayed on a two dimensional A vs B display and the A and B gains and zero offsets are adjusted to produce a display symmetrical about the diagonal of A vs B. This reduces angle slewing as a function of particle energy.

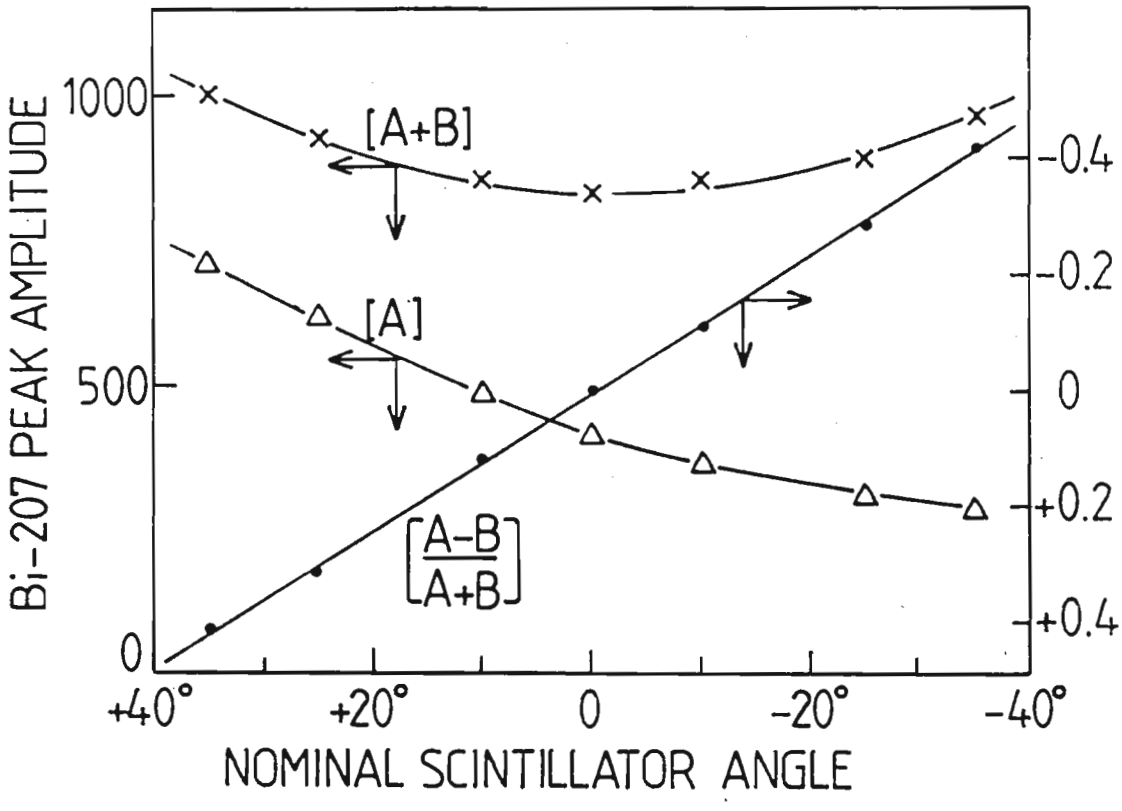

Figure 3.11: Position determination in the scintillator[1]

The position resolution of the system is checked by screening the scintillator with a thick absorber with slits at angles of $\pm 6^0$, $\pm 18^0$, $\pm 30^0$ and $\pm 38.5^0$. The 0^0 position is centred on channel 100 of the spectrum and the symmetry of proton spectra from a perspex sample is observed. It can be seen from Fig. 3.12 that the proton spectra at the scintillator are very symmetrical and have good position resolution. There is also very little slewing as a function of energy. From the available evidence, position determination with the simple $[\frac{A-B}{A+B}]$ function is good out to $\pm 35^0$ of the spectrometer but deviates close to the end of the scintillator strip (the 38.5^0 peaks are seen at a nominal 45^0).

In the data analysis the angle for each event is computed from

$$\theta = K\left(\frac{A-B}{A+B}\right) + 100 \qquad (3.1)$$

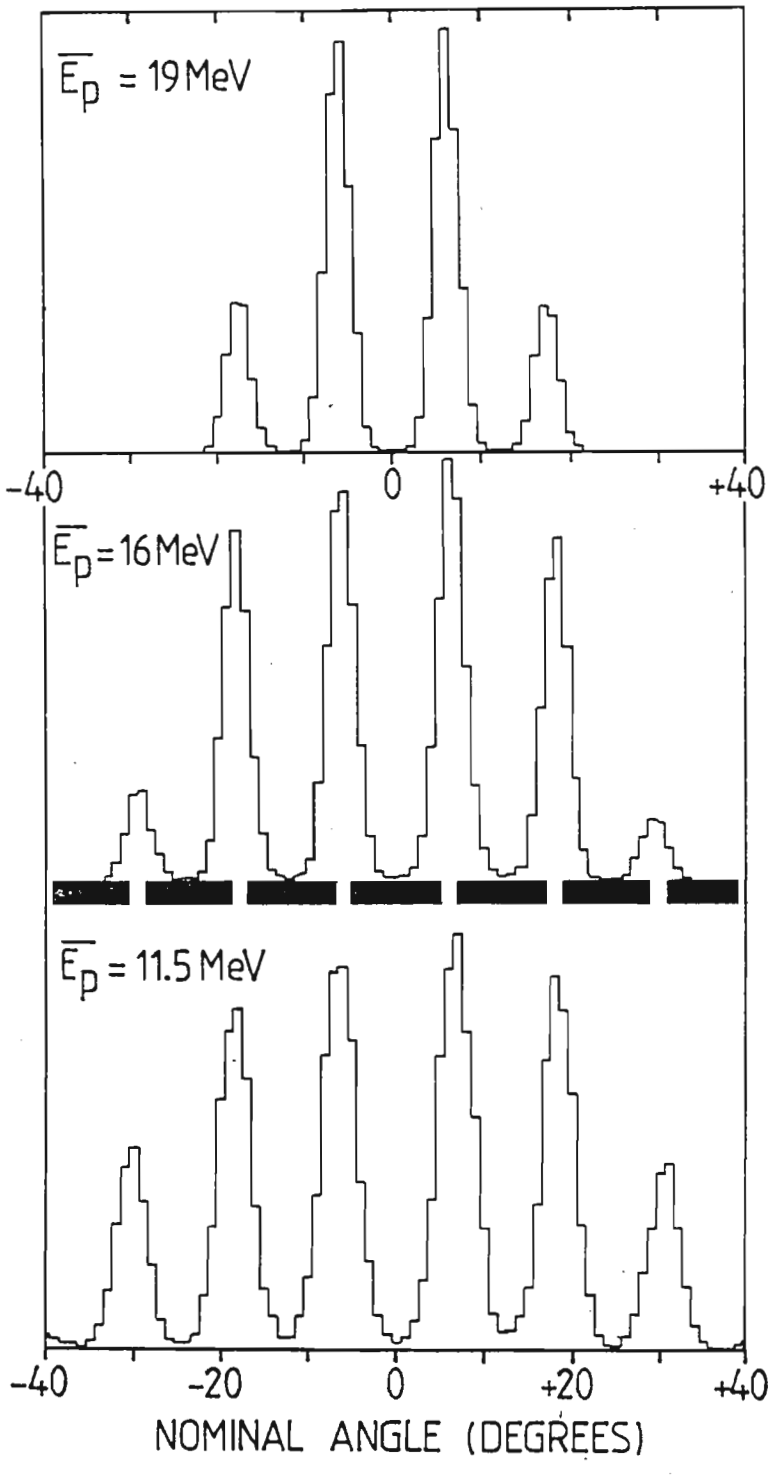

Figure 3.12: Position calibration spectrum with slits at the scintillator

so that an event at the midpoint of the scintillator (A=B) appears in channel 100. K is derived from source data such as that in Fig. 3.11.

3.2.5 Spectrometer geometry

The spectrometer has an intrinsic geometrical limitation in it's angular positioning of events and it's angular resolution. This geometry is determined primarily by the target height, tritium cell diameter, beam diameter, source to target distance and the scintillator height[2].

The geometry of the system from tritium cell to target is shown in Fig. 3.13. The tritium cell has a diameter of 10mm and a length of 30mm. The 5.0 MeV deuteron beam, with an effective diameter of 4mm enters the cell and all along the cell neutrons are produced at all angles. The energy of the neutrons is also fairly mono-energetic in the d-T reaction over a small angular range in the forward direction although low energy neutrons result from break-up reactions and d-d collisions.

As a compromise between reaction yield and angle spread (angular uncertainty) it was decided to fix the distance from the end of the tritium target to the target sample = 60mm and restrict the effective dimensions of the sample to 12mm height and 10mm width.

The significance of these limits can be seen in Fig 3.13 which shows that for any point in the sample there is a range of incoming neutron angles and a range of outgoing deuteron angles. Fig. 3.14 graphically illustrates the detection of (n,d) reaction angles as a function of position along a strip of the scintillator for an incoming neutron on the spectrometer symmetry axis.

The angle spread (angular resolution function) is a complex function of the

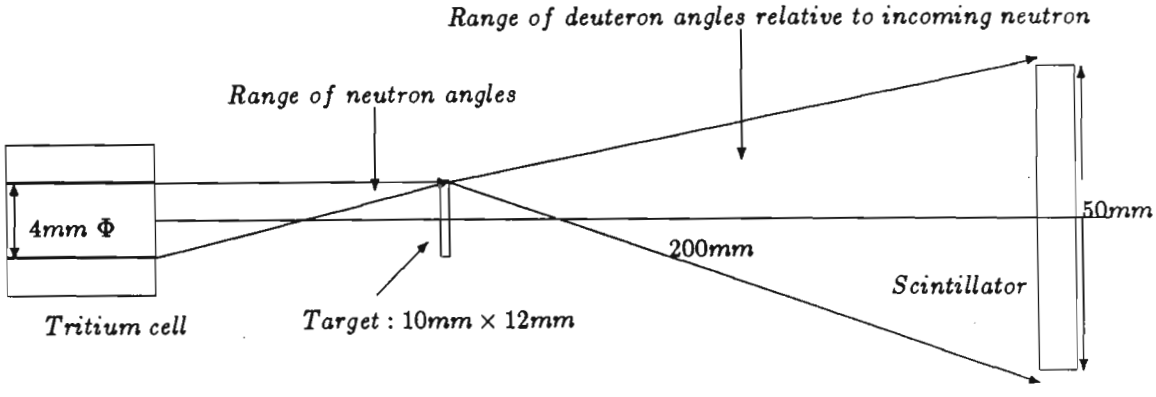

Figure 3.13: Experimental geometry

geometry of the tritium gas target and sample and scintillator dimensions. This has been computed. Results are presented in Table 3.1 for nominal $\pm 2.5^0$ strips of the scintillator and nominal $\pm 5^0$ strips of the scintillator.

If a strip of the scintillator corresponding to a 0^0 nominal angle, i.e. 0^0 with respect to the target-scintillator midpoint, is folded with a $\pm 2.5^0$ angle folding then the angular contributions to this region come from the range 0^0 to 8^0 for an angle of incidence of zero degrees at the axis of symmetry. Thus what was meant to be a $0^0 \pm 2.5^0$ strip collects solid angle contributions from the angle range 0^0 to 8^0.

Nominal angle	Angle limits	Angle range	Mean angle	FWHM
2.5^0		0.0^0-17.0^0	6.0^0	$\pm 4.0^0$
7.5^0		0.0^0-20.5^0	9.0^0	$\pm 4.2^0$
12.5^0		3.5^0-24.5^0	13.5^0	$\pm 4.4^0$
17.5^0	$\pm 2.5^0$	8.5^0-29.0^0	18.2^0	$\pm 4.4^0$
22.5^0		13.5^0-33.5^0	23.1^0	$\pm 4.5^0$
27.5^0		18.5^0-38.5^0	28.0^0	$\pm 4.5^0$
35.0^0		26.0^0-45.5^0	35.4^0	$\pm 4.5^0$
50.0^0		41.0^0-60.0^0	50.3^0	$\pm 4.5^0$
5.0^0	$\pm 5^0$	0.0^0-20.5^0	7.5^0	$\pm 4.7^0$
15.0^0		3.5^0-29.0^0	15.9^0	$\pm 5.4^0$
25.0^0		13.5^0-38.5^0	25.5^0	$\pm 5.5^0$
35.0^0		25.5^0-46.0^0	35.4^0	$\pm 4.7^0$

Table 3.1: True scattering angles and spread for nominal angular bins[2]

3.2.6 Particle energy determination

The energy of a particle in the scintillator is a function of the scintillator outputs A and B and can be represented as

$$E = f(A + B) \tag{3.2}$$

Corrections to the energy determination that are angle related can be obtained from an expression of the form

$$E = f(A + B, \theta) \tag{3.3}$$

The A+B curvature is corrected for angle θ by a binomial fit of (A+B) against θ given by

$$(A + B)_{corr} = A_1 + A_2(\theta) + A_3(\theta^2) \tag{3.4}$$

The polynomial fit is not executed by XSYS but is done separately. The variables A_1, A_2 and A_3 are also entered via the procedure SETPARMS.

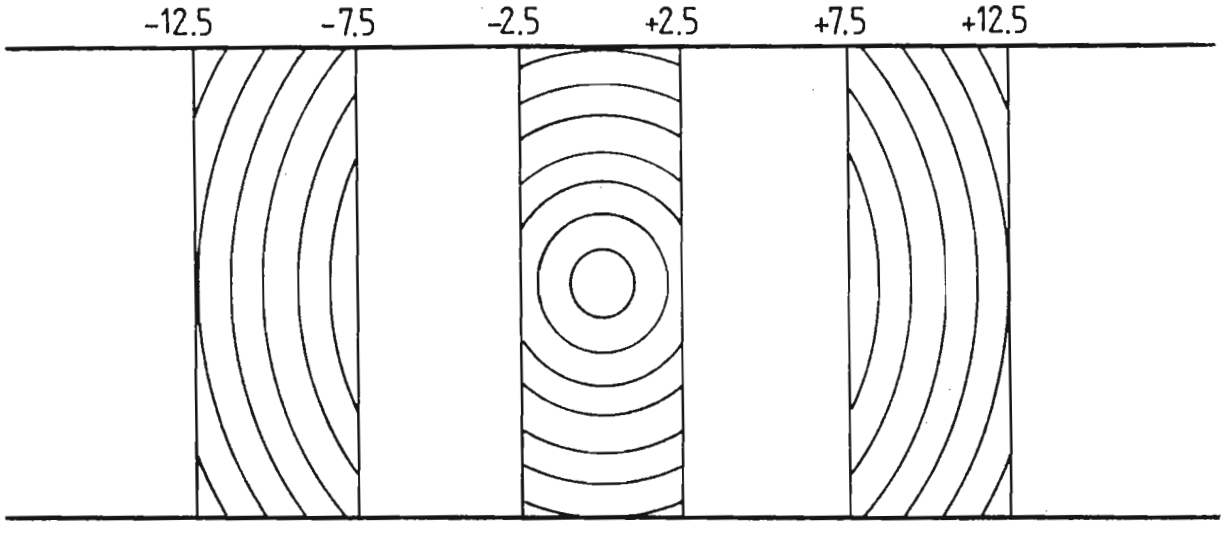

Figure 3.14: True scattering angles and spread for nominal angular bins on either side of 0^0 (from ref.[2])

A_1	1.0026
A_2	7.55×10^{-4}
A_3	1.99×10^{-4}

Table 3.2: Parameters for particle energy determination in the scintillator

The correct value of (A+B) that determines the energy for some event in the scintillator is then

$$E = (A+B)_{real} = \frac{(A+B)_{measured}}{A_1 + A_2(\theta) + A_3(\theta^2)} \tag{3.5}$$

The deduced values for A_1, A_2 and A_3 used for the ^{56}Fe(n,d) reaction is shown in Table 3.2.

As the particle spectrometer is operated in air separated from the proportional counters by thin foils, the energy (A+B) is the residual particle energy and not the total energy of the emitted particle.

Energy calibration of the system is achieved by replacing the target sample by foils of polythene (p-poly) and deuterated polythene (d-poly). These are bombarded by neutrons at $\sim$ 22 and 18 MeV to give a good spread

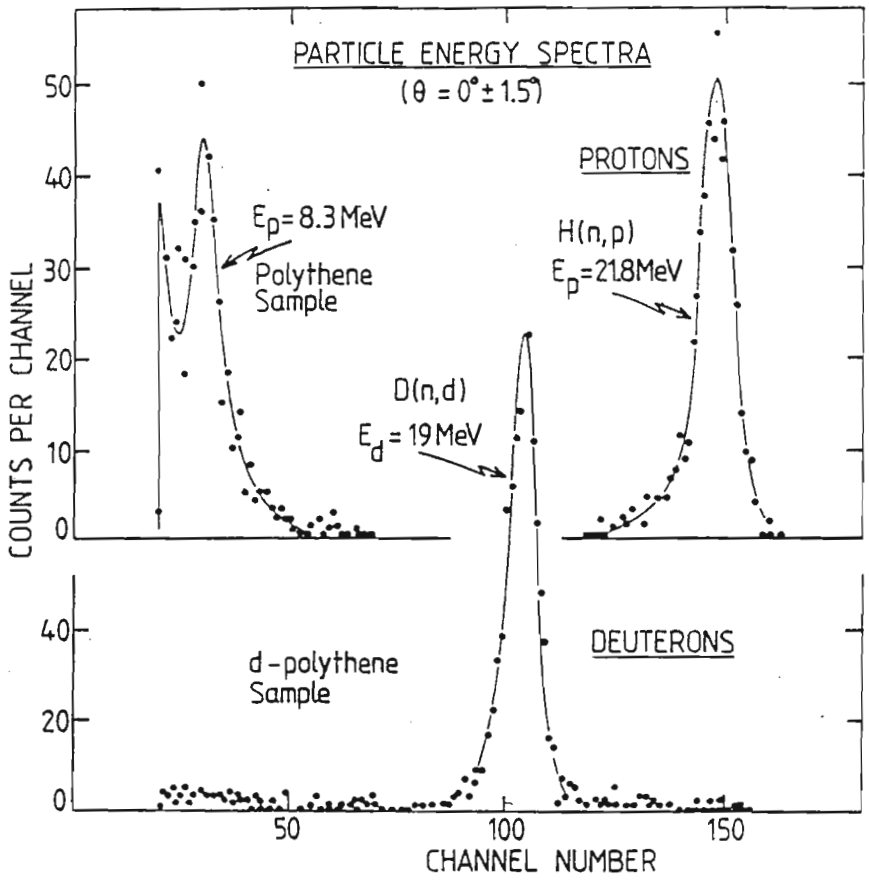

Figure 3.15: Particle energy spectra for polythene and deuterated polythene samples[1]

in the energy calibration. The multi-parameter spectra are particle-gated separately for protons and deuterons, respectively, and then angle-gated according to the determined 0^0 nominal position channel number and the required angle folding. The resultant energy spectra (Fig 3.15) then reveal calibration points for a energy vs channel number curve (Fig 3.16).

The channel number is obtained as the centroid of the peak from the p- or d-spectra and is computed by the analysis program. The energy of the outgoing particles is determined from a kinematical calculation of the energy of the reaction products as a function of reaction angle. Figure 3.17 shows the kinematic curve for d-poly.

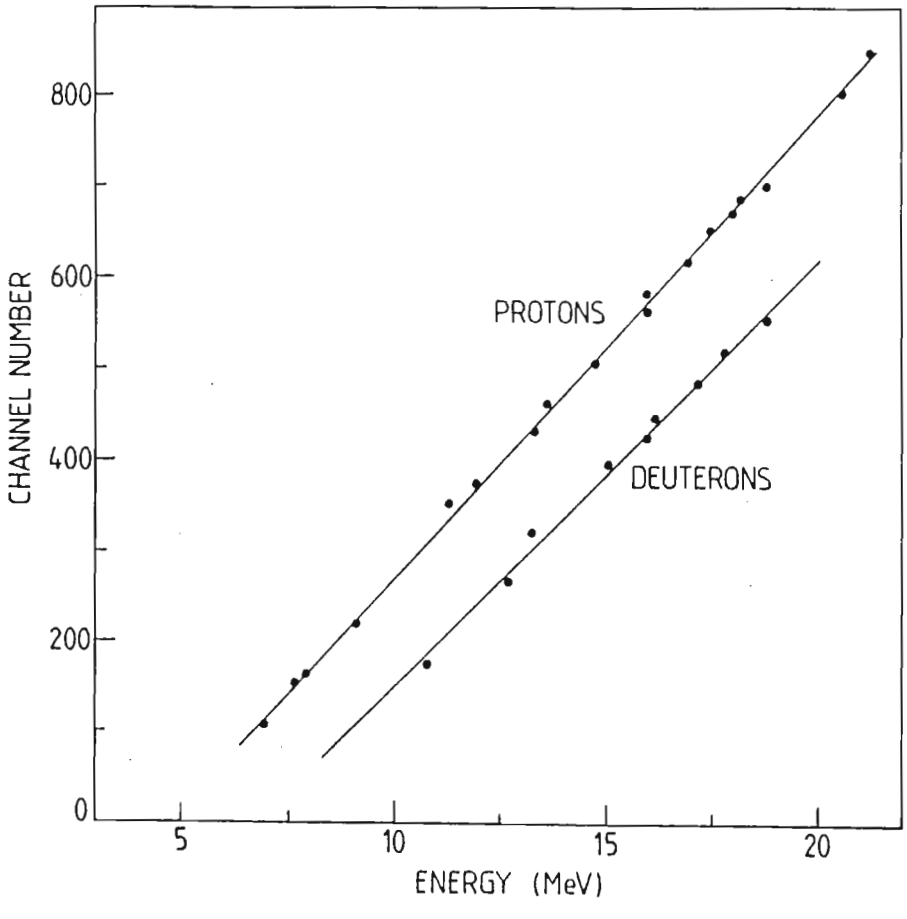

Figure 3.16: Deuteron and proton energy calibration curves

3.2.7 Energy loss in the proportional counters

The energy loss in the proportional counters, ΔE is computed as

$$\Delta E = PC \times Cos\theta \tag{3.6}$$

for each of the proportional counters and their summation. This computed correction largely eliminates the angle dependence of the event pulse amplitude for particles going through the proportional counters.

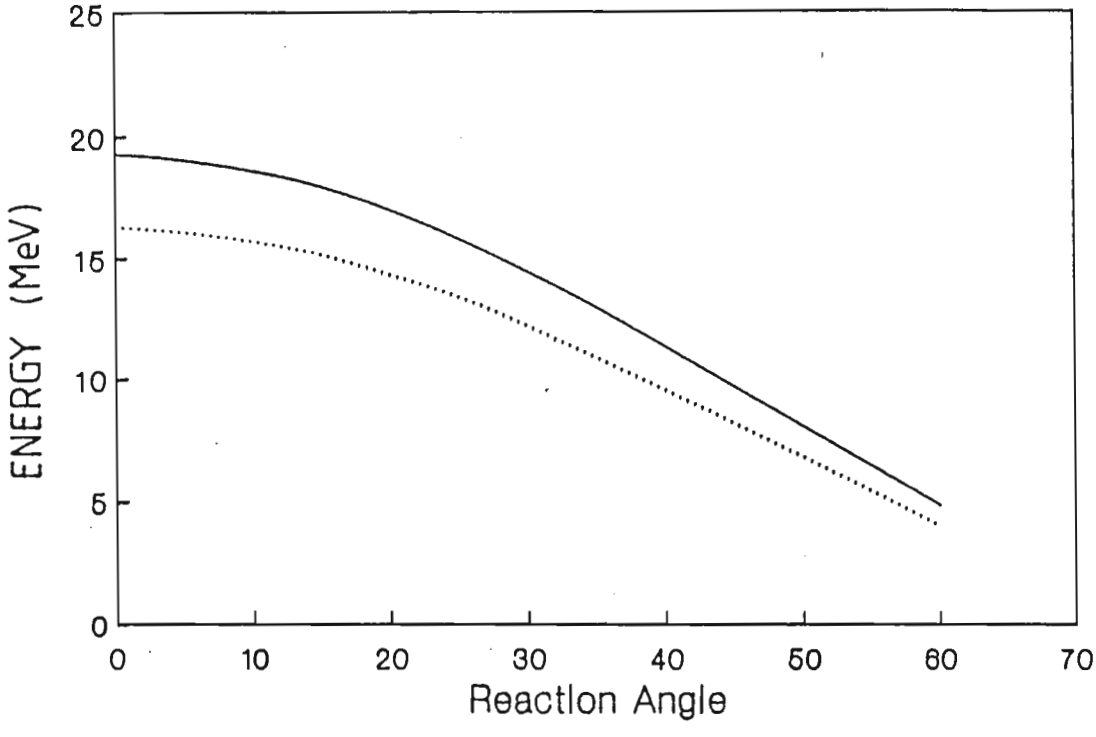

Figure 3.17: Kinematic curve for deuteron distributions with 22 and 18 MeV neutrons

3.3 Data acquisition

3.3.1 Monitor spectra and scalers

Run-time data is accumulated in multi-parameter mode in the PDP-11 digital data acquisition system known as SUREAL[6]. Spectra are obtained for seven parameters viz. A, B, A+B, PC1, PC2, PC3 and TAC, with the first six being used for gated multi-parameter acquisition.

The single spectra settings and multi-parameter SUREAL settings are available on video display. The multi-parameter configuration can be altered with a light pen. Polaroid photographs of single spectra and two parameter spectra are taken to the record performance of the detectors so that the detector setup can be replicated in subsequent runs on the accelerator.

Four two-parameter spectra are set to correspond to:

i) A vs B

ii) PC1 vs A+B

iii) PC2 vs A+B

iv) PC3 vs A+B

Spectrum (i) is used to monitor the symmetry of the gains for A and B at the photomultipliers while (ii) and (iii) give the ΔE-E curves that are used for particle identification. Proton loci are set on the ΔE-E curves by using the scattered protons from a thick perspex sample. Deuteron loci are set using a thick deuterated radiator. Proton and deuteron loci are marked on the video screen and used as reference for checking the loci of the emanating charged particles. Spectrum (iv) is used to set the gains and discriminator levels on PC3 and to monitor it's efficiency as a veto detector. When used as a veto counter, PC3, in anti-coincidence with A+B should not show any distribution in spectrum (iv). Indeed, this is what we observe.

Seven scalars are used as monitors during a run. Scalar data is recorded in a log book and the long term consistency or deviance of the system is inferred from the scalar readings. Gain drifts and/or fluctuations are also checked and corrected once daily by observing the single spectra obtained with the ^{207}Bi and Am-Mo sources. Scalar readings for scattered protons and deuterons from perspex and deuterated perspex radiators for 100μC of beam onto the tritium gas target are also used as checks between runs. Besides indicating the consistency of the detectors the p- and d-radiators also show the state of the p- and d-loci. A typical ΔE-E plot for a zirconium target is shown in Fig. 3.18, and for a perspex radiator in Fig. 3.19.

The events at the lower left corner of the diagram in Fig 3.19 are random events that have generated gate signals. Such events are concentrated just above the bias levels where the individual detector count rates are highest.

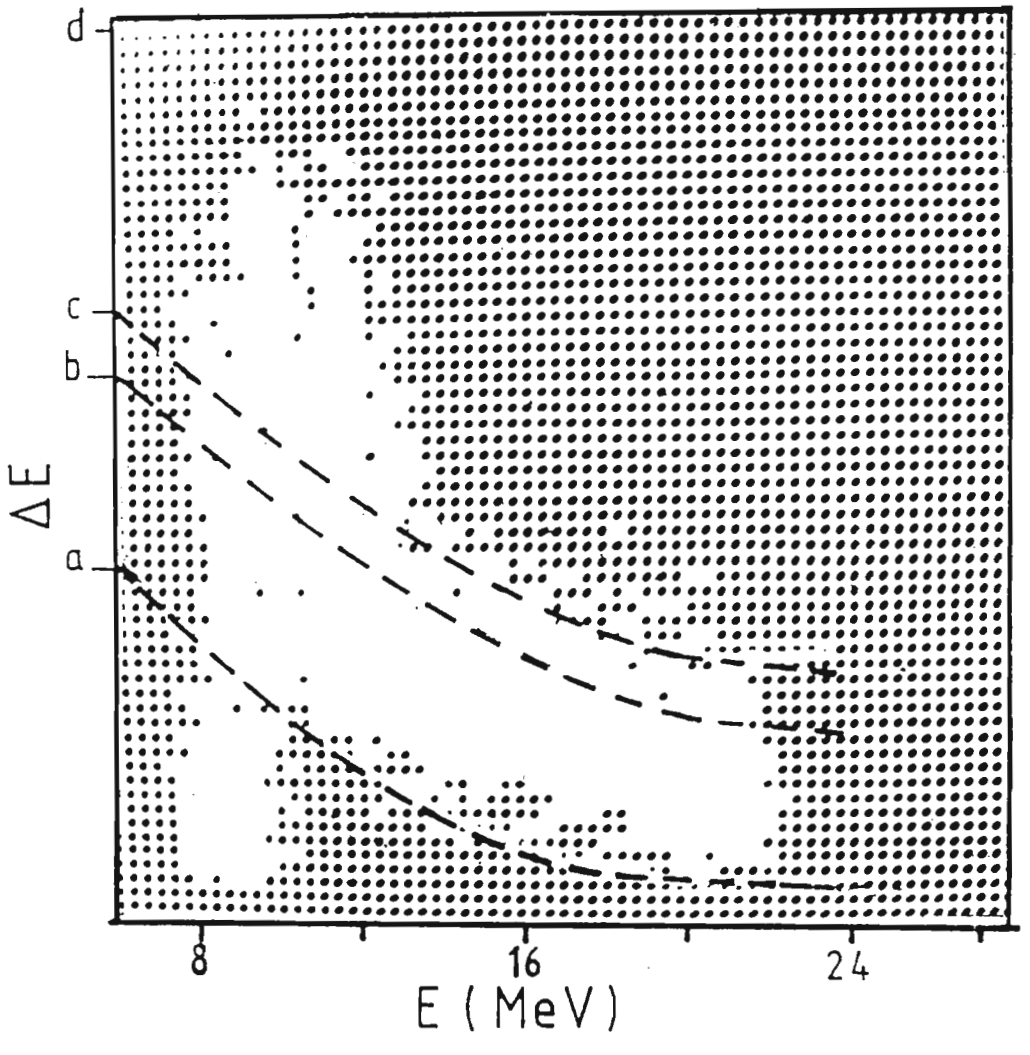

Figure 3.18: ΔE vs E plot showing loci for protons (a-c) and for deuterons (b-d). This plot, obtained with a zirconium sample, shows two strong deuteron peaks (upper left) and also a random peak (lower left) which is rejected in the data analysis[3].

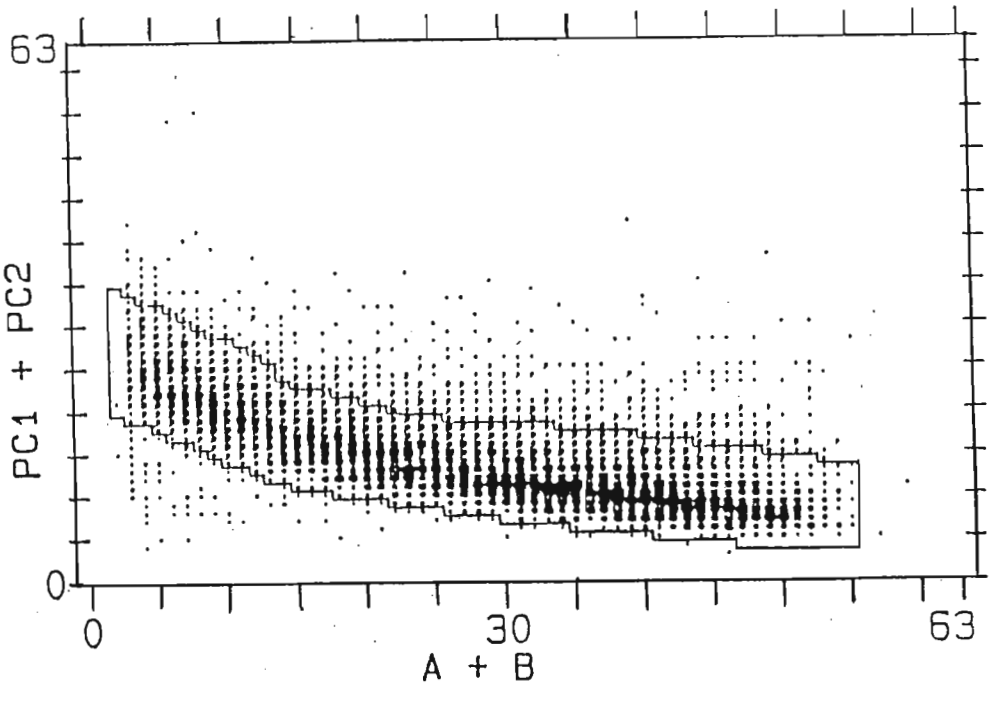

Figure 3.19: PC1 + PC2 *vs* (A+B) plot showing loci for protons, obtained with a perspex radiator

For the purpose of energy calibration polythene (p-poly) and deuterated polythene (d-poly) samples are used in place of the sample at neutron energies of $\sim$ 22 MeV and $\sim$ 18 MeV. The energy calibrated system can then be used to determine the energies of reaction peaks in the residual nuclei. p-poly or d-poly spectra are also used to normalize the target yields to cross-sections, using the well known cross-section for elastic n-p[7] scattering.

3.3.2 Neutron flux monitors

Neutron beam profile control is important in the experimental procedure and the beam has to be maintained at an adequate cross sectional thickness. If the beam has too large a cross section then it hits the collimators and results in additional neutron background from the collimators. A beam of

too small a cross section, on the other hand, is likely to burn a hole through the 0.0025mm Havar window on the tritium gas cell. The neutron beam is monitored by observing the profile of the incoming deuteron beam on the accelerator control module and adjustments to the size and shape can be made by adjusting the quadrupole magnets on the beam line.

The neutron flux from the d-T reaction in the tritium cell was monitored in three ways, each of which has disadvantages.
i) The integrated deuteron beam current(microCoulombs) directed into a tritium cell at constant pressure($\sim$ 0.8 atmospheres) should give a reliable relative monitor of total integrated neutron flux through the sample.
ii) A largely energy independent detector referred to as a "Long Counter"[8][9] is placed at 90^0 to the beam direction and in line with the tritium target. This detector is also sensitive to low energy neutrons coming from the d-d and other reactions in beam-line collimators. The Long counter response is thus also a function of the beam focus and direction. A poor focus or misdirected beam will therefore increase the count rate in the long counter for a given beam current into the target cell.
iii) A high bias on the particle spectrometer scintillator should eliminate contributions from low energy neutrons and a scalar on the output of a discriminator set with a sufficiently high bias should be a good monitor of high energy neutrons incident on the scintillator.

3.4 Data reduction

Gated data from the ADC's is accumulated in multi-parameter mode in the SUREAL data acquisition system in the control room of the Van de Graaff accelerator facility.

For every gated event, six parameters were stored on magnetic tape with the PDP-11 based digital acquisition system.

Magtape data is analysed off-line with the use of an event sorting and analysis program in the X-SYSTEM (XSYS), which is used to read the SUREAL tapes. The multiparameter sorting program NPART1 in XSYS was made available by Mr. John Pilcher of the National Accelerator Centre at Faure.

3.4.1 Particle identification.

Particle identification is based on the standard ΔE-E system. On a ΔE vs E plot, protons, deuterons and alphas, etc. lie on different curves. Proton and deuteron particle identification is brought about by setting particle loci for protons and deuterons with the use of a perspex or a deuterated radiator respectively. The perspex radiator will only emit protons whereas the deuterated radiator emits both deuterons and protons. In the current setup the Landau distributions for protons and deuterons from the deuterated radiator are seen to overlap. Observed distributions for protons and deuterons are shown in Fig. 3.20

The upper locus of the deuterons, at the different energy slices, is set above the upper tail of the d- distribution (see Fig. 3.20). The lower locus is set at the point of intersection of the proton and deuteron spectra. Thus,

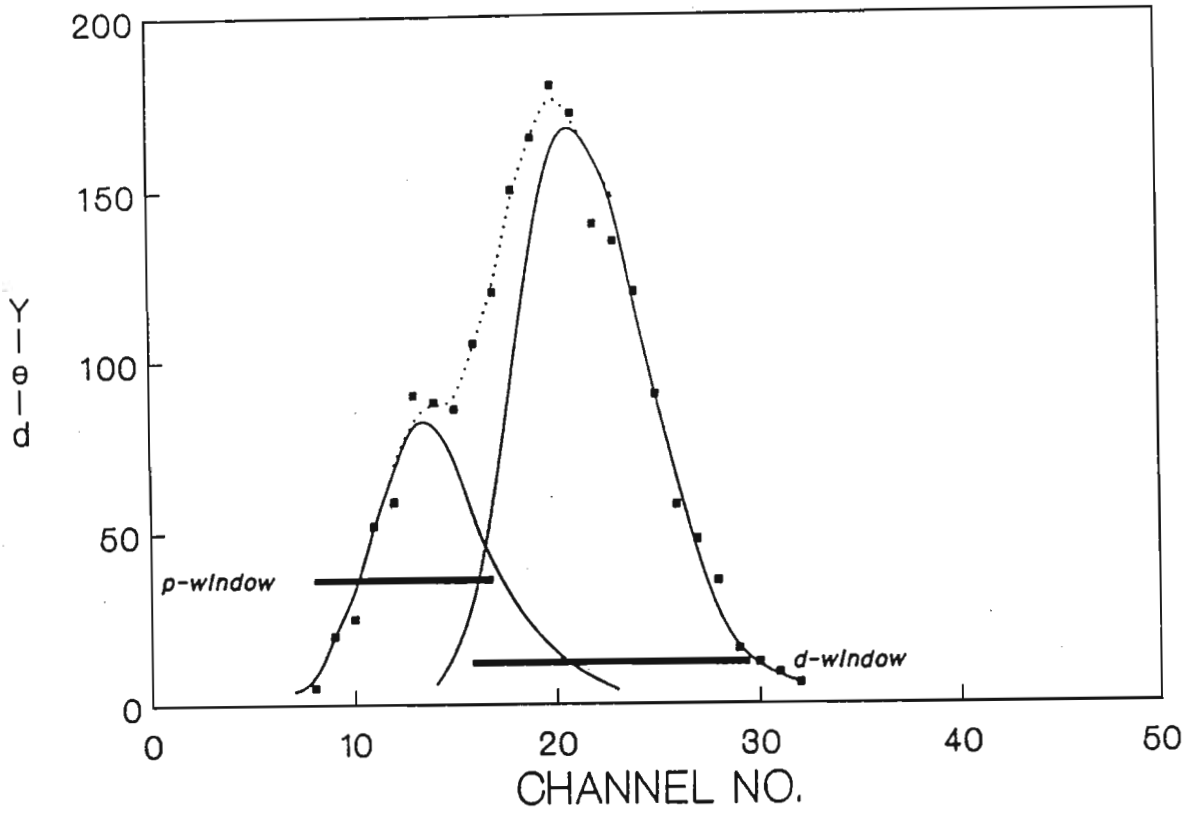

Figure 3.20: Landau distribution for protons and deuterons

while one loses less than 10% of the deuterons at the lower end, one is also eliminating more than 80% of the protons. The d-loci are generally set independently for PC1, PC2 and their sum (PC1+PC2)/2, although they tend to be identical. These d-loci are used to particle gate the target sample spectra and thus extract the d- distribution for the (n,d) reaction

3.4.2 Backgrounds

The spectrometer eliminates the background in many different ways. The main part of the background is eliminated by the three counter coincidence conditions. Nevertheless there will be some background, due to random coincidence events and due to charged particles traversing two proportional counters but not originating in the target. The anti-coincidence counter

PC3 eliminates all those charged particles emanating from behind the target. The efficiency of PC3 as a veto counter was checked on the ΔE-E monitor display and found to be very good. The time relations between the proportional counters and the scintillator also serves to eliminate some of the background by imposing conditions similar to a time-of-flight restriction.

The two-dimensional ΔE-E analysis reduces the background as the background events seldom satisfy the triple conditions for identification. These random coincident events generally consist of small E and ΔE pulses and are clustered in the lower corner of the ΔE-E plots, as seen in Fig. 3.19.

The remainder of the background can be considered in two ways:
i)The background obtained with a sample-out run (eg. from the PC gas filling).
ii)The background due to protons from the ^{27}Al(n,p)^{27}Mg and ^{56}Fe(n,p)^{56}Mn reactions.

The former is easier to observe and readily removed whereas the exact contribution of protons from the (n,p) reaction is not that easily discerned. For the sample-out background the target is replaced by a set of thin wires that provides a nearly weightless sample. The background run is normalized to the target run by equating the respective current integrator values and the normalized background is then subtracted from the target spectra. The background spectra and target spectra must correspond exactly in angle and particle gates. The background (Fig. 3.21) shows a d-peak that appears to come from the ^{16}O(n,d)^{15}N(gnd) and ^{40}Ar(n,d)^{39}K(gnd) reactions arising from the CO_2-Ar mixture in PC2. This background is less than 5% of the yield of the target. The background with sample-out follows the trend of the target spectra with the number of events falling off with increasing angle.

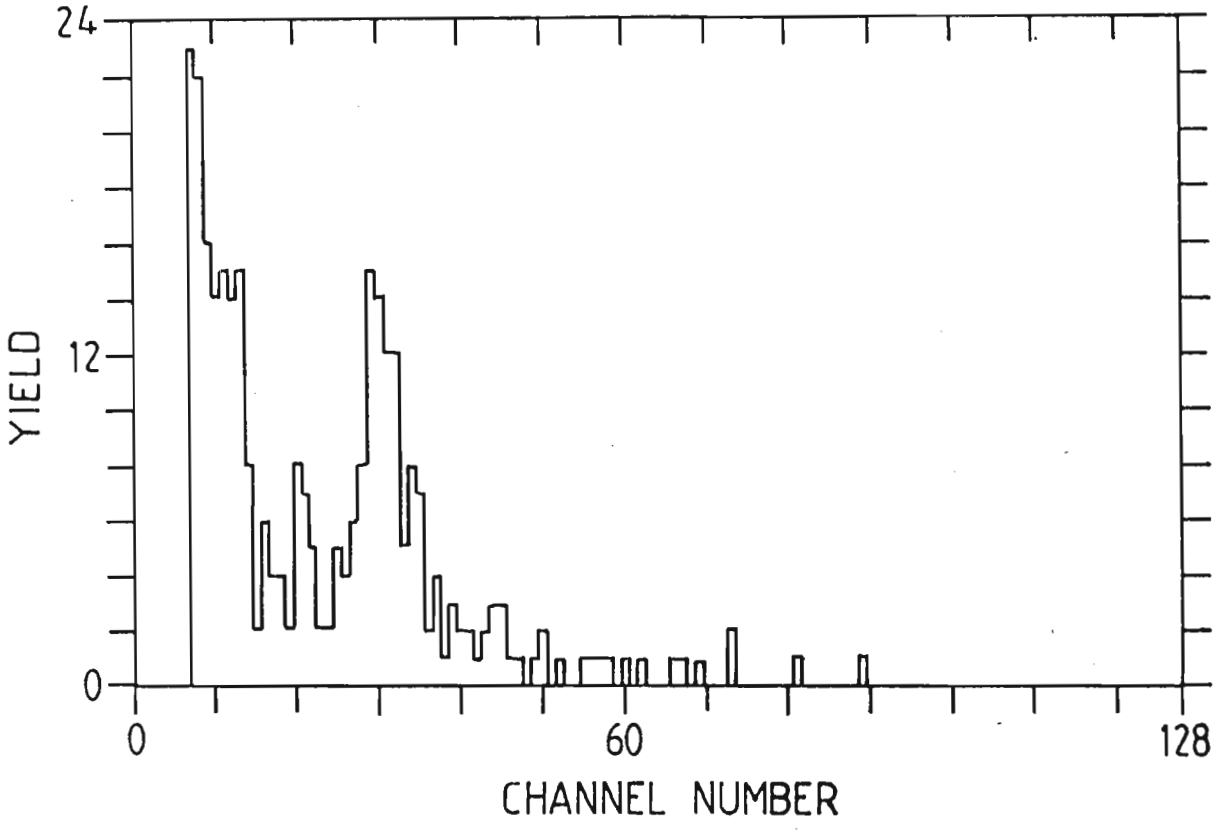

Figure 3.21: A sample target-out background spectrum

Not all the background due to the (n,p) reaction can be removed due to the overlap of p- and d-loci, implying that the final energy spectra will have an underlying proton spectrum. Background due to the (n,p) reaction will be mostly the tail of the p-distribution, with the largest number of events at low energy. The proton background for any specific angle is a smooth curve that drops off rapidly with increasing channel (viz. energy). The background removed is usually assessed as a ratio of the total yield and is based on the proton distribution. The final energy spectra are normalized to experimental cross-sections which are compared with theoretical cross-sections.

References

1.) W.R. McMurray and K. Bharuth-Ram, S.Afr. J. Phys. 8 (1985) 22.
2.) A.C. Bawa, M.Sc. Thesis, University of Durban-Westville, 1986.
3.) W.R. McMurray, K. Bharuth-Ram and S.M. Perez, Z. Phys. A315 (1984) 189.
4.) G.F. Knoll, Radiation detection and measurement (John Wiley and Sons, New York, 1979).
5.) A. Smith and M.J.L Turimer, Nucl. Instr. and Meth. 192 (1982) 475.
6.) J.V. Pilcher, M.Sc. Thesis, University of Cape Town, 1979.
7.) L.N. Rothenberg, Phys. Rev. C1 (1970) 1226.
8.) A.O. Hansen and M.C. McKibben, Phys. Rev. 72 (1947) 673.
9.) L.V. East and R.B. Walton, Nucl. Instr. and Meth. 72 (1969) 161.

Chapter 4

Results

4.1 ^{27}Al(n,d)^{26}Mg

A particle spectrum for the ^{27}Al(n,d)^{26}Mg reaction is shown in Fig. 4.1. The peaks shown correspond to the states of ^{26}Mg at excitations of 0.0, 1.81, 2.93 and 4.3 MeV. Several other smaller peaks are visible but these are either unresolved or have a yield that is too small for a spectroscopic calculation. A background of 5-10% of the peak area is still present in the spectrum.

Deuteron spectra have been obtained at various reaction angles in order to extract the angular distributions and the cross-sections for the different level transitions. Deuteron spectra for the various reaction angles are shown in Fig. 4.2.

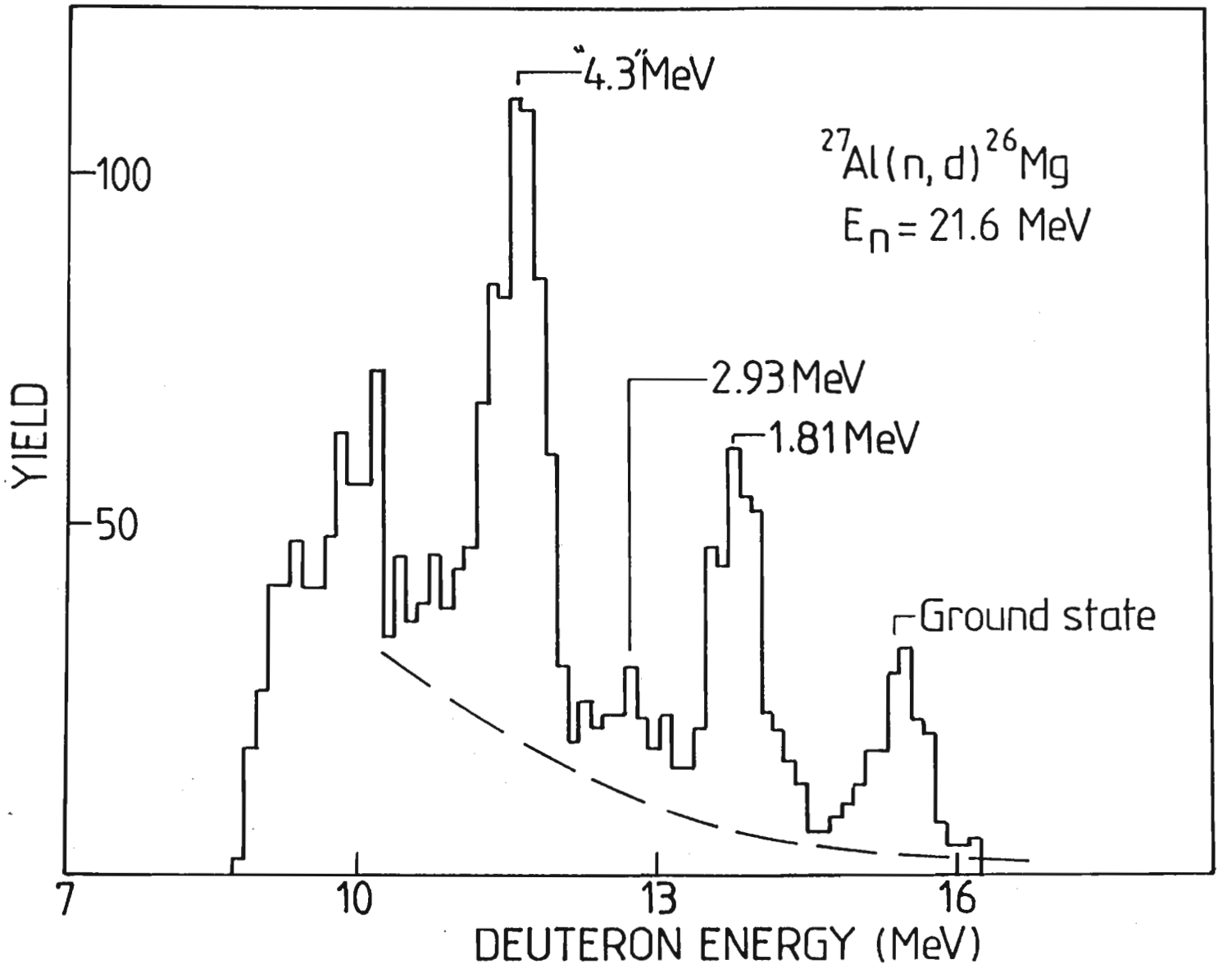

Figure 4.1: Summed deuteron spectrum up to 15^0 for the ^{27}Al(n,d)^{26}Mg reaction

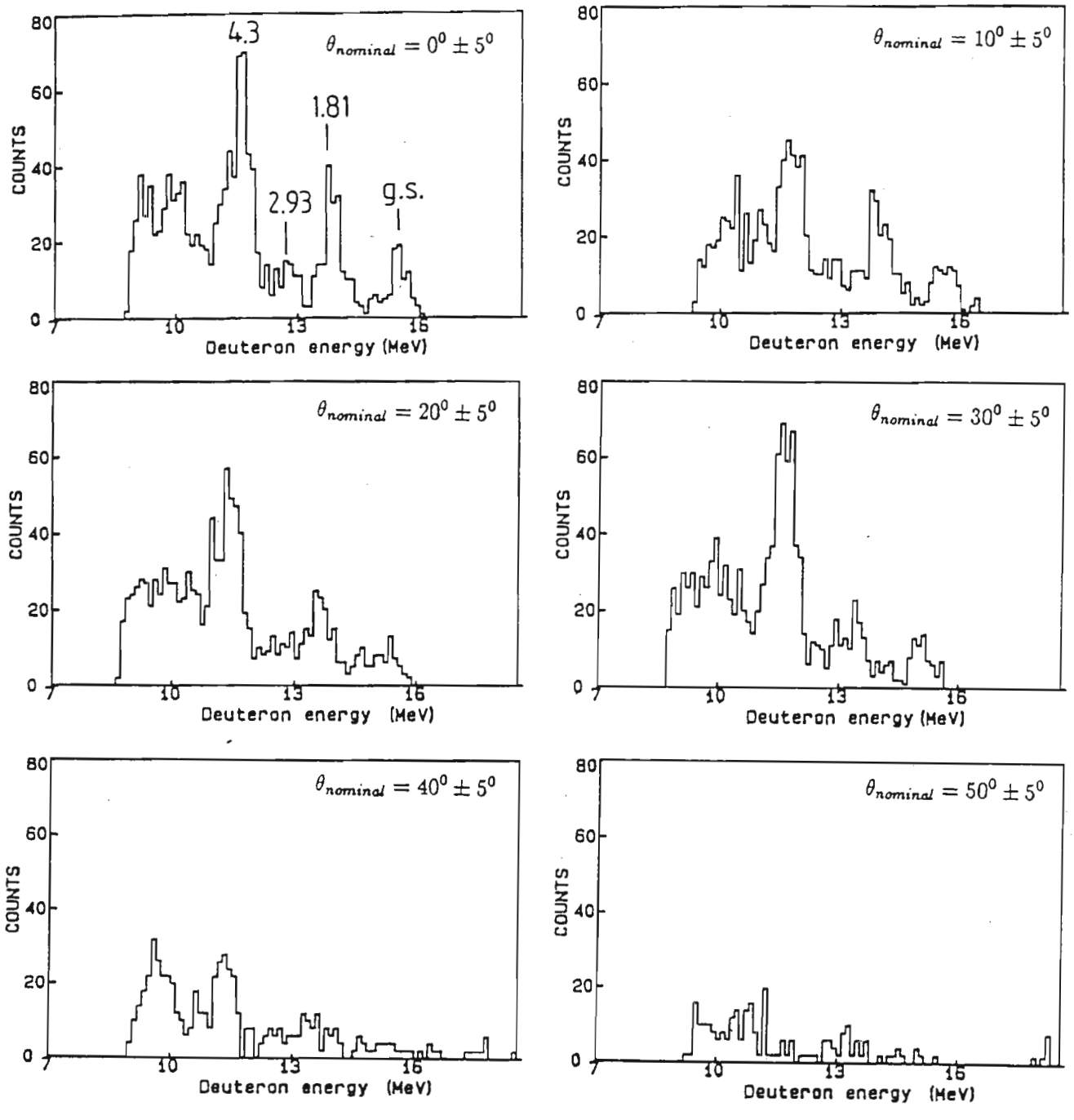

Figure 4.2: Deuteron spectra for the ^{27}Al(n,d)^{26}Mg reaction at various reaction angles

4.2 ^{56}Fe(n,d)^{55}Mn

The particle spectra from the ^{56}Fe(n,d)^{55}Mn reaction at 21.6 MeV are shown in Fig. 4.3. Peaks corresponding to ^{55}Mn level energies of 0.00 MeV, 1.6 MeV and 2.3 MeV have been analysed for a spectroscopic calculation. A sample-out background has been subtracted from the raw data to give Fig. 4.3. A proton spectrum from the ^{56}Fe(n,p)^{56}Mn reaction has also been removed. Deuteron spectra at the different reaction angles are shown in Fig. 4.4.

4.3 The experimental cross-section

The experimental cross-section per region of solid angle is found by normalizing the yield (number of events) for that solid angle with a known cross-section such as that for scattering of protons from a polythene sample (p-poly) or for scattering of deuterons from a deuterated polythene sample (d-poly).

The yield for a specific energy level at at some mean angle is found by integrating over that portion of the area that contributes to that level. The yield is dependent on the solid angle, the neutron flux, the number of sample nuclei and the particle detection efficiency. The yield is given by

$$Y = \left(\frac{d\sigma}{d\Omega}\right)_\theta \times \Delta\Omega \times F \times N_s \times \epsilon_{particle} \qquad (4.1)$$

where,

$\left(\frac{d\sigma}{d\Omega}\right)_\theta$ is the laboratory cross-section,

$\Delta\Omega$ is the solid angle region,

F is the neutron flux = constant $\times$ neutron monitor count(M),

N_s is the number of sample nuclei,

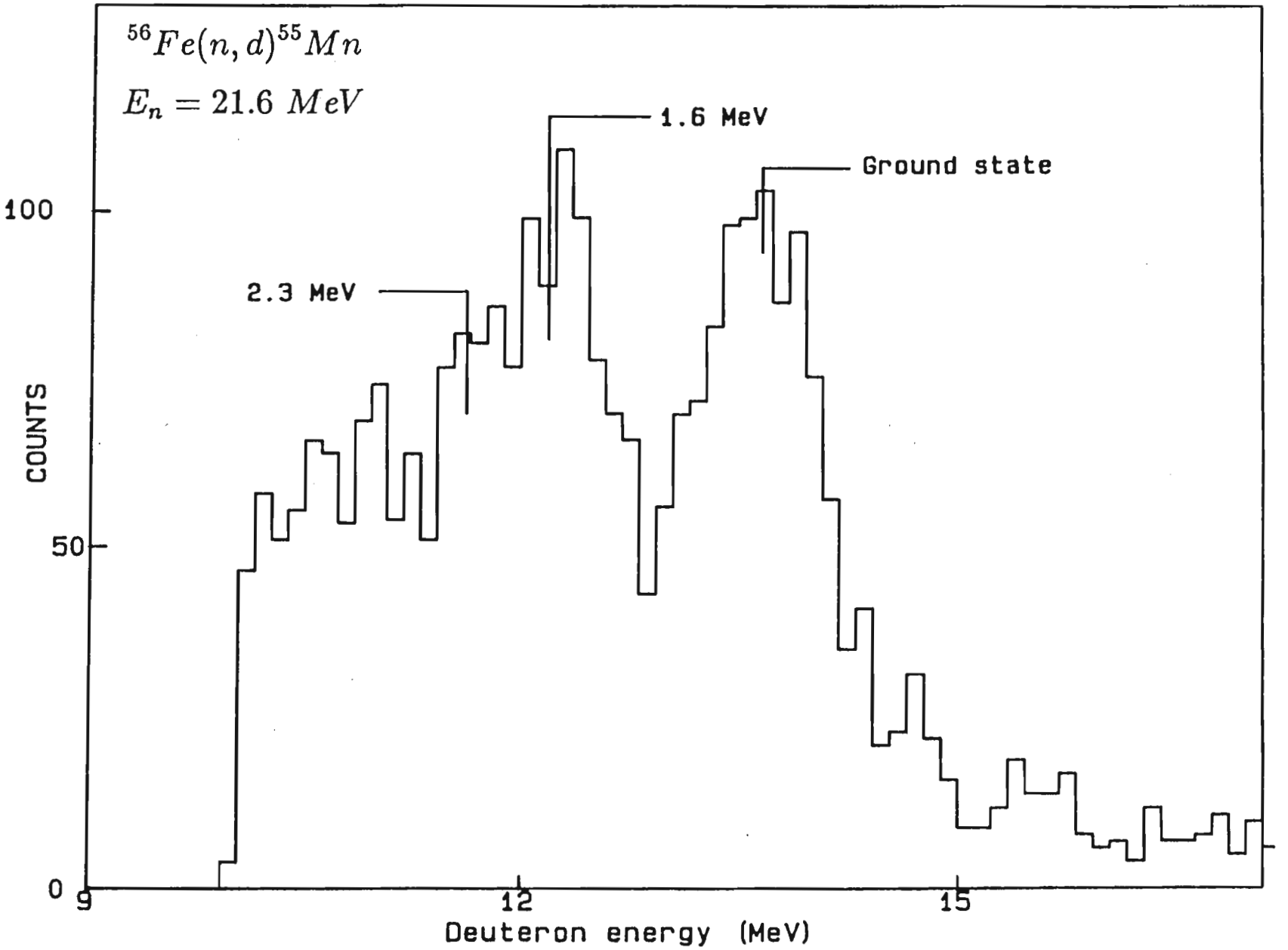

Figure 4.3: Summed deuteron spectrum up to 15^0 for the ^{56}Fe(n,d)^{55}Mn reaction

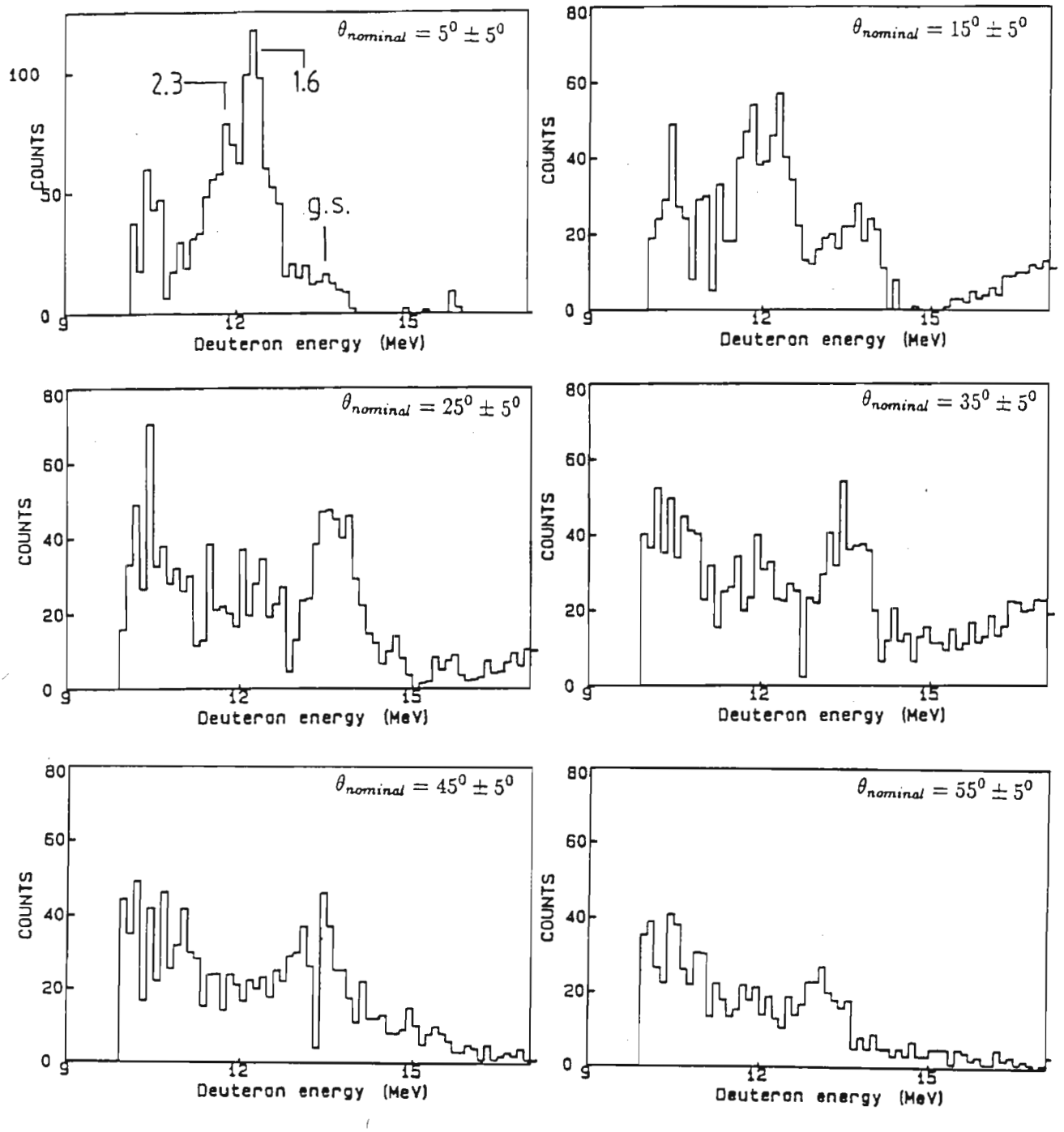

Figure 4.4: Deuteron spectra for the ^{56}Fe(n,d)^{55}Mn reaction at various reaction angles

ϵ_p is the particle detection efficiency and
Y is the yield per $\Delta\Omega$.

The yield from a proton-rich sample can be represented as

$$Y_H = d\sigma_H \times \Delta\Omega \times k \times M_H \times N_H \times \epsilon_p \tag{4.2}$$

The subscript H in the above equation indicates hydrogen and represents the proton-rich sample. Similarly for the (n,d) reaction on the target we can represent the yield as

$$Y_{(n,d)} = d\sigma_{(n,d)} \times \Delta\Omega \times k \times M_{(n,d)} \times N_{target} \times \epsilon_p \tag{4.3}$$

Dividing the latter equation by the former we get

$$d\sigma_{(n,d)} = d\sigma_H \times \frac{Y_{(n,d)}}{Y_H} \times \frac{M_H}{M_{(n,d)}} \times \frac{N_H}{N_{target}} \tag{4.4}$$

The yields for the (n,d) reaction and the proton scattering are measured as previously mentioned. The monitor counts are taken from the current integrator for the respective samples. The number of particles in the samples are calculated according to the density and dimensions of the sample. For example, in a p-poly sample $(CH_2)_n$, 1cm wide with a density of 14mg/cm^2 the number of protons is

$$\begin{aligned} N_H &= 6 \times 10^{23} \left(\frac{2}{14}\right) \times 0.014 \\ &= 1.2 \times 10^{21} atoms/cm^3 \end{aligned} \tag{4.5}$$

For both ^{27}Al and ^{56}Fe we had ~100% chemically pure foils with two sheets each, 1cm wide and of densities 14mg/cm^2 and 16mg/cm^2 respectively. Then the number of particles is

$$\begin{aligned} N_{Al} &= 6 \times 10^{23} \left(\frac{1}{27}\right) \times 2 \times 0.014 \\ &= 6.2 \times 10^{20} atoms/cm^3 \end{aligned} \tag{4.6}$$

E_x(MeV)	6^0	11.7^0	21.1^0	30.6^0	40.3^0	50.3^0
0.00	0.62(6)	0.54(5)	0.58(6)	0.37(4)	0.11(2)	0.09(2)
1.81	1.1(1)	1.1(1)	1.3(1)	1.0(1)	0.36(5)	0.28(4)
2.93	0.35(4)	0.22(2)	0.22(2)	0.19(2)	0.09(2)	0.06(2)
4.3	3.7(4)	2.8(3)	1.9(2)	1.7(2)	0.9(2)	0.43(7)

Table 4.1: Experimental cross sections (mb/sr) for the ^{27}Al(n,d)^{26}Mg reaction,including experimental uncertainties but excluding normalisation uncertainties

E_x(MeV)	7.5^0	15.9^0	25.5^0	35.4^0	45.3^0	54.6^0
0.00	2.0(2)	4.9(5)	9.0(9)	8.0(8)	3.4(4)	2.1(3)
1.6	1.2(1)	1.6(2)	1.2(1)	1.0(1)	0.52(7)	0.38(6)
2.3	1.5(1)	1.5(2)	0.95(9)	0.80(8)	0.48(6)	0.25(4)

Table 4.2: Experimental cross sections (mb/sr) for the ^{56}Fe(n,d)^{55}Mn reaction including experimental uncertainties but excluding normalisation uncertainties

and for ^{56}Fe,

$$\begin{aligned} N_{Fe} &= 6 \times 10^{23} \left(\frac{1}{56}\right) \times 2 \times 0.016 \\ &= 3.4 \times 10^{20} atoms/cm^3 \end{aligned} \tag{4.7}$$

The quantity $d\sigma_H$ is well documented for (n,p) scattering at different incident energies and is given by

$$d\sigma_{lab} = 4cos(\theta_{lab}) d\sigma_{cm} \tag{4.8}$$

where $d\sigma_{cm}$ is easily obtained from a table of values of $cos\theta$ and $d\sigma_{cm}$. Thus with all else known the experimental cross-section $d\sigma_{(n,d)}$ is easily determined.

4.4 The theoretical cross-section

The theoretical cross-section is generated in the DWBA by optical potentials that simulate the distorted waves mentioned in section 2.1. Optical potentials of a Woods-Saxon and Woods-Saxon derivative form are used to describe the cross-section for the (n,d) transfer reaction. The parameters for the optical potentials are derived from elastic scattering results. For the incident channels specific parameters for elastic scattering from the target nuclei at similar energies to the incident energy were used, but global parameters were used for the exit channel due to the lack of adequate deuteron elastic scattering data for the residual nuclei. Global parameters have the disadvantage of inducing an energy dependence in the potentials and of not representing the individual nuclei adequately. The theoretical cross-section was computed with the DWBA program DWUCK4[1].

DWUCK calculates the scattering differential cross-section for a general form of the DWBA. The incoming and outgoing particles are a combination of spin $\frac{1}{2}$ and spin 1 particles and give the spin dependent parts of the optical potentials for the distorted waves. The calculations were performed in a zero-range form between the coordinates of the incoming and outgoing waves. The (n,d) transfer reaction is compensated for finite range effects with a Local Energy approximation (LEA)[2]. The DWBA code DWUCK computes a transition amplitude for the reaction A(a,b)B of the form

$$T_{DW} = J_{\beta\alpha} \int d\vec{r}_\alpha \int d\vec{r}_\beta \chi_\beta^{(-)*}(k_\beta, r_\beta) \langle \beta \mid W \mid \alpha \rangle \chi_\alpha^{(+)}(k_\alpha, r_\alpha) \qquad (4.9)$$

with the notation being described in section 2.1.

Although there are several optical potentials available[1][3] in DWUCK, only the four listed below were utilised as only these are needed to describe the single particle transfer reaction.

i) Volume Woods-Saxon potential

ii) Surface Woods-Saxon potential

iii) Spin-Orbit potential

iv) Coulomb potential

Each of the above potentials is described in section 2.2. The non-local correction factor given by Kunz[1] for nucleons is 0.85 and for deuterons is 0.54 and is maintained for present calculations. For the finite range correction factor Kunz quotes a value between 0.621 and 0.695 as being appropriate for the (n,d) reaction. A value of 0.690 was used in this study.

The neutron optical potentials for both the ^{27}Al(n,d)^{26}Mg and ^{56}Fe(n,d)^{55}Mn reactions were easier to obtain than the deuteron optical potentials and one had to resort to using global potentials for the exit channel. A non-relativistic set of parameters[4] for a bombarding energy of 12-90 MeV was used for the d-channel. The parameters were obtained from the following definitions:

$$\begin{aligned}
V_R &= 88.5 - 0.26E + 0.88ZA^{1/3}MeV \\
r_R &= 1.17fm \\
a_R &= 0.709 + 0.0017Efm \\
W &= (12.2 + 0.026E)(1 - e^{\beta})MeV,\ \beta = -(E/100)^2 \\
W_D &= (12.2 + 0.026E)e^{\beta}MeV \\
r_w &= r_D = 1.325fm \\
a_w &= a_D = 0.53 + 0.07A^{1/3} - 0.04\Sigma_i exp(-\mu_i) \\
r_c &= 1.30fm \\
V_{so} &= 7.33 - 0.029EMeV \\
r_{so} &= 1.07fm \\
a_{so} &= 0.66fm
\end{aligned} \tag{4.10}$$

	V_0	r_0	a_0	W_o	r_W	a_W	W_D	V_{so}	r_{so}	a_{so}	r_c
n+^{27}Al[5]	45.17	1.18	0.64	3.19	1.26	0.58	7.14	6.0	1.01	0.5	1.3
d+^{26}Mg[4]	87.92	1.17	0.73	.315	1.32	0.80	13.2	6.2	1.07	0.66	1.3
p+^{26}Mg		1.25	0.70								
n+^{56}Fe[6]	49.90	1.17	0.61	1.51	1.31	0.60	6.02	5.8	0.89	0.41	1.3
d+^{55}Mn[4]	90.70	1.17	0.73	0.22	1.32	0.79	12.32	6.94	1.07	0.60	1.3
p+^{55}Mn		1.25	0.70								

Table 4.3: Optical potential parameters for the ^{27}Al(n,d)^{26}Mg and ^{56}Fe(n,d)^{55}Mn reactions

the symbol μ_i is defined by

$$\mu_i = \left[\frac{M_i - N}{2}\right]^2 \tag{4.11}$$

and the M_i are the magic numbers 8, 20, 28, 50, 82 and 126 and N is the neutron number.

The optical potentials for the transition to the ground state of ^{26}Mg and ^{55}Mn are shown in Table 4.3. The value of E in the parameter definition is the energy of the outgoing deuterons i.e. it is the incident energy of the neutron less the Q value of the reaction for a specific energy level. Thus the value of E for different energy levels is adjusted according to the Q value of the ground state and the excitation energy of the level.

The bound proton in the target nucleus has a real potential and a spin-orbit potential. The binding energy of the nucleon in the ground state to the 'core' is entered into the program and an iteration is performed on the potential well depth until the fixed binding energy is reproduced. The binding energy of the excited states is adjusted accordingly as:

$$\mid B_n \mid_{ex} = \mid B_n(g.s.) \mid + Ex \tag{4.12}$$

$\mid B_n(g.s.) \mid$ is the binding energy of the proton in the ground state in the target nucleus and Ex is the energy of the excited state(s) in the residual

nucleus.

The effects of varying the parameters of the optical potentials has been widely investigated[7][8]. In our determination of spectroscopic factors it was necessary to search for the best fit by iterating the parameters, usually r, V, a and W. The ambiguities arising from varying more than one parameter at a time are also well known[9]. We have minimized the effect of parametrizing the optical potentials by demanding small changes in the potential parameters.

The cross-section for the (n,d) reaction on the respective targets obtained from DWUCK is then compared with the experimental cross-section to reveal the spectroscopic factors. The experimental angular distributions obtained with the present experimental apparatus are to some extent smoothed by the angular resolution functions. The angle spread on any one differential cross-section measurement is $\sim 5^0$ FWHM. This angular spread can be folded into the theoretical angular distributions to give theoretical curves which can be directly compared with experiment, thus eliminating angle based errors in the calculation of spectroscopic factors.

4.5 Spectroscopic factors

The spectroscopic factors for a specific level are computed from a comparison of the experimental and theoretical cross-sections, taking into account the finite range effects. The spectroscopic factor factor C^2S is calculated from

$$\sigma_{exp} = \frac{3}{2} D_0^2 C^2 S \sigma_{DW} \tag{4.13}$$

σ_{DW} is the theoretical distorted waves cross-section calculated with neutrons in the incident channel and deuterons in the exit channel. The value of the finite range parameter $D_o{}^2$ was taken as 1.55 from Bassel[10] and includes the effects of d-state admixture in the deuteron wavefunction. The spectroscopic factor C^2S includes the isospin Clebsch-Gordan coefficient

$$C = \left\langle T_f T_{fz} \frac{1}{2} t_z \mid T_i T_{iz} \right\rangle \tag{4.14}$$

with T_f and T_i the isospins of the residual and target nuclei respectively. The factor $\frac{3}{2}$ takes into account the spins of the incoming and outgoing particles and is often combined with $D_o{}^2$ to form a normalization factor, N.

$$N = \frac{3}{2} D_0^2 = 2.325 \tag{4.15}$$

The normalisation factor is particularly interesting if one compares pickup via (n,d) and (d,^{3}He) reactions. As a result of the relatively complex nature of incoming and outgoing particles in (d,^{3}He), the normalisation factors used range from 2.0 to 2.95[11][12][13]. The variation in the normalisation factor alone can thus induce uncertainties of up to 30% in the spectroscopic factors, excluding any experimental uncertainties. This variation arises directly from the factor $D_o{}^2$, which is generally better understood for the (n,d) reaction than the (d,^{3}He) reaction. It is expected that the variation in the normalisation factor for the (n,d) reaction is not more than 10%.

The spectroscopic factor is then

$$C^2S = \frac{\sigma_{exp}}{N\sigma_{DW}} \tag{4.16}$$

Best fits to the experimental cross-section were found by minimizing the expression

$$\chi^2 = \frac{1}{n}\Sigma_{i=1}^{n}\left[\frac{\sigma_{exp}(\theta_i) - C^2S \times N\sigma_{DW}(\theta_i)}{\Delta\sigma_{exp}(\theta_i)}\right]^2 \tag{4.17}$$

n is the number of experimental points, θ_i the angle at each of these points and $\Delta\sigma_{exp}(\theta_i)$ is the error associated with $\sigma_{exp}(\theta_i)$. The best fit parameters were found by varying the optical parameters in $\sigma_{DW}(\theta)$ without attempting a parametrization.

4.5.1 Errors and uncertainties

The overall uncertainty in the spectroscopic factors is estimated to be $\sim$ 30% and is a combination of errors and uncertainties from the experimental cross-section, the normalization factor and the DWBA.

An error of the order of 10% is induced in determining the contributions to the particle yield, the integrated neutron flux monitor count, and the number of atoms in the sample. A further 10% uncertainty is expected in normalising the results with the (n,p) cross-section, giving a combined error of 15% for the experimental cross-section.

The error in the normalisation factor N is expected to be $\sim$ 10% due to possible variations in the value of D_o^2. This puts the value of D_o^2 within the range 2.1 to 2.5, well within the expected values for the (n,d) reaction.

The error in the DWBA formalism is set at 25% and stems from several sources:

i) The non-locality of the optical potential

ii) Energy dependence in the optical potentials
iii) A probable j-dependence in the cross-section
iv) The use of global potentials for the deuteron channel
v) The approximation made for the N-N interaction i.e. simplifying it to a first order perturbation and truncating the calculation after a fixed number of iterations.
vi) The intrinsic error induced by the macroscopic calculation that simulates the distorted waves with optical potentials.

The value of 25% is set empirically as this is the maximum possible variation in the theoretical cross section that enables reproduction of a realistic potential well depth for the bound particle.

The overall error in magnitude of 30% is then a combination of the 15, 10 and 25% error.

4.6 Analysis of ^{27}Al(n,d)^{26}Mg

4.6.1 Transition to the ground state

The ground state transition from ^{27}Al to ^{26}Mg must satisfy angular momentum selection rules. Since $J^\pi = \frac{5}{2}^+$ for the ^{27}Al ground state and $J^\pi = 0^+$ for the ^{26}Mg ground state, parity conservation ensures that we must have the total angular momentum j with a value of $\frac{5}{2}$ and the orbital angular momentum l must be even. Thus for $j = \frac{5}{2}$ only $l = 2$ is allowed for the orbital angular momentum. The $l = 2$ fit to the experimental data is shown in Fig. 4.5. A 15% rms uncertainty is shown for the experimental data. The spectroscopic factor for transition to the ground state was found to be 0.29.

4.6.2 Transition to the 1.81 MeV level

Angular momentum selection rules restrict the transition of $J^\pi = \frac{5}{2}^+ \rightarrow J^\pi = 2^+(1.81$ MeV), with even parity, to an orbital angular value of $l = 2$ or $l = 0$. The angular distribution of the deuterons correlated with the distorted waves analysis shows that the transition is predominantly $l = 2$ with the $l = 0$ contribution being less than 0.5%. The $l = 2$ distribution together with the experimental data are shown in Fig. 4.5. A value of 0.88 for the spectroscopic factor was extracted for the transition to this level.

4.6.3 Transition to the 2.93 MeV level

The 2.93 MeV level is not adequately investigated in previous (n,d) studies[14][15], and even in the high energy study by Brady[14], this level was not sufficiently excited for a spectroscopic calculation; hence no spectroscopic fac-

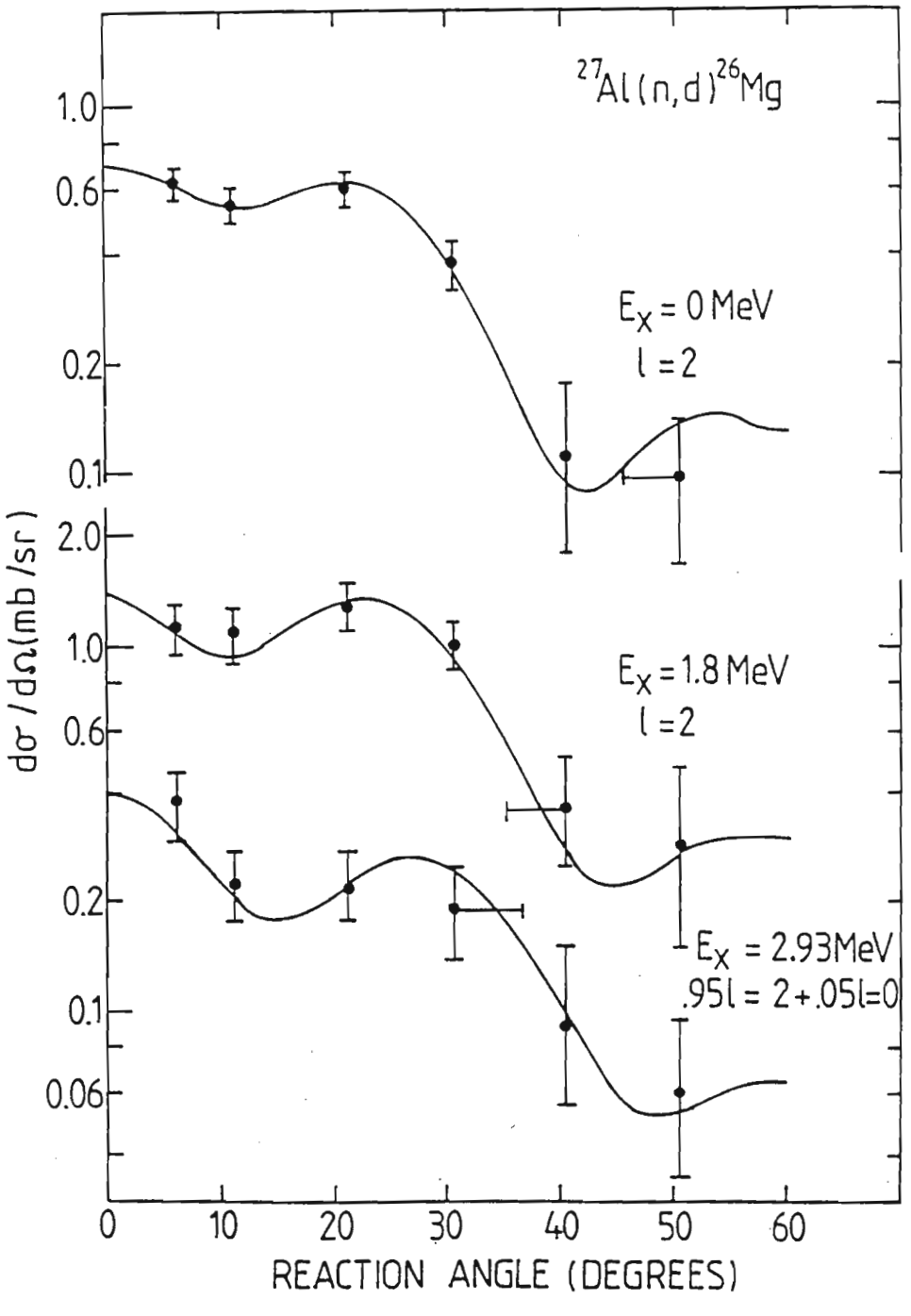

Figure 4.5: Angular distributions for the transitions to the 0.00 MeV, 1.81 MeV and 2.93 MeV levels

tor is quoted for this level in that study. Transition from the ground state of ^{27}Al to the 2nd 2^+ level in ^{26}Mg is restricted to $l = 2$ and $l = 0$ for the orbital angular momentum values. It was found that this transition corresponds to a combination of the $l = 2$ and $l = 0$ transitions (Fig. 4.5). A modified chi-squared program was used to minimize the deviation between the mixed configuration

$$\Omega(2.93) = \alpha(\Phi_{l=2}) - \beta(\Phi_{l=0}) \tag{4.18}$$

$$\alpha^2 + \beta^2 = 1$$

and the experimental values; the ϕ_l represent the unmixed or "pure" configurations and α and β are the weighting factors, the squares of which reflect the percentage of each pure configuration contained in the mixed configuration.

The least squares fitting procedure gives a value of 0.24 for the spectroscopic factor with $\alpha^2 = 0.95$ and $\beta^2 = 0.05$, implying a 95% $l = 2$ transfer and a 5% $l = 0$ transfer. Exclusion of the $l = 0$ contribution leads to a deterioration of the fit with the experimental data. The mixed l value fit to the experimental values are shown in Fig. 4.5. It was attempted to ascertain if an admixture of the $d_{5/2}$ and the $d_{3/2}$ levels in ^{27}Al leads to an improvement of the fit. However, it was found that the 2.93 level l fit is predominantly due to transfer from the $d_{5/2}$ level of ^{27}Al.

4.6.4 Transition to the 4.3 MeV state

The unresolved triplet peak at 4.3 MeV was the most difficult to analyse conclusively in this study. The $J^\pi = 2^+, 3^+, 4^+$ combination at 4.33, 4.35 and 4.32 MeV respectively remain unresolved due to the limited energy resolution of the spectrometer. The mixing of the two allowed transitions to these levels is integrated into the experimental angular distribution for the

peak at "4.3" MeV. The mixing of two or more possible transitions generally leads to greater uncertainties in the determination of the spectroscopic factors. The allowed orbital angular momentum values of $l = 2$ and $l = 0$ are combined to provide the angular distribution of the 4.3 MeV level. The best fit was found using the modified chi-squared program for the $l = 2 + l = 0$ admixture, as mentioned previously. For the best fit it was found that the $l = 2$ transition contributes $\simeq 65\%$ of the distribution while $\simeq 35\%$ is due to the $l = 0$ contribution (Fig. 4.6). The large $l = 0$ contribution may be attributed to $l = 0$ contributions from both the 2^+ and the 4^+ levels. The large strength of the 4.3 MeV level transition is due to angular momentum coupling and the location of nearby states that are submerged within the "4.3" MeV peak. In particular the 3.6 MeV 0^+ state and the triplet $2^+ 3^+ 0^+$ state at "4.8" MeV lie within the limit of resolution of the 4.3 MeV peak for the spectrometer setup used. An energy resolution of $\leq$ (30 keV) is required if we wish to individually analyse the levels in the 4.3 MeV peak. As this was not possible in the present study the 4.3 MeV peak was treated as a single level. The DWBA fit consists of mixed $l = 0$ and $l = 2$ contributions. A spectroscopic factor of 1.9 was extracted for the transition to the "4.3 MeV" state.

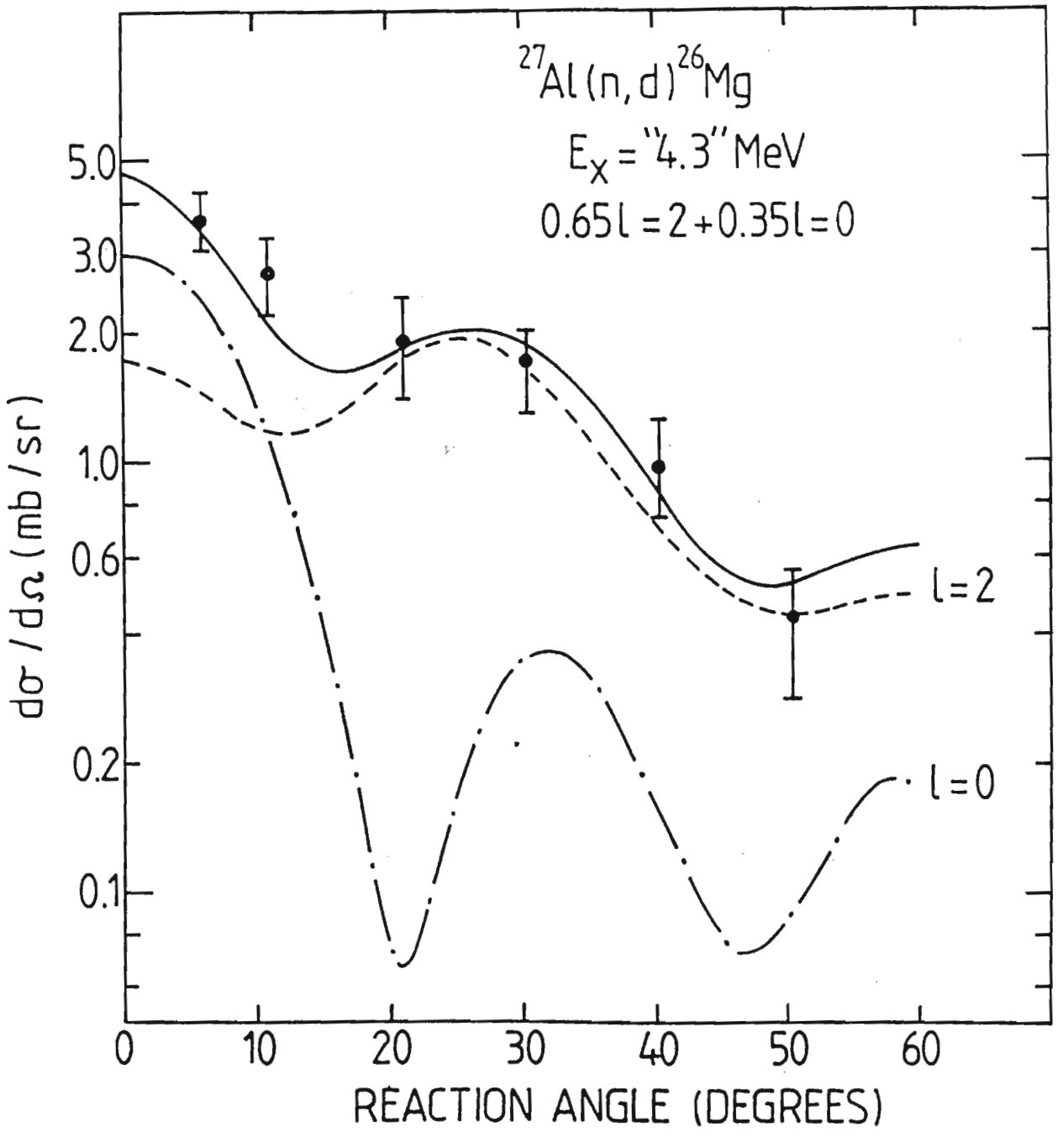

Figure 4.6: Angular distributions for the transitions to the 4.3 MeV level

4.7 Analysis of ^{56}Fe(n,d)^{55}Mn

4.7.1 Transition to the ground state

The experimental angular distributions and the DWBA fits for the transition to the ground state are shown in Fig. 4.7. There is good agreement for the fitted curve involving $l = 3$ transfer.

The "ground state" was considered as a mixture of the $\frac{7}{2}^-$ state at 0.126 MeV and the $\frac{5}{2}^-$ state at 0.00 MeV, which could not be resolved experimentally. The use of the mixed levels to calculate the spectroscopic factors does not handicap the validity of the results in any way as the $\frac{5}{2}^-$, 0.00 MeV state is only weakly excited and both levels involve $l = 3$ transfer. A spectroscopic factor of 2.4 was obtained for the transition to the "ground state" of ^{55}Mn.

4.7.2 Transition to the 1.6 MeV level

The 1.6 MeV level under investigation is an admixture of the 1.53 MeV level and the 1.88 MeV level. These levels remain unresolved in the spectrum and are treated as a single ad hoc level at 1.6 MeV, chosen closer to the 1.53 MeV state as the l=1 transition should be more dominant. Using the values of $J^\pi=\frac{7}{2}^-$ for the 1.88 MeV level and $J^\pi=\frac{3}{2}^-$ for the 1.53 MeV level, the expected l-values for transition from the 0^+ ground state of ^{56}Fe are l=3 and l=1 respectively. This is verified by a comparison of the DWBA angular distribution comprising an admixture of l=3 and l=1 and the experimental cross-section, as shown in Fig. 4.7.

The calculated values for the admixture were computed using the modified Chi-squared fit described in equation 4.18. The theoretical cross-section revealed approximately equal contributions from l=3 as from l=1 i.e A^2=0.5

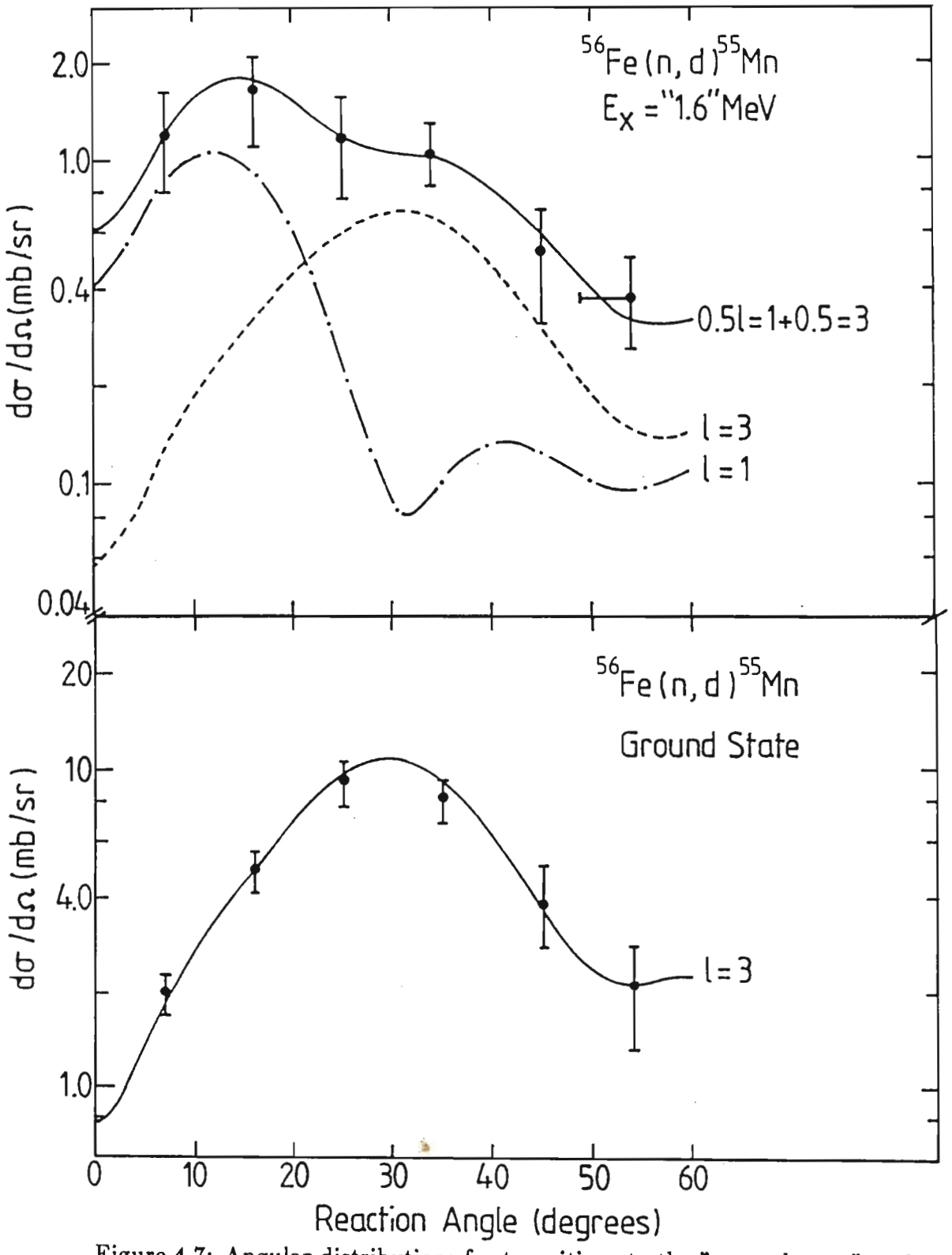

Figure 4.7: Angular distributions for transitions to the "ground state" and "1.6 MeV" levels

and B^2=0.5. A spectroscopic value of 0.4 was obtained for the mixed transition.

4.7.3 Transition to the 2.3MeV level

Several levels in ^{55}Mn lie close in energy at $\sim$ 2.3 MeV, and contributions to the deuteron peak seen in the present work could arise from transitions to the following levels : (i) the 2.20(1)MeV levels with $J^\pi = (\frac{7}{2},\frac{5}{2})^-$ (ii) the 2.27(1)MeV levels with $J^\pi = (\frac{1}{2},\frac{3}{2},\frac{5}{2})^-$ (iii) the 2.37(1) MeV level with $J^\pi = \frac{5}{2}^-$ (iv) the 2.43(1)MeV level with $J^\pi = \frac{1}{2}^+$ and the 2.56(1)MeV level with $J^\pi = \frac{3}{2}^-$.

The DWBA analysis was carried out assuming mixed $l = 3$ and $l = 1$ contributions. Using a modified Chi-squared fitting program for multiple l-fitting the combined wavefunction is given as

$$\Phi_{2.3MeV} = \alpha(\Phi_{l=1}) - \beta(\Phi_{l=3}) \qquad (4.19)$$
$$\alpha^2 + \beta^2 = 1$$

The cross-section for the 2.3 MeV state was found to be divided into 65% l=1 and 35% l=3 contributions. The combination of l=1 and l=3 is evident in the double peaked distribution(Fig. 4.8) with the l=1 distribution dominating at low angles. A spectroscopic factor of 0.4 was extracted for the transitions to the "2.3 MeV" level.

The ^{56}Fe(n,d)^{55}Mn spectrum (Fig.4.3) showing the residual levels of ^{55}Mn indicate that there are other levels above 2.3 MeV that are excited in this study. However, poor statistics and an unclear assignment as to the leading l-value of these levels hampers a lucid analysis of them. The presence of

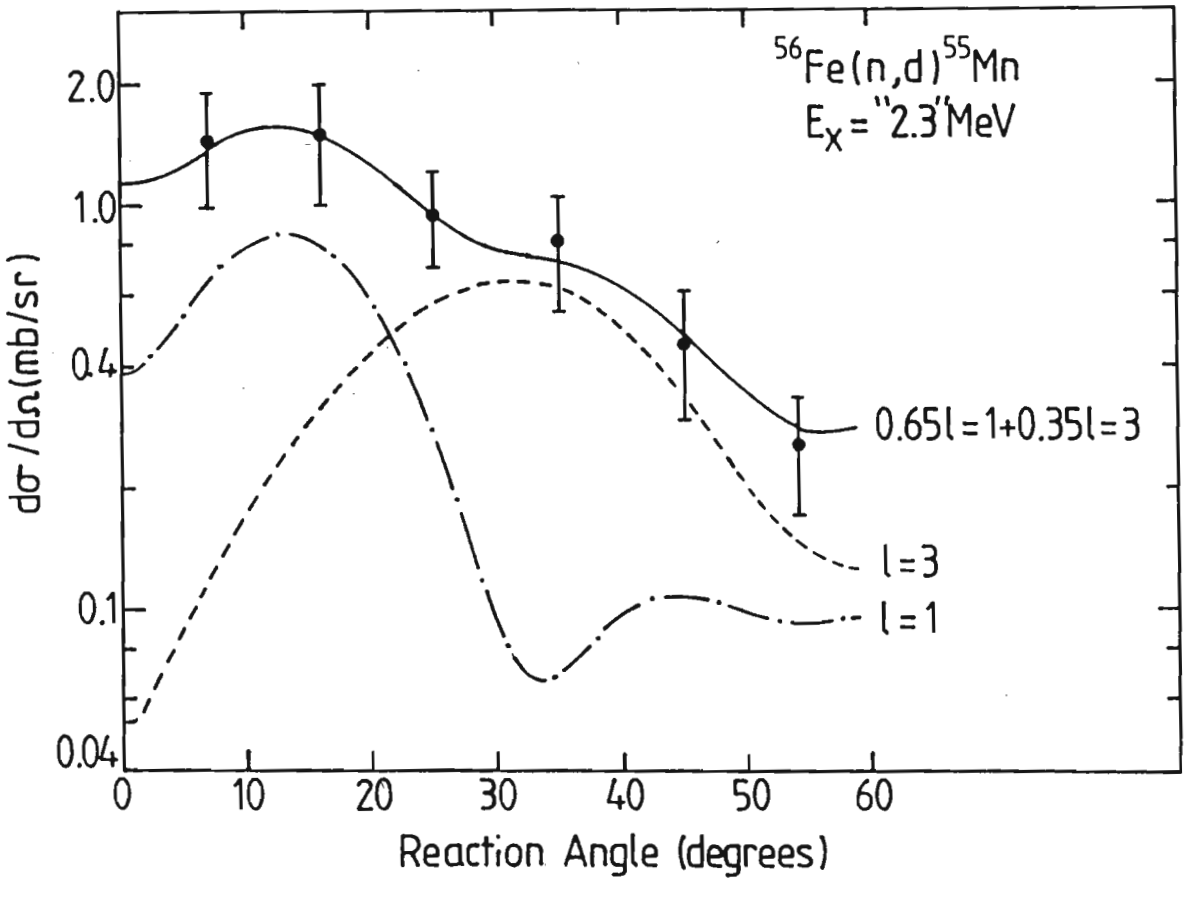

Figure 4.8: Angular distributions for transition to the levels at 2.3 MeV

high background rates at low energies also hinders the exact determination of cross-sections.

References

1.) P.D. Kunz, University of Colorado, 1978, unpublished.
2.) F.G. Perey and D.S. Saxon, Phys. Lett. 10 (1964) 107.
3.) A.C. Bawa, M.Sc. Thesis, University of Durban-Westville, 1986.
4.) W.W. Daehnick, J.D. Childs and Z. Vreclz, Phys. Rev. C21 (1980) 2253.
5.) C.S. Whisnant et al., Phys. Rev. C30 (1984) 1435.
6.) S.M. El Kadi et al., Nucl. Phys. A390 (1982) 509.
7.) N. Austern, Direct Nuclear Reaction Theories (Wiley Interscience, New York, 1970).
8.) N.K. Glendenning, Direct nuclear reactions (Academic Press, London, 1983).
9.) G.R. Satchler, Direct Nuclear Reactions (Oxford Science Publications, Oxford, 1983).
10.) R.H. Bassel, Phys. Rev. 149 (1966) 791.
11.) C.B. Fulmer and J.B. Ball, Phys. Rev. 140B (1965) 330.
12.) N.S. Chant, et al., Phys. Rev. C15 (1977) 53.
13.) A.A. Ioannides, M.A. Nagarajan and R. Shyam, Nucl. Phys. A363 (1981) 150.
14.) F.P. Brady et al., Nucl. Phys. A288 (1977) 269.
15.) R.N. Glover and E. Wiegold, Nucl. Phys. 24 (1961) 630.

Chapter 5

Discussion and conclusions

5.1 The ^{27}Al(n,d)^{26}Mg reaction

The spectroscopic factors determined in the present study are listed in Table 5.1 and compared with other experimental ^{27}Al(n,d)^{26}Mg data and with theoretical calculations. The present C^2S factors obtained show good agreement with the 14 and 50 MeV (n,d) measurements[1][2] and with the theoretical shell model predictions of Wildenthal[3].

The (n,d) results are generally more reliable than other proton pickup reactions as the neutron and deuteron optical potentials and their finite range corrections are well documented and better understood than for more complex particles.

It is interesting to note that while the C^2S factors for the lowest two states are higher than those from the 56 MeV data of Brady[1] and from the shell model predictions, the ratio of the first excited state spectroscopic factor to the ground state spectroscopic factor lies between the ratio for the theoretical case and for the 56 MeV (n,d) data. The ratio of spectroscopic factors for the first excited state to the ground state is larger than for

	E_b(MeV)	ref.	g.s.	1.81MeV	2.93MeV	4.3MeV
(1) ^{27}Al(n,d)^{26}Mg						
Present work	22		0.29(8)	0.9(3)	0.18(5)	1.9(6)
Brady et al	56	1	0.24(7)	0.7(2)	-	1.9(6)
Glover et al	14.8	2	0.3(1)	0.7(2)	0.26(7)	-
(2) ^{27}Al(d,^{3}He)^{26}Mg						
Pellegrini et al	12.8	4	1.0(4)	1.8(7)	0.4(1)	-
Cujec	15	5	0.5(1)	0.9(3)	0.29(9)	-
Wildenthal	34.5	6	0.30(7)	1.1(3)	0.23(6)	2.2(5)
Wagner	52	7	0.27(7)	0.9(3)	0.19(5)	2.0(5)
Arditi	80	8	0.26(7)	0.85(3)	-	2.05(6)
(3) Model prediction						
Shell model		3	0.29	0.75	0.29	1.80
Weak coupling		1	0.33	1.67	-	3.00
Rotational		7	0.33	0.60	-	0.07, 0.5
						$K^\pi=0^+$, 4^+

Table 5.1: Spectroscopic factors for proton pickup from ^{27}Al

the rotational model and in conjunction with similar results from (n,d)[1] and (d,^{3}He) work, implies disagreement with the Nilsson model over the assumption of an unperturbed K=0 ground state rotational band. Also, the strength observed in the 4.3MeV transition is at least two orders of magnitude larger than predicted by the rotational model. This would imply that the 4.3MeV state is not the 4^+ state of the ground state rotational band, as is assumed in the rotational model. The spectroscopic factors favour a spherical shell model and do not fit in with either the simple rotational model, in which the C^2S factors for the 1.81 and 4.3 MeV levels are too low; nor with the weak coupling model, in which the C^2S factors for the 1.81 and 4.3 MeV levels are excessively high. It is only in the ground state that all three models have some sort of agreement. Shell model effective interaction calculations[9] for spectroscopic factors in the s-d shell have detailed agreement with the experimental results.

The absence of the 0^+ state at 3.59 MeV in the residual spectrum is an indication of the extent to which the ground state of ^{27}Al may be described as a $d_{5/2}$ proton coupled to the ground state of ^{26}Mg. The ground state of ^{26}Mg is orthogonal to the 0^+ state at 3.59 MeV, implying that the C^2S factor for the 3.59MeV state should vanish in the ^{27}Al(n,d)^{26}Mg reaction. This is essentially what we observe and what is described by the shell model wave functions.

Although the triplet at 4.3 MeV is the most complicated level to analyse effectively and has the largest degree of uncertainty, the 2.93 MeV level that provides great interest also. This level is not documented for the high energy (n,d) study of low-lying even parity levels[1], with only (d,^{3}He) studies presenting reliable spectroscopic factors for the l=2 transfer[5],[6],[7]. It is noteworthy that in comparison with a high energy (d,^{3}He) study[7] on the 2.93 MeV level, our analysis presents fair agreement with shell model predictions although this level is not suitably excited for a good analysis. The

spectroscopic factor calculated for this transition is lower than shell model predictions and together with the lack of evidence for this level in other (n,d) investigations, indicates a possible difference between the (d,^{3}He) and (n,d) reactions. It might be that the unobserved strength in the transition to the second 2^+ state has been incorporated into the transition to the first 2^+ state due to configuration mixing. The $l = 2 + l = 0$ admixture for the theoretical spectroscopic factor differs from the present results in that we require a 5% $l = 0$ admixture for a good fit to the observed cross -sections, whereas the shell model predicts a 1% $l = 0$ admixture.

The experimental cross-sections show that the strongest transition strengths in the ^{27}Al(n,d)^{26}Mg reaction were to the states at 4.3 MeV excitation. This is in support of Wagners'[7] claim that the centre of gravity of the d-hole strength lies at ~3.9 MeV and the strongest even parity transitions are at ~4.3 MeV due to angular momentum coupling.

The incident beam energy is relatively too low to excite the states above 4.3 MeV adequately, making it impossible to perform a distorted waves analysis on these deuteron peaks. However, their very presence in the (n,d) angular distributions indicate that a sum rule calculation for the $l = 2$ transfers cannot be performed as we may not have analysed all the $l = 2$ transfers to exhaust the sum rule. However, if we sum the spectroscopic factors for the four levels being considered, we can get some idea as to the occupation numbers up to the 4.3 MeV level and compare these with model predictions and previous results. Table 5.2 shows the summed strength for the proton occupation numbers up to the 4.3 MeV level.

Included in Table 5.2 is the occupation numbers for the $1d$ shell from the (e,e'p) reaction on ^{27}Al[10]. The individual spectroscopic factors are not quoted for the (e,e'p) results but the low occupation number for the $1d$ shell is indicative of low spectroscopic factors for the knockout reaction.

	E_{beam}(MeV)	refs.	ΣC^2S
(n,d)			
Brady	56	1	2.8(9)
Glover	14.8	2	1.3(4)
Present work	22		3.0(9)
(d,^{3}He)			
Pellegrini	12.8	4	3.2(9)
Cujec	15	5	2.4(8)
Wildenthal	34.5	6	3.7(9)
Wagner	52	7	3.3(8)
Arditi	80	8	3.2(8)
Model predictions			
Shell model		3	3.13
Weak coupling		1	5.00
Rotational		7	1.00
(e, e'p)			
Nakamura		10	1.6(5)

Table 5.2: Summed C^2S factors for proton removal from ^{27}Al

Comparison of summed strengths for proton pickup and (e,e'p) knockout on ^{51}V and ^{90}Zr[11],[12] have also revealed low occupation numbers for (e,e'p) results as compared to shell model and proton pickup strengths. The *d*-shell occupation number of 1.6 from the (e,e'p) results is 40-60% lower than shell model predictions and experimental values. Spin dependent sum rules (SDSR) are a powerful tool in the determination of single particle strengths, and imply that the low occupation numbers are at variance with a theoretical understanding of single particle strengths in nuclei.

The investigation of deep hole states in s-d shell nuclei is problematic because of large absorption and distortion effects resulting from the final state interaction of proton and residual nucleus, which is not fully understood, and high background rates due to multiple collision processes.

Quantitative agreement of the spectroscopic factors obtained in this study with the spherical shell model and with previous (n,d) data is marred by the uncertainty over the precise $l = 0$ contribution to the 4.3 MeV level. The higher $l = 0$ admixture obtained in this study may be due to the integration of nearby states into the 4.3 MeV cross-section. It is noteworthy that the distorted wave method calculation for the 4.3 MeV level assuming a $d_{3/2}$ pickup leads to an angular distribution of virtually the same form as for $d_{5/2}$ pickup but with a 40% lower cross-section. Therefore the exclusion of the $d_{3/2}$ contribution to the 4.3 MeV level could lead to an underestimate of the spectroscopic factor for the case of significant $d_{3/2}$ contributions. However, this has the adverse effect of increasing the $l = 0$ contribution, leading to unrealistic results. With a lower $l = 0$ contribution the experimental spectroscopic factor is ~ 1.8 and in good agreement with the shell model value.

It is well known that the mixing of two possible l -values generally leads to greater uncertainties in the determination of spectroscopic factors. Thus it is expected that the uncertainty for the 4.3 MeV level triplet may be large and this may account for the deviation from the theoretical spectroscopic factor, as well as for the large $l = 0$ contribution.

The ambiguities in the parameter dependence of the DWBA cross-section is another source of error in the determination of C^2S factors. Numerous studies on the DWBA have shown that the parametrization of the optical potentials to fit the experimental data can be done in various ways without impairing the fit to elastic scattering data. Variation of optical model

parameters can effect changes of up to 50% in the spectroscopic factors without a change in the form of the cross-section[13][14].

If the single particle contribution to the wavefunction is small for the residual nucleus, approximations made to calculate the nuclear form factor for the residual nucleus are not always valid. Thus small spectroscopic factors cannot be confidently determined. Additional problems arise if the background from competing reactions is of comparable magnitude, thereby impairing the determination of the cross-section.

Most nuclei in the s-d shell are known to display a rotational structure characteristic of a deformed nucleus. It is thus worthwhile to ask why the spectroscopic factors obtained in this and other studies are in better agreement with single particle shell model values than with rotational model values. One could question the accuracy of the rotational model spectroscopic factors but this cannot hide the fact that the spectroscopic factors follow the shell model closely. It is more reasonable to argue that ^{26}Mg is only softly deformed, a feature that is well supported by its low quadrupole moment, that the addition of a proton to ^{26}Mg induces the rotational features, but in the pickup reaction the reaction mechanism is largely insensitive to the explicit rotational features of ^{27}Al. The rotational features are taken into account in the deformation used for the optical potentials. A full analysis of a strongly deformed nucleus would require a coupled channels (CC) calculation as the differential cross-section would depend on the amplitude and phase of both one step and multi-step excitations. Thus the sphericising tendency of the last two neutrons in ^{26}Mg facilitates the use of a "near-spherical" picture of ^{27}Al.

The change in shape in the s-d shell occurs from the A=24 nuclides to the A=28 nuclides and it is reasonable to expect that in the middle region where the change occurs, that is at A=26, the change from prolate to

oblate shape would manifest itself as a delicate equilibrium between the two shapes. Thus we might expect a vibration around a spherical mean and the pickup reaction reflects the mean state of the ^{27}Al(n,d)^{26}Mg reaction, thus enabling a simple shell model picture.

If we assume that the ^{26}Mg nucleus is largely spherical in terms of our surface reactions then any noticeable features of rotational behaviour must originate from the addition of a proton to the ^{26}Mg nucleus. This would imply that the nature of the nucleon-nucleon interaction is important as is the different deformations of the neutron and proton orbits. This is largely applicable in using the extended shell model in which the assumption of an ^{16}O core + 10 valence nucleons incorporates the inclusion of rotational features. The application of a microscopic analysis to the ^{27}Al(n,d)^{26}Mg reaction is therefore worthwhile to understand the fine details of the ^{27}Al nucleus.

In summary, we have concluded that the ^{27}Al(n,d)^{26}Mg reaction is well described by the shell model. The experimental spectroscopic factors correspond with those obtained in the shell model and, for the low lying levels at least, are not in accordance with the weak coupling model or rotational model predictions. The spectroscopic factors obtained with the (n,d) reaction also show a clear energy independence as compared to those obtained with the (d,^{3}He) reaction.

5.2 The ^{56}Fe(n,d)^{55}Mn reaction

The experimental and theoretical spectroscopic factors for the ^{56}Fe(n,d)^{55}Mn reaction are given in Table 5.3. There is fair agreement between the experimental values obtained via (d,^{3}He) and (n,d) reactions and the theoretical shell model values. The QPCC and CVM spectroscopic factors are very similar for the 1.6 and 2.3 MeV levels but are much higher than shell model and experimental value for the 'ground' state.

The shell model with KB interaction predicts a C^2S factor of 0.0 for the 0.00 MeV state and the QPCC and CVM calculations are unable to reproduce spectroscopic factors for this level. In a recent (d,^{3}He) work[15], the C^2S factor obtained for the 0.00 MeV state was only 3% of that of the 0.126 MeV state. Both levels are unambiguously l=3 transfer from the 0^+ ground state of ^{56}Fe and although the possible inclusion of l=3 transfer contribution from the 0.00 MeV state will raise the spectroscopic factor, this effect is not expected to be significant. Theoretical shell model spectroscopic factors have been determined via the KB and SDI methods. For present purposes only the value from the KB interaction have been used as these were known to have closer agreement with experiment and yield superior results[15].

The spectroscopic factor extracted from this fitting is higher than the theoretical factors and those of the (d,^{3}He) results. It is well known that the mixing of possible l-values leads to greater uncertainty in the determination of spectroscopic factors. The high C^2S factor for this level might be attributed to (i) contribution from the 1.29 MeV level, which is expected to lie in the tail of the 1.53 MeV peak. The 1.29 MeV peak is not adequately excited either in this study or in the (d,^{3}He) study, but is expected to make some contribution to the cross-section,(ii) contribution from the 2.20 MeV

	E_{beam}(MeV)	refs.	g.s.	1.6MeV	2.3MeV
(n,d)					
Present work	22		2.4(7)	0.4(1)	0.4(1)
Colli et al	14	15	6(2)	-	-
(d,^{3}He)					
Puttaswamy	80	14	2.9(7)	0.15(4)	0.5(1)
Model predictions					
Shell model		14	3.14	0.08	0.37
QPCC			4.49	-	-
CVM			4.16	0.15	0.55

Table 5.3: Spectroscopic factors for proton pickup from ^{56}Fe

level , expected to lie close to the 1.88 MeV peak. The energy resolution of $\sim$ 0.7 MeV implies that this level is also likely to contribute towards the cross-section of the 1.6 MeV level.

For the purpose of comparison, theoretical and previous experimental results have been used to calculate the C^2S factor for the 2.3 MeV level by using the relative proportions of the l-values as a basis for combining the respective spectroscopic factors for the levels contributing to 2.3 MeV. The present value of 0.4 for C^2S is in agreement with theoretical and experimental values although we expect that there are large errors in the determination of this value.

The QPCC calculations have only produced a result for the ground state, which it predicts to be $J^\pi=\frac{7}{2}^-$. This incorrect prediction of the ground state spin-parity and the extremely high spectroscopic factor for pickup to that level casts doubt on the usefulness of the QPCC for calculating the spectroscopic factors. In the CVM however, the use of three hole cluster configurations enables the correct prediction of the ground state spin-parity and also produces spectroscopic factors that are in reasonable agreement with experiment.

Although there is evidence for a rotational band structure in ^{56}Fe, we have found that the spectroscopic factors indicate a shell model structure for the low-lying levels in ^{56}Fe. There are at present no theoretical spectroscopic factors available based on the Nilsson model for ^{56}Fe. The good agreement between experimental values and shell model predictions does not in any way exclude the possibility of rotational behaviour, especially of the highly excited states.

Taking into consideration the effective shell model picture painted for both ^{27}Al and for ^{56}Fe one might speculate that the (n,d) reaction is insensitive

to the rotational nature of these nuclei. However, it must be noted that we have only investigated the low-lying levels in these nuclei and that other studies at higher incident energies have found the higher excitation energy levels behaving differently[1],[7]. Significantly, low energy investigations[3],[5] of proton pickup from the target nuclei have been interpreted in terms of the rotational model, while higher energy studies[1],[7] have found the low-lying levels to be of a shell model nature and the higher states as having a rotational nature. If the energy of the incoming particle is important, then one has to take into account the compound nucleus contribution and it's effects, especially at low energies. Also, the residual nucleon-nucleon interaction is of importance and must be properly accounted for. It has been suggested[17] that the inclusion of form factor effects due to residual interactions between nucleons in the target nuclei can reduce the values of spectroscopic factors drastically.

While the rotational model description of the target nuclei based on the Nilsson wave functions cannot reproduce the experimental results for the low-lying states, a rotational band structure description does not exclude a shell model description as has been used. The physical interpretation of shell model results is usually based on a single dominant configuration. Within the broad context of the shell model there are numerous possible configurations that can co-exist or overlap to some extent. Thus we might expect to find, especially for ^{27}Al, that the wave function we have observed is an overlap of dominant shell model wavefunctions and projected Nilsson wavefunctions and that at high incident energies the low-lying states display predominantly shell model structure while the higher excited states may display a different dominant structure.

References

1.) F.P. Brady et al., Nucl.Phys. A288 (1977) 269.
2.) R.N. Glover and E. Wiegold, Nucl.Phys. A24 (1961) 630.
3.) B.H. Wildenthal, J.B. McGory, E.C. Halbert and P.W.M. Glaudemans, Phys. Lett. 26B (1968) 692.
4.) F. Pellegrini and S. Wiktor, Nucl. Phys. 40 (1963) 412.
5.) B. Cujec, Phys. Rev. B136 (1964) 1305.
6.) B.H. Wildenthal and E. Newman, Phys. Rev. 175 (1968) 1431.
7.) G.J. Wagner, G. Mairle, U. Schmidt and P.Turek, Nucl. Phys. A125 (1969) 80.
8.) M. Arditi et al., Nucl. Phys. A165 (1971) 225.
9.) F. Meurders, P.W.M. Glaudemans, J.F.A. Van Hienan and G.A. Turimer, Z. Physik A276 (1976) 113.
10.) K. Nakamura et al., Nucl. Phys. A271 (1976) 221.
11.) J.W.A. den Herder et al., Phys. Rev. Lett. 57 (1986) 1843.
12.) J.W.A. den Herder et al., Phys. Lett. 161B (1985) 65.
13.) B.J. Cole, A. Watt and R.R. Whitehead, J. Phys. G.: Nucl. Phys. 2 (1976) 501.
14.) W.R. Coker, Z. Physik A273 (1975) 251.
15.) N.G. Puttaswamy et al., Nucl. Phys. A401 (1983) 269.
16.) L. Colli, et al., Nucl. Phys. 46 (1963) 73.
17.) J.B. McGrory, Phys. Rev. 160 (1967) 915.